

Frequency-Domain Control Design in Power Systems

THÈSE N° 8746 (2018)

PRÉSENTÉE LE 7 SEPTEMBRE 2018

À LA FACULTÉ DES SCIENCES ET TECHNIQUES DE L'INGÉNIEUR

LABORATOIRE D'AUTOMATIQUE

PROGRAMME DOCTORAL EN GÉNIE ÉLECTRIQUE

ÉCOLE POLYTECHNIQUE FÉDÉRALE DE LAUSANNE

POUR L'OBTENTION DU GRADE DE DOCTEUR ÈS SCIENCES

PAR

Christoph Manuel KAMMER

acceptée sur proposition du jury:

Dr S.-R. Cherkaoui, président du jury

Dr A. Karimi, directeur de thèse

Prof. F. Dörfler, rapporteur

Prof. J. M. Guerrero, rapporteur

Prof. G. Ferrari Trecate, rapporteur



ÉCOLE POLYTECHNIQUE
FÉDÉRALE DE LAUSANNE

Suisse
2018

Acknowledgements

Most importantly I would like to thank my PhD supervisor Alireza Karimi for all his support and guidance throughout these four years. He freely let me explore my various side projects and ideas, but always knew when to focus my attention back on my main topic such that I actually managed to finish this thesis in time. Thanks to his mentoring and active participation in my research I was able to study a large range of control and power systems topics in theory as well as in practice, and I will be forever grateful to him for offering me this opportunity.

I would also like to thank Florian Dörfler for giving me a great introduction to my thesis topic when I first entered the world of power systems, and for the many visits and discussions we had afterwards. Similarly, I would like to thank the other members of my thesis committee, Josep M. Guerrero, Giancarlo Ferrari Trecate and Rachid Cherkaoui for reading my work, and for the great discussions during my defense.

A special note goes to Adrian, who is mostly to blame that I applied to a position in Lausanne in the first place. Our casual side projects and gym/food sessions were a great part of the experience!

Furthermore, I am very thankful to Dominique Bonvin and all members of the Laboratoire d'Automatique for the great time I had in the past four years. The friendly and really positive culture and spirit of the lab were one of the most important parts of this journey. Thanks Christophe for still helping me out with LabView even though I installed Windows on your precious apple hardware. Also thanks a lot to all my office and drinking mates (probably incomplete and in no specific order): Ehsan, Martand, Petr, Tafarel, Luca, Altug, Tomasz, Georgios, Faran, Harsh, Predrag, Diogo, Ivan, Ye, Andrea and Rene (great couch!). Also thank you Andreas and Willi for all the good times, great beers and fun chats. Finally, thanks to Zlatko, who showed me that it's possible to write a thesis in less than 2 months, and to Mahdieh for being a great friend overall!

Also, I'd like to thank Joanna, my brother Stephan and all my friends in Bern and beyond for reminding me that there is a life outside of work and university, which is definitely an important thing to remember.

Finally, thanks a lot to my parents who supported me greatly throughout all this time, it seems that I finally made it after all! (:

Lausanne, 08 of July 2018

C. K.

Abstract

The scope of this thesis encompasses two main subjects: fixed-structure data-driven control design on one side, and control design in power systems on the other. The overall goal is to identify challenging and relevant problems in power systems, to express them as rigorous specifications from the viewpoint of control systems, and to solve them by developing and applying advanced methods in robust control. This work aims to combine expertise from both fields to open up a holistic perspective and bridge the gap between control and power systems.

First, the derivation of a novel fixed-structure, data-driven frequency-domain control design method for multivariable systems is described. A key feature of the method is that only the frequency response of the plant is required for the design, and no parametric model is required. The designed controllers are fully parametrized in terms of matrix polynomial functions and can take a centralized, decentralized or distributed structure. The controller performance is formulated as H_2 and H_∞ constraints on any loop transfer function. A convex formulation of the optimization problem is derived, and it is shown that the solution converges to a locally optimal solution of the original problem. The versatility of the design method is demonstrated in various simulation examples, as well as in experiments on two electromechanical setups.

Next, a frequency-domain modeling approach for power grids is discussed. A model based on dynamic phasors is developed that represents the electromagnetic and electromechanic dynamics of lines, inverters, synchronous machines and constant power loads. It also offers a modular structure that makes it straightforward to combine white-, grey- and blackbox models in a single framework.

Then, the control design method and dynamic phasor model are applied in two relevant power systems case studies. First, the design of a decentralized current controller for parallel, grid-connected voltage source inverters in a typical distribution grid is considered. It is shown how performance specifications can be formulated as frequency-domain constraints in order to attenuate the resonances introduced by the output filters and coupling effects, and to provide robustness against model uncertainties and grid topology changes. The controllers for all VSIs are designed in a single step, and stability and performance is guaranteed by design. Furthermore, an approach for plug-and-play control design is presented. The results are validated in numerical simulation as well as in power-hardware-in-the-loop experiments.

The second study concerns the design of a distributed controller that combines primary

Acknowledgements

and secondary frequency and voltage control for an islanded, meshed low-voltage grid with any number of voltage source inverters and synchronous generators in a single framework. No assumption on the R/X-ratio of the lines is made, and it is shown how advanced control specifications such as proportional active power sharing, zero frequency steady-state error and decoupling can be formulated as constraints on the norm of weighted sensitivity functions. Furthermore, the communication delays of the distributed controller are considered exactly during the design. The controller is implemented in numerical simulation, and results show significantly improved performance as compared to the classical hierarchical structure.

This thesis was supported by the SCCER-FURIES competence center.

Keywords: *Data-driven control, robust control, convex optimization, H_2/H_∞ , power system transients, power system stability, primary control, secondary control, distributed control*

Zusammenfassung

Diese Doktorarbeit umfasst zwei Hauptthemen: einerseits datenbasiertes Reglerdesign für Regler mit fixer Struktur, und andererseits Reglerdesign in Stromnetzen. Das Hauptziel der Arbeit ist, herausfordernde und relevante Probleme im Stromnetz zu identifizieren, sie also rigorose Spezifikationen im Sinne der Regelungstechnik zu formulieren, und mittels neu entwickelten und fortschrittlichen robusten Reglerdesignmethoden zu lösen. Die Arbeit zielt darauf ab, Kompetenzen aus beiden Fachgebieten zu kombinieren, um eine gesamtheitliche Perspektive des Problems zu erhalten, und die Lücke zwischen Regelungstechnik und Elektrotechnik zu schliessen.

In einem ersten Teil wird die Herleitung einer datenbasierten Reglerdesignmethode für Regler mit fixer Struktur auf der Frequenzebene beschrieben. Ein Hauptmerkmal der Methode ist, dass nur die Frequenzantwort des Systems für das Design benötigt wird, und dass kein parametrisches Modell vonnöten ist. Die entworfenen Regler sind komplett parametrisiert im Sinne von polynomiellen Matrixtransferfunktionen, und können eine zentralisierte, verteilte oder dezentrale Struktur annehmen. Die Reglerperformance kann als H_2 oder H_∞ Zwangsbedingung für jegliche Übertragungsfunktion im Regelkreis formuliert werden. Eine konvexe Formulierung des Optimierungsproblems wird hergeleitet, und es wird gezeigt dass die Lösung zu einer lokal optimalen Lösung des originalen Problems konvergiert. Die Vielseitigkeit der Designmethode wird in verschiedenen Beispielen und anhand zweier elektromechanischer Experimente demonstriert.

Im nächsten Schritt wird ein Modellierungsansatz für Stromnetze im Frequenzbereich behandelt. Basierend auf dynamischen Phasoren wird ein Modell entwickelt, welches die elektromagnetischen und elektromechanischen Dynamiken der Kabel, Wechselrichter, Synchronen Maschinen und Lasten mit konstanter Leistung abbildet. Es bietet ausserdem eine modulare Struktur, welche es einfach ermöglicht, White-, Grey- und Blackbox-Modelle in einer Gesamtstruktur zu vereinen.

Schlussendlich werden die Reglerdesignmethode und das Modell in zwei relevanten Fallstudien im Stromnetz angewandt. Im ersten Beispiel wird das Design eines dezentralen Stromreglers für parallel verbundene Wechselrichter in einem typischen Verteilnetz behandelt. Es wird aufgezeigt, wie Performancespezifikationen als Zwangsbedingungen im Frequenzbereich formuliert werden können, um die Resonanzen der Ausgangsfilter und Kopplungseffekte zu dämpfen, und um Robustheit gegenüber Modellunsicherheiten und verschiedenen Netztopologien zu gewährleisten. Die Regler aller Wechselrichter werden in einem Schritt berechnet, und Stabilität und Performance sind garantiert. Weiterhin

Acknowledgements

wird ein Vorgehen für Plug-and-Play Reglerdesign präsentiert. Die Ergebnisse werden sowohl in numerischer Simulation, als auch in Power-Hardware-in-the-Loop-Experimenten validiert.

Die zweite Studie behandelt das Design eines verteilten Reglers, welcher primäre und sekundäre Frequenz- und Spannungsregelung eines geinselten, maschigen Niederspannungsnetzes mit einer beliebigen Anzahl an Wechselrichtern und Synchrongeneratoren in einer Gesamtstruktur verbindet. Es werden keine Annahmen bezüglich des R/X-Verhältnisses der Kabel gemacht, und es wird gezeigt wie komplexe Reglerspezifikationen, so wie proportionales Teilen der aktiven Ausgangsleistung, kein stationärer Fehler der Frequenz und Entkopplung als Zwangsbedingungen auf der Norm von gewichteten Sensitivitäten formuliert werden können. Ausserdem wird die Kommunikationszeitverzögerung beim Reglerdesign berücksichtigt. Der Regler wird in numerischer Simulation getestet, und die Resultate demonstrieren eine signifikant bessere Leistung als die klassische, hierarchische Struktur.

Diese Arbeit wurde mit Unterstützung des SCCER-FURIES Kompetenzzentrums geschrieben.

Stichworte: *Datenbasierte Regelung, robuste Regelung, konvexe Optimierung, H_2/H_∞ , Stromnetztransienten, Stromnetzstabilität, primäre Regelung, sekundäre Regelung, verteilte Regelung*

Contents

Acknowledgements	iii
Abstract (English/Deutsch)	v
List of Figures	xiii
List of Tables	xvii
1 Introduction	1
1.1 Motivation	1
1.2 Thesis Organization	4
2 Fixed-Structure Control Design using Frequency-Domain Data	9
2.1 Introduction	9
2.2 State of the Art	10
2.2.1 State-Space Methods	10
2.2.2 Methods using Frequency-Domain Data	11
2.3 Frequency response data	12
2.4 Controller Structure	13
2.5 Control Performance	14
2.5.1 H_∞ Performance	15
2.5.2 H_2 Performance	17
2.5.3 Loop shaping	18
2.6 Stability Analysis	19
2.6.1 A detailed look at the Nyquist Criterion	20
2.6.2 Stability Proof - Discrete-Time	22
2.6.3 Multimodel uncertainty	24
2.6.4 Frequency-domain uncertainty	25
2.7 Implementation	25
2.7.1 Frequency Gridding	26
2.7.2 Controller Order	27
2.7.3 Initial controller	27
2.7.4 Numerical Issues	28
2.7.5 Iterative algorithm	29

Contents

2.8	Simulation Examples	31
2.8.1	Compleib Examples	31
2.8.2	Hard-disk Drive	32
2.8.3	Multivariable System	34
2.9	Conclusion	37
2.A	Stability Proof - Continuous-Time	37
3	Frequency-Domain Modeling of Power Grids	41
3.1	Introduction	41
3.1.1	State of the Art	41
3.2	Phasor Notation	42
3.3	Frequency-Domain Model of Voltage and Current Dynamics	43
3.3.1	Line Current Dynamics	43
3.3.2	LCL Filter Dynamics	45
3.3.3	Complete Transfer Function Model	46
3.4	Frequency-Domain Power Flow Model (Dynamic Phasor Model)	47
3.4.1	Dynamic Power Flow Equations	47
3.4.2	Line Power Flows Model	49
3.4.3	Voltage Source Inverter Model	50
3.4.4	Synchronous Generator Model	51
3.4.5	Complete Dynamic Phasor Model	52
3.4.6	Validation of Dynamic Phasor Model	54
3.5	Conclusion	55
4	Current Control Design for Parallel Grid-Connected Inverters	57
4.1	Introduction	57
4.1.1	State of the Art	58
4.2	Control Design	60
4.2.1	Grid Model	61
4.2.2	Control Specifications	61
4.2.3	Controller Structure	63
4.2.4	Convex Formulation	64
4.2.5	Simulation Results	66
4.3	Plug-and-Play Design	68
4.4	Experimental Results	69
4.4.1	PHIL Setup	70
4.4.2	PHIL Results	70
4.5	Conclusion	72
5	Distributed Primary and Secondary Control in Islanded Grids	75
5.1	Introduction	75
5.1.1	State of the Art	76
5.2	Grid Model	77

5.2.1	VSI Dynamics	78
5.2.2	Synchronous Generator Dynamics	79
5.2.3	Complete Transfer Function Model	80
5.3	Control Design	81
5.3.1	Control Specifications	82
5.3.2	Controller Structure	84
5.3.3	Convex Formulation	85
5.4	Simulation Results	87
5.5	Conclusion	91
5.A	Primary and Secondary Control Design: Additional Results	92
5.A.1	Example Grid	92
5.A.2	Improved Primary Control Performance	92
5.A.3	Robustness Towards Topology Change	96
5.A.4	Distributed Secondary Control	98
6	Conclusion	103
6.1	Summary	103
6.2	Future Research	104
A	Data-Driven Control Design for Atomic-Force Microscopy	107
A.1	System Description	107
A.2	State of the Art	108
A.3	Control Design	110
A.3.1	Plant Identification	110
A.3.2	Control Performance	111
A.3.3	Controller Structure	111
A.3.4	Convex Formulation	112
A.4	Experimental Results	113
A.5	Conclusion	115
B	Data-driven Multivariable Control of a 2-DOF Gyroscope	117
B.1	Experimental Setup	117
B.2	Frequency Response	117
B.3	Control Design Formulation	118
B.4	Experimental Results	121
B.5	Conclusion	122
	Bibliography	123

List of Figures

1.1	General layout of modern power grids. Electricity is generated both on the high- and low-voltage level, and many distributed power plants are involved.	2
2.1	Nyquist contours.	21
2.2	Simplified discrete-time Nyquist contour.	22
2.3	The main steps of the control design method.	30
2.4	Bode magnitude plot of the plant used in the hard-disk drive example. . .	33
2.5	Comparison of the open-loop transfer functions. In blue is the desired open-loop function L_d , in red the obtained open-loop function L with the proposed method, and in dashed yellow the obtained L with the <i>hinfstruct</i> controller.	34
2.6	Plot of the achieved mixed sensitivity norm for different controller orders p . The dashed red line shows the globally optimal value obtained by <i>mixsyn</i> . . .	36
3.1	One-line diagram of a distribution grid with multiple VSIs and constant current loads.	43
3.2	Block diagram of the complete closed-loop model.	47
3.3	Small example grid with one load, one VSI and one SG.	49
3.4	Block diagram of the full dynamic phasor model.	52
3.5	One-line diagram of a 50 Hz/230 V islanded grid with 3 SGs and one VSI. The arrows denote constant power loads.	54
3.6	Comparison of frequency and voltage between nonlinear simulation (in blue) and linear dynamic phasor model (in red).	55
3.7	Comparison of power flows between nonlinear simulation (in blue) and linear dynamic phasor model (in red).	56
4.1	Electrical one-line diagrams: a) a rural distribution grid with 4 VSIs and a Line Voltage Regulator (LVR), b) the output filter configuration and controller block diagram of the VSIs.	58
4.2	Measurements of three-phase current and voltage at the LVR after it is switched on [78].	59
4.3	Maximum singular value plots of the grid model. The model without the LVR is in blue, and with the LVR in red.	62

List of Figures

4.4	Maximum singular values plots: a) the controller (in green) and the plant without and with the LVR (in blue and red), b) the closed-loop sensitivities and c) the input sensitivities without and with the LVR. The dashed lines indicate the constraints.	65
4.5	Inverter current step response of VSI 1 without and with the LVR. The dashed line shows the current reference.	67
4.6	Block diagram of plant for plug-and-play design.	68
4.7	Inverter current step response of the plug-and-play controller of VSI 5 without the LVR. The dashed line shows the current reference.	69
4.8	One-line diagram of the PHIL setup. The output filter impedances are identical for all VSIs.	70
4.9	Photo of a custom-designed inverter used for the PHIL experiments. . . .	71
4.10	The PHIL results are in red, simulation results are in blue, the dashed line shows the current reference.	72
4.11	Three-phase voltage and current of VSI 1 without and with the LVR during the step of $I_{t,d}^1$	73
5.1	One-line diagram of a 50 Hz/230 V islanded grid. The bus numbers are indicated in red and the arrows denote constant power loads.	78
5.2	Block diagram of speed-controlled synchronous generator.	80
5.3	Block diagram of complete dynamic phasor model of the grid from Fig. 5.1. The block K is the controller.	81
5.4	Frequency of the DG units after an active power load step. The new controller is in red, droop in blue and DAPI in yellow.	89
5.5	Active output power of the DG units after an active power load step. The new controller is in red, droop in blue and DAPI in yellow.	89
5.6	Voltage magnitude of the DG units after an active power load step. The new controller is in red, droop in blue and DAPI in yellow.	90
5.7	Reactive output power of the DG units after an active power load step. The new controller is in red, droop in blue and DAPI in yellow.	91
5.8	Model adapted from [137] with 11 buses, 2 inverter-interfaced batteries, 1 synchronous generator and 6 loads. The sign \downarrow denotes the loads.	93
5.9	Maximum singular value plots of the SG sensitivity $W_1 S$. Blue is the droop controller, red is the new controller.	96
5.10	Comparison of simulation results. Blue is the droop controller, red is the new primary controller	97
5.11	Generator reactive output power after an active power load step. Blue is the droop controller, red is the new primary controller.	97
5.12	Generator frequency after line 9-10 is closed. Blue is the droop controller, red is the new primary controller.	98
5.13	Block diagram of the distributed secondary controller.	99

5.14	Comparison of simulation results for secondary control. Blue is the droop controller, red is the improved primary controller, yellow is with the distributed controller.	102
A.1	a) Block diagram of the functionality of an AFM. b) Exploded view of the head used for the experiments.	107
A.2	Comparison of control design steps in AFM for conventional approaches and using a data-driven approach.	110
A.3	Evolution of the frequency response of a J-scanner in liquid over 3 hours. The envelope shows the range of the variations. Three example responses are shown, where blue is at the start, red is after 1 hour and yellow is after 2 hours.	110
A.4	Comparison of the nominal closed-loop sensitivities. a) Measured plant frequency response in green, designed 10th-order controller in blue. b)-d) Sensitivity S , closed-loop sensitivity T and input sensitivity U for the 10th-order controller in blue and the PI-controller in yellow. Black dashed lines indicate the constraints W_2, W_3	113
A.5	Frequency responses and designed controllers for different systems. The upper plots show the plant in green and the controller in blue. The lower plots show the nominal and measured closed-loop sensitivity in blue and red respectively, with the H_∞ constraint in dashed black. a) J-scanner in air, b) E-scanner in air, c) J-scanner in liquid, d) triple-S scanner in air.	114
A.6	Imaging of DNA at increasing line rates.	114
A.7	Time-lapse of the self-assembly of a DNA lattice.	115
B.1	The gyroscope experimental setup by Quanser.	118
B.2	Block diagram of the cascaded controller structure of the gyroscope.	118
B.3	The measured frequency response of the blackbox model G at different disk speeds. The blue line is the response at a disk speed of 300 rpm, red at 400 rpm and yellow at 500 rpm.	119
B.4	Bode magnitude plots of the desired open-loop transfer function L_d and the achieved $L_{1,2,3}$ for the three different plant models. The blue line is the achieved response at a disk speed of 300 rpm, red at 400 rpm and yellow at 500 rpm. The desired L_d is shown in dashed purple.	120
B.5	Closed-loop sensitivities and measured step response.	121

List of Tables

2.1	Comparison of optimal mixed sensitivity norms for 10 plants from Compleib	32
5.1	Line Parameters	77
5.2	DG Units Parameters	81
5.3	CIGRE Grid Parameters	93

1 Introduction

1.1 Motivation

The advent of the 21st century poses some very challenging problems for the incredibly complex, distributed and nonlinear system that is our power grid. From a very personal perspective, in a recent vote in Switzerland a new energy strategy act for 2050 was enacted, which identifies an increase in the use of renewable energy and a withdrawal from nuclear power as key strategic energy objectives for this country. Far from pursuing an isolated course, Switzerland is part of a global trend to replace fossil and nuclear energy with renewable resources such as wind and solar.

From a power systems perspective, these developments imply a drastic shift away from a centralized architecture, where power is produced by few large power plants, to distributed and renewable generation, where a large portion of the electricity is produced by myriads of small generation units (see Fig. 1.1). Design rules and guidelines established by power companies after decades of experience no longer hold true, and new paradigms are required. Due to the intermittent nature of renewable resources such as wind and solar, the generation will be highly dynamic in comparison to conventional power systems, and storage of energy is required to damp the fluctuations of generation. On the other hand, CO₂ reduction strategies are pushing the industry towards electric vehicles. This increases the overall demand for electric power, but an even bigger challenge is the change in consumption patterns and maximum loading due to fast charging technologies, which will have a considerable effect on grid planning and operation. The integration of renewable and intelligent distributed generation units, energy storage systems and electric vehicles will completely change the structure of the grid as we know it today.

On a large scale, a key problem is the increasing loss of inertia [1]. A fundamental characteristic of the power grid is that almost no energy can be stored inside the lines, and production always has to perfectly match consumption in order to maintain stability. Since it is impossible to exactly predict the consumption, some form of fast-acting

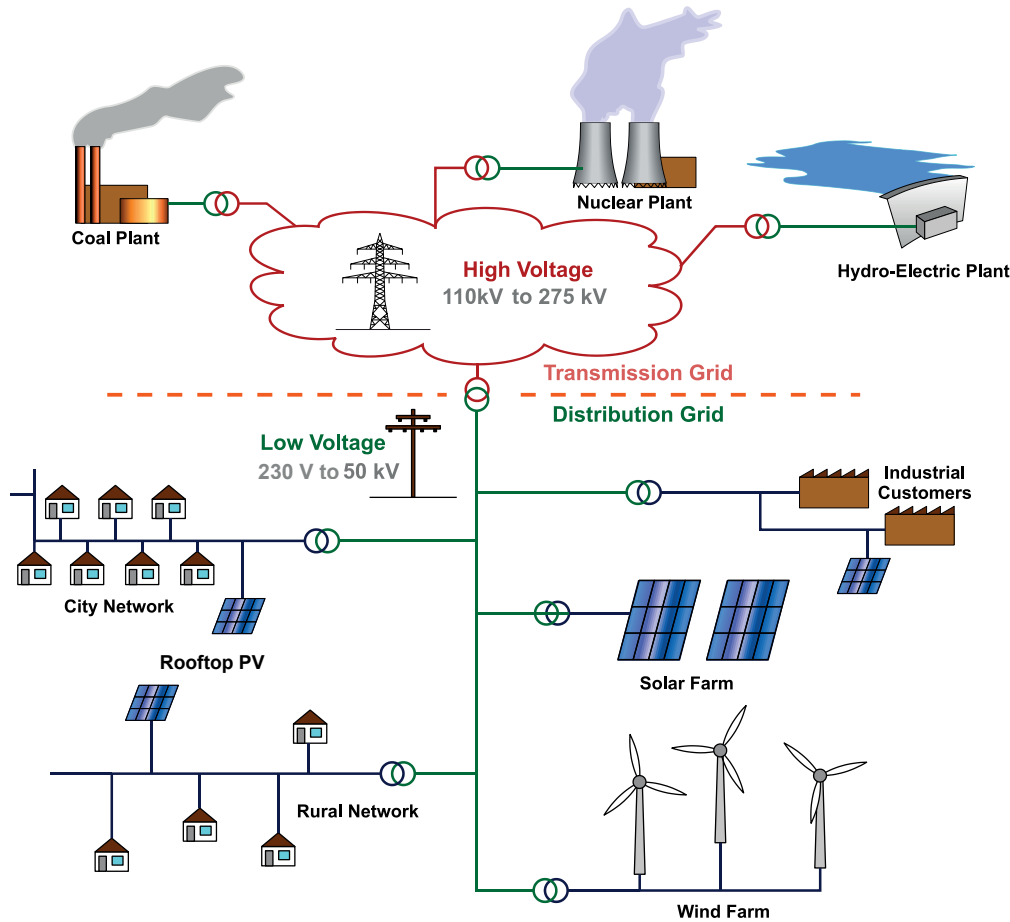


Figure 1.1 – General layout of modern power grids. Electricity is generated both on the high- and low-voltage level, and many distributed power plants are involved¹.

energy storage is required to balance the production and consumption and maintain the equilibrium. Today, this role is taken on by the inertia of the large synchronous generators, which acts as an energy reservoir. Since the grid frequency is directly tied to the rotational frequency of the generators, large inertia renders frequency dynamics more benign by slowing down transients and dampening oscillations, which guarantees a sufficiently large response time to events.

The task to maintain the grid frequency and voltage close to their nominal values is called primary and secondary control. Primary control is traditionally provided by droop control, which is a decentralized proportional controller that relates the output power of a generator to the grid frequency. If the frequency drops power generation is increased, and vice versa. However, being a proportional controller, droop control exhibits a steady-state error after a disturbance. The task to restore the frequency to its nominal value is taken on by secondary control, which is in essence a centralized integral controller that adjusts

¹MBizon (https://commons.wikimedia.org/wiki/File:Electricity_Grid_Schematic_English.svg), „Electricity Grid Schematic English“, modified, <https://creativecommons.org/licenses/by/3.0/legalcode>

the production of all generators in the grid.

A fundamental difference of renewable generation units such as solar and wind is that they do not provide any rotational inertia (or more precisely, in the case of wind it is difficult to leverage). As more and more power is supplied by these units, the total inertia in the grid decreases, and frequency dynamics become much faster and less well damped. If a certain threshold is crossed and the inertia falls too low, this situation unavoidably results in cascaded failures and a complete blackout of the grid. While nowadays most renewable sources simply inject as much power into the grid as they can produce, it is clear that distributed generation units will have to start participating in primary and secondary control to maintain the stability of the grid in the future. However, these sources are generally connected to the grid through power electronic devices such as inverters, and their dynamics are fundamentally different from synchronous generators. New approaches and methodologies for primary and secondary control have to be developed to guarantee stable and robust operation of grids with both synchronous machines and inverter-interfaced sources.

Concerning secondary control, the traditional approach where a centralized integral controller has to communicate with all generation units is not feasible if high numbers of distributed generation units are involved. The large number of required communication channels would be expensive, and decreases the reliability of the grid. Also, on a physical level, grids with low inertia and stochastic generation exhibit fast dynamics with large changes, and the separation of timescales required by a hierarchical structure may render it infeasible. Therefore, significant research efforts are being made towards distributed control approaches that combine primary and secondary control in a single framework.

Another challenge is that, unlike traditional power plants, many renewable generation units are not connected to the high-voltage transmission grid, but are instead embedded on the medium- and low-voltage distribution grid level. Introducing and operating distributed generation on the distribution grid level on a large scale is still new territory, and many challenges exist. An example of a more and more frequent issue in modern distribution grids are overvoltage situations due to increasing penetration of photovoltaics. The stochastic nature of solar power leads to rapid and unpredictable changes in power generation, which leads to situations that have not been encountered before. New control strategies involving distributed storage and controllable transformers are promising solutions to this problem. When considering primary control on the low-voltage level, another important aspect is that the dynamics of power lines in distribution grids are fundamentally different from the transmission grid. Since droop control has been developed for the latter, it does not perform well in the former, and new solutions have to be found. Furthermore, most inverters have to be equipped with an output filter in order to remove the harmonic content of the switching PWM output and obtain a sinusoidal voltage. Connecting large numbers of inverters in parallel creates a complex and heavily coupled system with complicated dynamics.

The evolution of the electrical grid requires new control methodologies to ensure stability and power quality in the future. A significant challenge for control design in distribution grids is that the electrical parameters such as line resistance and inductance, or even the exact grid topology, are very uncertain, or even unknown. Therefore, a method is required that is able to consider robustness against these uncertainties as part of the design specifications. The method also needs to be able to accommodate very particular performance specifications such as proportional power sharing, decoupling or topology changes, which are often difficult to represent in classical approaches.

Furthermore, as advanced measurement devices (e.g. phasor measurement units) become more and more commonplace, the availability of real-time measurement data is increased significantly. This makes a data-driven paradigm very attractive, which allows the design of a controller purely based on measured data without requiring a parametric model of the system.

In light of the distributed nature of renewable generation units, a centralized controller is generally not practical. Therefore, a key requirement is the ability to design controllers with a distributed or decentralized structure. When considering distributed control, an important aspect are communication time delays, which should be considered in the design. Another important aspect is plug-and-play design, which allows the addition or withdrawal of individual generation units to or from a running grid.

Finally, the designed controllers should be practical and easy to implement. Notable features are low computational complexity (e.g. low controller order), and designing directly in discrete-time, which significantly reduces the number of intermediary steps from calculation to implementation. Since the majority of controllers used in practice are proportional-integral controllers with additional filters, the method should be able to design controllers of an equivalent form, which makes it relatable to practitioners.

1.2 Thesis Organization

As the thesis covers a wide and diverse range of topics, the corresponding state of the art is discussed at the start of each chapter. The chapters are organized as follows:

Chapter 2: Fixed-Structure Control Design using Frequency-Domain Data

In this chapter, a novel frequency-domain control design method for fixed-structure controllers is developed. The control specifications are formulated as H_∞ and H_2 constraints on any loop sensitivity transfer function. The constraints can be presented as convex-concave matrix inequality constraints, and a novel way to construct and solve the corresponding optimization problem is proposed. The main contributions are as follows:

- It is shown how the convex-concave problem can be linearized to obtain a convex optimization problem. An iterative approach is used, and it is shown that the solution converges to a locally optimal solution of the original problem.
- A proof for closed-loop stability based on the generalized Nyquist criterion is constructed.
- Only the frequency response of the plant is required for the design, which can be obtained either from a parametric model, or calculated from measurement data. This makes the method well-suited for high-order plants, and enables a purely data-driven approach.
- The controller is fully parametrized and covers a large range of representations (e.g. MIMO-PID with filters). The design can be either in continuous- or directly in discrete-time.
- Robustness against frequency-domain and multimodel uncertainty is straightforward to consider.

The method has also been published in *Automatica* [2].

Chapter 3: Frequency-Domain Modeling of Power Grids

A frequency-domain approach towards the modeling of voltage and current dynamics as well as power flow dynamics in low- and medium-voltage power grids is developed. The model is based on dynamic phasors and represents well the transient dynamics of the power flows, as well as the electromagnetic and electromechanic dynamics of inverters, synchronous generators and constant power loads. It also offers a straightforward way to combine white-box models from first-principle modeling with gray- and black-box models obtained from measurement data in the same framework. The model has been part of various publications [3–7].

Chapter 4: Current Control Design for Parallel Grid-Connected Inverters

In this chapter, the control design for multiple parallel, grid-connected inverters in a rural distribution grid is considered. It is shown how common performance specifications can be formulated as frequency-domain constraints, and using the method developed in Chapter 2 a decentralized controller is computed that guarantees stability and robust performance. Key contributions are:

- Whereas most approaches in the literature evaluate stability a posteriori, the proposed approach guarantees closed-loop stability and performance by design.

Chapter 1. Introduction

- The controller is robust against modeling uncertainties. It is also shown how robustness against changes in the grid topology can be considered as a multimodel uncertainty.
- An approach for plug-and-play control design is presented. The approach can be used to connect new distributed generation units to an existing grid while guaranteeing stability and performance.

The results are validated in numerical simulation as well as in power-hardware-in-the-loop experiments. This work has also been submitted for publication in [4].

Chapter 5: Distributed Primary and Secondary Control in Islanded Grids

This chapter treats the problem of robust control design for distributed primary and secondary frequency and voltage control of an islanded, meshed, low-voltage grid with multiple distributed generation units. The grid consists of several inverters, a synchronous machine and constant power loads, resulting in a general and realistic example. The method developed in Chapter 2 is then used to design a distributed controller that provides primary and secondary frequency and voltage control. The contributions are as follows:

- A distributed controller structure is proposed which provides primary and secondary frequency and voltage control in a unified framework.
- It is shown how non-standard performance specifications such as proportional power sharing, no frequency steady-state error and decoupling can be formulated as frequency-domain constraints on closed-loop sensitivity functions.
- The presented formulation is generic and makes no assumption on the resistance and inductance of the lines.
- Communication time delays are considered during the design.
- It is shown how robustness towards different grid layouts can be considered as multimodel uncertainty.

Extensive numerical simulation results demonstrate the potential of the approach. The results from this chapter have been published in [3, 5–7].

Chapter 6: Conclusion

This chapter states the concluding remarks and discusses possible future extensions of the research presented in this thesis.

Appendix A: Data-Driven Control Design for Atomic-Force Microscopy

This appendix presents an application of the developed control design method for data-driven control design for atomic force microscopes (AFMs). An AFM is a mechanical microscope with a resolution on the order of nanometers, and a wide range of applications in various fields such as solid-state physics, semiconductor science, molecular biology and cell biology. The data-driven method developed in Chapter 2 forms the core of an automated tool that allows a user to measure the plant response and design a controller within a few minutes, and without requiring any knowledge of control systems. This makes it possible to significantly reduce the time required to capture an image, while also improving the image quality. The initial results have been published in [8], and a more extensive dissemination is in progress.

Appendix B: Data-driven Multivariable Control of a 2-DOF Gyroscope

This appendix treats an experimental example where the design of a data-driven, robust multivariable controller with multimodel uncertainty is presented to control the gimbal angles of a gyroscope. The results show that the method is well suited for multivariable control design of strongly coupled systems under multimodel uncertainty, which is a challenging and relevant problem in many practical applications. The results are published in [9].

2 Fixed-Structure Control Design using Frequency-Domain Data

2.1 Introduction

Having been introduced in the early 1980s [10–12], the idea of applying H_∞ methods for robust control design has been an important area of research for a long time. Later, H_2 optimal design, which is a generalization of the well-known linear quadratic regulator design, was combined with H_∞ methods in a versatile framework [13, 14].

While these initially proposed methods are based on convex optimization and can be solved efficiently, they can only be used to compute full-order controllers (i.e. the controller is of the same order as the plant with the weighting filters). Furthermore, it is not possible to specify the controller structure, which makes the design of decentralized or distributed controllers impossible. This led to the concept of fixed-structure control, where the order and structure is fixed as part of the design specifications. Being able to fix a low-order controller as part of the specifications is a necessary feature for a method to be useful in practice. Similarly, enabling a fixed structure is especially important when considering networked systems, where a centralized controller is generally not practical, and a decentralized or distributed structure is required. As opposed to full-order design however, the resulting optimization problem for fixed-structure design is non-convex and nonsmooth, which presents a significant challenge. Current methods still suffer from various issues regarding complexity and implementability, which will be addressed in this chapter.

An additional obstacle is that in an industrial setting, since typical controller synthesis methods generally struggle with complex high-order models, the plant is often approximated by low-order models. This approximation can be difficult to find and limits the achievable performance, as the low-order models are subject to large uncertainty. A very attractive alternative is offered by methods that are able to synthesize a controller based only on the frequency response of the plant. This also enables a data-driven approach, where the frequency response is calculated from measured time- or frequency-domain data,

which eliminates the additional issues introduced by the system identification process. Data-driven methods do not suffer from any issues regarding unmodeled dynamics or parametric uncertainties, as the only source of uncertainty comes from the measurement noise and nonlinearity.

The recent developments in the fields of numerical optimization as well as computer and sensor technology have led to a significant reduction of the computational time of optimization algorithms, and have increased the availability of large amounts of measured data during a system's operation. These progresses make computationally demanding data-driven control design approaches a viable alternative to the classical model-based control problems. A survey on the differences between data-driven and model-based approaches has been made in [15], which asserts the advantages of this approach.

2.2 State of the Art

In this section, a review of the current literature on fixed-structure H_∞ and H_2 control design methods is presented.

2.2.1 State-Space Methods

A large part of fixed-structure methods in the literature relies on a parametric state-space model of the plant to design a fixed-structure state-space controller [16]. The methods can be separated into non-convex and convex approaches, depending on whether the robust control design problem is solved directly, or transformed into a convex approximation. The designed controllers are formulated as continuous-time state-space models, and generally need to be transformed to discrete-time to be implemented.

An early suggestion was to reformulate the non-convex problem using bilinear matrix inequalities (BMIs), but even moderately-sized problems proved numerically difficult [17, 18]. Non-smooth methods are used in [19–21] to directly solve the non-convex H_∞ design problem. This approach is also implemented in the Robust Control toolbox of Matlab under the `hinfstruct` command. A similar approach is used in the code package `HIF00`, which is able to also consider H_2 synthesis [22]. A downside of these implementations is that the performance specifications have to be expressed in a linear fractional transformation (LFT) form, which can make the choice of design parameters difficult and limits the design problems that can be expressed. Also, the use of non-smooth methods means that in practice every design step yields different results, which can be cumbersome.

To avoid the use of non-smooth methods, another approach is to convexify the problem and present sufficient conditions in terms of linear matrix inequalities (LMIs) [23–29]. The main drawback of these approaches is that they all rely on certain types of auxiliary

Lyapunov matrices, the size of which grows quadratically with the number of states of the plant. The resulting optimization problem can be hard to solve and the computation times are very high for high-order systems.

2.2.2 Methods using Frequency-Domain Data

Another direction is robust control design based only on frequency-domain data instead of a parametric plant model. This approach has two significant advantages compared to state-space methods: first, only the frequency response is required for the design, so the order of the plant has no effect on the computational complexity of the design algorithm. This means that accurate, high-order models can be used, which improves the robustness and achievable performance. Second, it is straightforward to measure the frequency response of a plant directly (e.g. using sweeps), or to compute it from time-domain measurement data. This is very attractive in practice, as it allows for a data-driven approach and makes it unnecessary to identify a parametric model, which is often a complicated process.

In [30, 31] a method for SISO systems based on Q-parametrization is proposed, where the H_∞ problem is linearized around an initial stabilizing controller to obtain a convex optimization problem. Other approaches are based on linearly parametrized (LP) controllers for SISO systems, where the controller is expressed as a linear combination of some basis functions in transfer-function form. Convex methods to design LP controllers with a desired gain and phase margin have been proposed in [32, 33]. Further, a method to design LP controllers with loop shaping or H_∞ performance has been developed in [34–36], and is extended to MIMO systems in [37] with the use of Gershgorin bands. These methods are based on the linearization of the constraints around a desired open-loop transfer function and have already been applied to industrial systems [36, 38–40] using a public domain toolbox [41].

A loop-shaping method has been proposed in [42], where the H_∞ problem for MIMO systems is considered by imposing multiple line constraints in the Nyquist diagram to achieve stability and performance. However, the proposed constraints become convex only for special cases of LP controllers.

Another approach for the robust design of LP-MIMO state-space controllers is presented in [43]. A method to design MIMO-PID controllers was developed in [44, 45], where a convex-concave optimization problem is linearized around an initial controller to obtain a convex optimization problem with LMI constraints. However, the controller structure is limited to PID, and no proof of stability is given in these papers. The method is further extended in [46] and applied in [47]. In [48] a non-smooth method is used to directly solve the convex-concave optimization problem to compute fixed-structure controllers, where stability is achieved through the iterative tuning of barrier functions. It is important

to note that a limitation of the approaches discussed in this paragraph is that the performance can only be specified in the H_∞ and not in the H_2 sense.

2.3 Frequency response data

The system to be controlled is a Linear Time-Invariant Multi-Input Multi-Output (LTI-MIMO) system, and is represented very generally by a multivariable frequency response model $G(j\omega) \in \mathbb{C}^{n \times m}$, where n is the number of outputs and m the number of inputs. The frequency response $G(j\omega)$ is assumed to be bounded in all frequencies except for a set B_g including a finite number of frequencies that correspond to the poles of G on the stability boundary (the imaginary axis for continuous-time, or the unit circle for discrete-time systems).

The frequency response can be obtained from a parametric model by evaluating:

$$G(j\omega) = G(s = j\omega), \quad \omega \in \Omega_g = \{\omega \mid -\infty < \omega < \infty\} \setminus B_g \quad (2.1)$$

$$G(j\omega) = G(z = e^{j\omega T_s}), \quad \omega \in \Omega_g = \left\{ \omega \mid -\frac{\pi}{T_s} \leq \omega \leq \frac{\pi}{T_s} \right\} \setminus B_g \quad (2.2)$$

for continuous-time and discrete-time models respectively, where T_s is the sampling time. A notable advantage of frequency response models as compared to state-space models is that time-delays can be considered exactly, and no approximation is required.

Following a data-driven approach, the frequency response model can also be identified directly from time-domain measurement data using the Fourier analysis method from m sets of input/output sampled data as [49]:

$$G(j\omega) = \left[\sum_{k=0}^{N-1} y(k) e^{-j\omega T_s k} \right] \left[\sum_{k=0}^{N-1} u(k) e^{-j\omega T_s k} \right]^{-1} \quad (2.3)$$

$$\omega \in \Omega_g = \left\{ \omega \mid -\frac{\pi}{T_s} \leq \omega \leq \frac{\pi}{T_s} \right\} \setminus B_g \quad (2.4)$$

where N is the number of data points for each experiment, $u(k) \in \mathbb{R}^{m \times 1}$ includes the inputs at instant k , $y(k) \in \mathbb{R}^{n \times 1}$ the outputs at instant k and T_s is the sampling period. Note that at least m different experiments are needed to extract G from the data (each column of $u(k)$ and $y(k)$ represents respectively the input and the output data from one experiment). In order to obtain an accurate model, the input data should have a rich frequency spectrum such as e.g. a PRBS signal, a sum of sinusoids or a frequency sweep. The main advantage of directly using frequency-domain data is that a parametric model of the plant is not required, and there are no unmodeled dynamics. The only source of uncertainty for an LTI system is the measurement noise, whose influence can be reduced significantly if the amount of measurement data is large.

2.4 Controller Structure

A fixed-structure matrix transfer function controller is designed. The controller is fully parametrized, which greatly simplifies the choice of controller structure and order as opposed to linearly parametrized approaches. The controller is defined as $K = XY^{-1}$, where X and Y are polynomial matrices in s for continuous-time or in z for discrete-time controller design. This controller structure, therefore, can be used for both continuous-time or discrete-time controllers. The matrix X has the following structure:

$$X = \begin{bmatrix} X_{11} & \dots & X_{1n} \\ \vdots & \ddots & \vdots \\ X_{m1} & \dots & X_{mn} \end{bmatrix} \circ F_x \quad (2.5)$$

where X and F_x are $m \times n$ polynomial matrices and \circ denotes the element by element multiplication of matrices. The matrix F_x represents the fixed known terms in the controller that are designed to have specific performance, e.g. based on the internal model principle, or communication time delays of distributed controllers. For discrete- and continuous-time controllers we have respectively:

$$X(z) = (X_p z^p + \dots + X_1 z + X_0) \circ F_x(z) \quad (2.6)$$

$$X(s) = (X_p s^p + \dots + X_1 s + X_0) \circ F_x(s) \quad (2.7)$$

where $X_i \in \mathbb{R}^{m \times n}$ for $i = 0, \dots, p$ contain the controller parameters. In the same way the matrix polynomial Y can be defined as:

$$Y = \begin{bmatrix} Y_{11} & \dots & Y_{1n} \\ \vdots & \ddots & \vdots \\ Y_{n1} & \dots & Y_{nn} \end{bmatrix} \circ F_y \quad (2.8)$$

where Y and F_y are $n \times n$ polynomial matrices. The matrix F_y represents the fixed terms of the controller, e.g. integrators or the denominator of other disturbance models. The set of frequencies of all roots of the elements of F_y on the stability boundary (imaginary axis for continuous-time controllers or the unit circle for the discrete-time case) is denoted by B_y . For discrete- and continuous-time controllers we have respectively:

$$Y(z) = (I z^p + Y_{p-1} z^{p-1} + \dots + Y_1 z + Y_0) \circ F_y(z) \quad (2.9)$$

$$Y(s) = (I s^p + Y_{p-1} s^{p-1} + \dots + Y_1 s + Y_0) \circ F_y(s) \quad (2.10)$$

where $Y_i \in \mathbb{R}^{n \times n}$ for $i = 0, \dots, p-1$ contain the controller parameters. In order to obtain low-order controllers, a diagonal structure can be considered for Y , which also simplifies its inversion and implementation. Note that $Y(j\omega)$ should be invertible for all $\omega \in \Omega = \Omega_g \setminus B_y$.

This controller structure is very general and covers centralized, decentralized and distributed control structures, as will be shown in the following examples.

Example - PI controller with Lead/Lag compensators: A very well-known structure that can be represented is a SISO-PI controller with filters. For example, a PI with two lead/lag compensators can be expressed as a third-order transfer function with fixed integrator:

$$\underbrace{\left(k_p + k_i \frac{1}{z-1}\right)}_{\text{PI}} \underbrace{\frac{z-b_1}{z-a_1} \frac{z-b_2}{z-a_2}}_{\text{lead/lag lead/lag}} = \frac{X_1 z^3 + X_2 z^2 + X_1 z + x_0}{(z^2 + Y_1 z + Y_0) \cdot (z-1)} = \frac{X(z)}{Y(z)} \quad (2.11)$$

Example - Decentralized PI controller: Assume a multivariable system with 3 devices (e.g. 3 motors), where each device has a single input and a single output. To design a decentralized PI controller, the following structure can be chosen:

$$X(z) = \begin{bmatrix} X_1^{11}z + X_0^{11} & 0 & 0 \\ 0 & X_1^{22}z + X_0^{22} & 0 \\ 0 & 0 & X_1^{33}z + X_0^{33} \end{bmatrix}$$

$$Y(z) = \begin{bmatrix} 1 & 0 & 0 \\ 0 & 1 & 0 \\ 0 & 0 & 1 \end{bmatrix} \circ \begin{bmatrix} z-1 & 0 & 0 \\ 0 & z-1 & 0 \\ 0 & 0 & z-1 \end{bmatrix} \quad (2.12)$$

Example - Distributed second-order controller: Assume a multivariable system with 3 devices, where each device has a single input and a single output. The first and the third device are able to communicate with each other, whereas the second device only uses its local measurements. Then, a distributed second-order controller can be defined as:

$$X(z) = \begin{bmatrix} X_2^{11}z^2 + X_1^{11}z + X_0^{11} & 0 & X_2^{13}z^2 + X_1^{13}z + X_0^{13} \\ 0 & X_2^{22}z^2 + X_1^{22}z + X_0^{22} & 0 \\ X_2^{31}z^2 + X_1^{31}z + X_0^{31} & 0 & X_2^{33}z^2 + X_1^{33}z + X_0^{33} \end{bmatrix}$$

$$Y(z) = \begin{bmatrix} Iz^2 + Y_1^{11}z + Y_0^{11} & 0 & 0 \\ 0 & Iz^2 + Y_1^{22}z + Y_0^{22} & 0 \\ 0 & 0 & Iz^2 + Y_1^{33}z + Y_0^{33} \end{bmatrix} \quad (2.13)$$

2.5 Control Performance

In this section it is shown how classical H_2 and H_∞ control performance constraints can be transformed to constraints on the spectral norm of the system, which take the

following quadratic matrix inequality form:

$$F^* \gamma^{-1} F - P^* P < 0 \quad (2.14)$$

where $F \in \mathbb{C}^{n \times n}$ and $P \in \mathbb{C}^{n \times n}$ are linear in the optimization variables, $\gamma \in \mathbb{R}$ is an auxiliary variable and $(\cdot)^*$ denotes the complex conjugate transpose. This type of constraint is called a convex-concave constraint and can be convexified using the Taylor expansion of $P^* P$ around $P_c \in \mathbb{C}^{n \times n}$ which is an arbitrary known matrix [50]:

$$P^* P \approx P_c^* P_c + (P - P_c)^* P_c + P_c^* (P - P_c) \quad (2.15)$$

It is easy to show that under the following linear matrix inequality (LMI) the left hand side term is always greater than or equal to the right hand side term:

$$0 \leq (P - P_c)^* (P - P_c) \rightarrow P^* P \geq P_c^* P_c + P_c^* P - P_c^* P_c \quad (2.16)$$

Then, using the Schur complement the LMI from (2.14) can be written as a convex constraint:

$$\begin{bmatrix} P_c^* P_c + P_c^* P - P_c^* P_c & F^* \\ F & \gamma I \end{bmatrix} > 0 \quad (2.17)$$

The following sections will derive the convex formulation of several performance specifications commonly used in robust control. However, it should be noted that the method is not restricted only to the presented specifications. Essentially, any H_∞ or H_2 objective on any weighted transfer function can be realized in the presented framework, which results in a very flexible and powerful tool that is suitable for a wide range of applications.

Furthermore, the performance objectives are generally specified through weighting filters $W(j\omega)$. These weighting filters can be defined e.g. as transfer functions, scalar values, or even arbitrary non-smooth functions such as piece-wise continuous functions, which greatly simplifies the problem formulation.

2.5.1 H_∞ Performance

Constraints on the infinity-norm of any weighted sensitivity function can be considered. For example, consider the following design objective:

$$\min_K \| W_1 S \|_\infty \quad (2.18)$$

Chapter 2. Fixed-Structure Control Design using Frequency-Domain Data

where $S = (I + GK)^{-1}$ is the sensitivity function and W_1 is a performance weight. Using the fact that the infinity norm of a system is equal to:

$$\|H\|_\infty = \max_{\omega \in \Omega} \sigma_{\max}(H(j\omega)) \quad (2.19)$$

where σ_{\max} is the maximum singular value of a matrix, this problem can be converted to an optimization problem on the spectral norm as:

$$\begin{aligned} & \min_K \gamma \\ & \text{subject to:} \\ & (W_1 S)^*(W_1 S) < \gamma I, \quad \forall \omega \in \Omega \end{aligned} \quad (2.20)$$

where $\gamma \in \mathbb{R}$ is an auxiliary scalar variable. Note that the argument $j\omega$ has been omitted for $W_1(j\omega)$, $S(j\omega)$ and $K(j\omega)$ in order to simplify the notation. The above constraint can be rewritten as:

$$[W_1(I + GK)^{-1}]^*[W_1(I + GK)^{-1}] < \gamma I \quad (2.21)$$

and converted to a convex-concave constraint as follows:

$$Y^* W_1^* \gamma^{-1} W_1 Y - (Y + GX)^*(Y + GX) < 0 \quad (2.22)$$

We denote $P = Y + GX$, and define an initial controller $K_c = X_c Y_c^{-1}$. Then, using (2.16) a convex approximation of the constraint can be obtained around $P_c = Y_c + G X_c$ as:

$$Y^* W_1^* \gamma^{-1} W_1 Y - P^* P_c - P_c^* P + P_c^* P_c < 0 \quad (2.23)$$

Now, using the Schur complement lemma, the H_∞ problem can be represented as the following convex optimization problem with linear matrix inequalities (LMIs):

$$\begin{aligned} & \min_{X, Y} \gamma \\ & \text{subject to:} \\ & \begin{bmatrix} P^* P_c + P_c^* P - P_c^* P_c & (W_1 Y)^* \\ W_1 Y & \gamma I \end{bmatrix} > 0, \quad \forall \omega \in \Omega \end{aligned} \quad (2.24)$$

This convex constraint is a sufficient condition for the spectral constraint in (2.20) for any choice of initial controller $K_c = X_c Y_c^{-1}$.

Analogously, the following H_∞ constraints on the weighted closed-loop sensitivity functions:

$$\|W_2 T\|_\infty < 1, \quad \|W_3 U\|_\infty < 1 \quad (2.25)$$

where $T = GK(I + GK)^{-1}$, $U = K(I + GK)^{-1}$ can be expressed as:

$$\begin{bmatrix} P^*P_c + P_c^*P - P_c^*P_c & (W_2GX)^* \\ W_2GX & I \end{bmatrix} > 0, \forall \omega \in \Omega \quad (2.26)$$

$$\begin{bmatrix} P^*P_c + P_c^*P - P_c^*P_c & (W_3X)^* \\ W_3X & I \end{bmatrix} > 0, \forall \omega \in \Omega \quad (2.27)$$

Another classical example is the mixed sensitivity problem:

$$\min_K \left\| \begin{bmatrix} W_1S \\ W_3KS \end{bmatrix} \right\|_\infty \quad (2.28)$$

which can be written as:

$$\begin{aligned} & \min_{X,Y} \gamma \\ & \text{subject to:} \\ & \begin{bmatrix} P^*P_c + P_c^*P - P_c^*P_c & (W_1Y)^* & (W_3X)^* \\ W_1Y & \gamma I & 0 \\ W_3X & 0 & \gamma I \end{bmatrix} > 0, \forall \omega \in \Omega \end{aligned} \quad (2.29)$$

2.5.2 H_2 Performance

The method can also accommodate H_2 control performance objectives. As an example, consider the following H_2 control performance for a stable, discrete-time system:

$$\min_K \|W_1SW_2\|_2^2 = \min_K \int_{-\frac{\pi}{T_s}}^{\frac{\pi}{T_s}} \text{trace}[(W_1(I + GK)^{-1}W_2)^*W_1(I + GK)^{-1}W_2]d\omega \quad (2.30)$$

where the weighting filter W_2 is invertible for all frequencies $\omega \in \Omega$. This is equivalent to:

$$\begin{aligned} & \min_K \int_{-\frac{\pi}{T_s}}^{\frac{\pi}{T_s}} \text{trace}[\Gamma(\omega)]d\omega \\ & \text{subject to:} \end{aligned} \quad (2.31)$$

$$(W_1(I + GK)^{-1}W_2)^* (W_1(I + GK)^{-1}W_2) < \Gamma(\omega), \forall \omega \in \Omega$$

where $\Gamma(\omega) > 0$ is an unknown matrix function $\in \mathbb{R}^{n \times n}$. Replacing K with XY^{-1} , we obtain:

$$W_1Y \left((W_2^{-1}(Y + GX))^*(W_2^{-1}(Y + GX)) \right)^{-1} (W_1Y)^* \leq \Gamma(\omega) \quad (2.32)$$

Chapter 2. Fixed-Structure Control Design using Frequency-Domain Data

which, using the Schur complement lemma, is equivalent to the following quadratic matrix inequality:

$$\begin{bmatrix} \Gamma & W_1 Y \\ (W_1 Y)^* & (W_2^{-1}(Y + GX))^*(W_2^{-1}(Y + GX)) \end{bmatrix} (j\omega) \geq 0 \quad (2.33)$$

We denote $P_{W_2} = W_2^{-1}(Y + GX)$, and define an initial controller $K_c = X_c Y_c^{-1}$. Then, the quadratic part can be linearized around $P_{c,W_2} = W_2^{-1}(Y_c + GX_c)$ using (2.16) to obtain a linear matrix inequality, which leads to the following convex problem:

$$\begin{aligned} & \min_K \int_{-\frac{\pi}{T_s}}^{\frac{\pi}{T_s}} \text{trace}[\Gamma(\omega)] d\omega \\ & \text{subject to:} \\ & \begin{bmatrix} \Gamma & W_1 Y \\ (W_1 Y)^* & P_{W_2}^* P_{c,W_2} + P_{c,W_2}^* P_{W_2} - P_{c,W_2}^* P_{c,W_2} \end{bmatrix} (j\omega) > 0, \quad \forall \omega \in \Omega \end{aligned} \quad (2.34)$$

Remark: The unknown function $\Gamma(\omega)$ can be approximated by a polynomial function of finite order as:

$$\Gamma(\omega) = \Gamma_0 + \Gamma_1 \omega + \dots + \Gamma_h \omega^h \quad (2.35)$$

In case the constraints are evaluated for a finite set of frequencies $\Omega_N = \{\omega_1, \dots, \omega_N\}$, $\Gamma(\omega)$ can also be replaced with a matrix variable Γ_k at each frequency ω_k .

2.5.3 Loop shaping

Assume that a desired loop transfer function L_d is available and that the objective is to design a controller K such that the loop transfer function $L = GK$ is close to L_d in the 2- or ∞ -norm sense. The objective function for the ∞ -norm case is to minimize:

$$\min_K \|L - L_d\|_\infty \quad (2.36)$$

and can be expressed as follows:

$$\begin{aligned} & \min_K \gamma \\ & \text{subject to:} \\ & (GK - L_d)^*(GK - L_d) < \gamma I, \quad \forall \omega \in \Omega \end{aligned} \quad (2.37)$$

Replacing K with XY^{-1} in the constraint, we obtain:

$$(GX - L_d Y)^* \gamma^{-1} (GX - L_d Y) - Y^* Y < 0 \quad (2.38)$$

Again Y^*Y can be linearized around Y_c using the linear approximation in (2.16). Thus, the following convex formulation is obtained:

$$\begin{aligned} & \min_{X,Y} \gamma \\ & \text{subject to:} \\ & \begin{bmatrix} Y^*Y_c + Y_c^*Y - Y_c^*Y_c & (GX - L_dY)^* \\ GX - L_dY & \gamma I \end{bmatrix} > 0, \forall \omega \in \Omega \end{aligned} \quad (2.39)$$

In a similar way, minimizing:

$$\min_K \|L - L_d\|_2^2 \quad (2.40)$$

can be written as:

$$\begin{aligned} & \min_{X,Y} \int_{-\frac{\pi}{T_s}}^{\frac{\pi}{T_s}} \text{trace}[\Gamma(\omega)] d\omega \\ & \text{subject to:} \\ & (GK - L_d)^*(GK - L_d) < \Gamma(\omega), \forall \omega \in \Omega \end{aligned} \quad (2.41)$$

The constraint can be written as:

$$(GX - L_dY)(Y^*Y)^{-1}(GX - L_dY)^* < \Gamma(\omega) \quad (2.42)$$

and using (2.16) to linearize Y^*Y around Y_c , the following convex optimization problem can be solved:

$$\begin{aligned} & \min_{X,Y} \int_{-\frac{\pi}{T_s}}^{\frac{\pi}{T_s}} \text{trace}[\Gamma(\omega)] d\omega \\ & \text{subject to:} \\ & \begin{bmatrix} \Gamma(\omega) & (GX - L_dY)^* \\ GX - L_dY & Y^*Y_c + Y_c^*Y - Y_c^*Y_c \end{bmatrix} > 0, \forall \omega \in \Omega \end{aligned} \quad (2.43)$$

2.6 Stability Analysis

The stability of the closed-loop system is not necessarily guaranteed even if the spectral norm of a weighted sensitivity function is bounded. In fact, an unstable system with no pole on the stability boundary has a bounded spectral norm. In this section, we show that the closed-loop stability can be guaranteed if some conditions in the linearization of the constraints are met. More precisely, the initial controller $K_c = X_c Y_c^{-1}$ plays an important role in guaranteeing the stability of the closed-loop system with the resulting controller K .

2.6.1 A detailed look at the Nyquist Criterion

Our stability analysis is based on the generalized Nyquist stability criterion for MIMO systems that is recalled here [51].

Theorem 1 (Nyquist stability theorem) *The closed-loop system with the plant model G and the controller K is stable if and only if GK has no unstable hidden modes¹, and the Nyquist plot of $\det(I + GK)$*

1. *makes $N_G + N_K$ clockwise encirclements of the origin, where N_G and N_K are the number of unstable poles of G and K , and*
2. *does not pass through the origin.*

The Nyquist plot is the image of $\det(I + GK)$ as s or z traverses the Nyquist contour counterclockwise. We assume that the Nyquist contour has some small detours around the poles of G and K on the stability boundary.

Definition 1 *Let $F(s)$ or $F(z)$ be a continuous- or discrete-time transfer function. Let $\text{wno}\{F\}$ be the winding number, in the counterclockwise sense, of the image of F around the origin when s or z traverses the Nyquist contour in the counterclockwise direction with some small detours around the poles of F on the stability boundary.*

Since the winding number is related to the phase of the complex function, we have the following properties:

$$\text{wno}\{F_1 F_2\} = \text{wno}\{F_1\} + \text{wno}\{F_2\} \quad (2.44)$$

$$\text{wno}\{F\} = -\text{wno}\{F^*\} \quad (2.45)$$

$$\text{wno}\{F\} = -\text{wno}\{F^{-1}\} \quad (2.46)$$

The Nyquist contours for the continuous- and discrete-time case are shown in Figs. 2.1a and 2.1b. It can be seen that since the discrete-time contour must encircle the exterior of the unit circle, it contains not only the unit circle, but also an additional circle of infinite radius. It is also assumed the contour makes a small detour around any poles on the stability boundary.

¹A hidden unstable mode is an unstable pole of GK that does not appear in $\det(GK)$. An example are pole-zero cancellations, or the following transfer function:

$$GK = \begin{bmatrix} \frac{1}{s+1} & \frac{1}{s-1} \\ 0 & \frac{1}{s+2} \end{bmatrix}$$

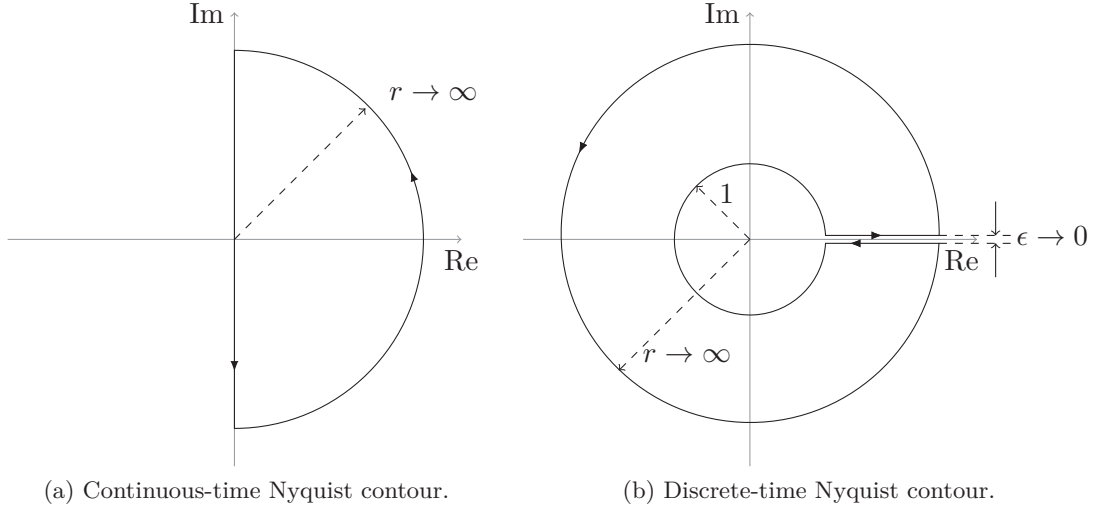


Figure 2.1 – Nyquist contours.

If GK has no unstable hidden modes, the unstable poles and zeros of $\det(I + GK)$ are equal to the unstable poles and zeros of G and K . Furthermore, the unstable zeros of $\det(I + GK)$ are also the unstable poles of the closed-loop system. Then, according to Cauchy's argument principle, the Nyquist plot satisfies:

$$\text{wno}(\det(I + GK)) = N_Z - (N_G + N_K) \quad (2.47)$$

where N_G, N_K are the number of unstable poles of G and K , and N_Z is the number of unstable zeros of $\det(I + GK)$.

Therefore, stability is guaranteed if N_Z is zero (i.e. if the closed-loop system does not contain any unstable poles):

$$\begin{aligned} N_Z &= (N_G + N_K) + \text{wno}(\det(I + GK)) = 0 \\ &\rightarrow -\text{wno}(\det(I + GK)) = N_G + N_K \end{aligned} \quad (2.48)$$

which leads to the Nyquist criterion formulated above.

For the discrete-time case, it is also possible to simplify the Nyquist contour by encircling the *stable* poles and zeros instead. Then, the contour reduces to only the unit circle in the counterclockwise direction (see Fig. 2.2). Note that this is opposed to the contour in Fig. 2.1b, where the unit circle is traversed clockwise. Cauchy's argument principle now leads to:

$$\text{wno}(\det(I + GK)) = N_Z^{\text{stab}} - (N_G^{\text{stab}} + N_K^{\text{stab}}) \quad (2.49)$$

where $N_Z^{\text{stab}}, N_G^{\text{stab}}, N_K^{\text{stab}}$ are the number of stable zeros and poles. Now, let p be the

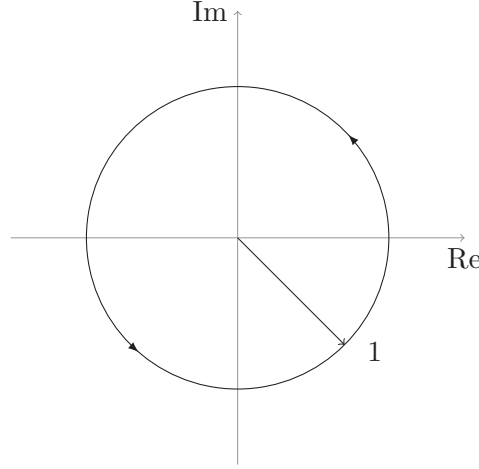


Figure 2.2 – Simplified discrete-time Nyquist contour.

order of the numerator and denominator of $\det(I + GK)$). Then, closed-loop stability is guaranteed if and only if:

$$\begin{aligned} N_Z = p - N_Z^{\text{stab}} &= p - (N_G^{\text{stab}} + N_K^{\text{stab}}) - \text{wno}(\det(I + GK)) = 0 \\ \rightarrow \text{wno}(\det(I + GK)) &= p - (N_G^{\text{stab}} + N_K^{\text{stab}}) = N_G + N_K \end{aligned} \quad (2.50)$$

It should be noted that in this case the direction of the encirclements in the Nyquist theorem changes to *counterclockwise*.

2.6.2 Stability Proof - Discrete-Time

Using the generalized Nyquist criterion, we can now show under which conditions closed-loop stability is guaranteed in the discrete-time case. The continuous-time proof is almost analogous to the discrete-time case, and is given in Appendix 2.A.

Theorem 2 *Given a plant model G , an initial stabilizing controller $K_c = X_c Y_c^{-1}$ with $\det(Y_c) \neq 0, \forall \omega \in \Omega$, and feasible solutions X and Y to the following LMI,*

$$\underbrace{(Y + GX)^*}_{P} \underbrace{(Y_c + GX_c)}_{P_c} + (Y_c + GX_c)^* (Y + GX) > 0 \quad (2.51)$$

for all $\omega \in \Omega$, then the controller $K = XY^{-1}$ stabilizes the closed-loop system if and only if

1. $\det(Y) \neq 0, \forall \omega \in \Omega$.
2. *The initial controller K_c and the final controller K share the same poles on the stability boundary, i.e. $\det(Y) = \det(Y_c) = 0, \forall \omega \in B_y$.*

3. The order of $\det(Y)$ is equal to the order of $\det(Y_c)$.

Remark: Note that the condition in (2.51) is always met when a convexified H_∞ or H_2 control problem has a feasible solution because $P^*P_c + P_c^*P > 0$ is included in the constraints.

Proof: The proof is based on the discrete-time Nyquist stability criterion using only the unit circle as the contour (see Fig. 2.2), and the properties of the winding number. Then, the winding number of the determinant of $P^*(z)P_c(z)$ is given by:

$$\begin{aligned} \text{wno}\{\det(P^*P_c)\} &= \text{wno}\{\det(P^*)\} + \text{wno}\{\det(P_c)\} \\ &= -\text{wno}\{\det(I + GK)\det(Y)\} + \text{wno}\{\det(I + GK_c)\det(Y_c)\} \\ &= -\text{wno}\{\det(I + GK)\} \\ &\quad -\text{wno}\{\det(Y)\} + \text{wno}\{\det(Y_c)\} + \text{wno}\{\det(I + GK_c)\} \end{aligned} \quad (2.52)$$

Note that the phase variation of $\det(P^*P_c)$ for the small detour in the Nyquist contour is zero, if Condition 2 of the theorem is satisfied. In fact, for each small detour, the Nyquist plot of $\det(I + GK)$ and $\det(I + GK_c)$ will have the same phase variation because K and K_c share the same poles on the unit circle. As a result, the winding number of $\det(P^*P_c)$ can be evaluated on Ω instead of the complete Nyquist contour. Furthermore, the condition in (2.51) implies that $P^*(e^{j\omega})P_c(e^{j\omega})$ is a non-Hermitian positive definite matrix in the sense that :

$$\Re\{x^*P^*(e^{j\omega})P_c(e^{j\omega})x\} > 0 \quad \forall x \neq 0 \in \mathbb{C}^n \quad (2.53)$$

and $\forall \omega \in \Omega$. This, in turn, means that all eigenvalues of $P^*(e^{j\omega})P_c(e^{j\omega})$, denoted $\lambda_i(\omega)$ for $i = 1, \dots, n$, have positive real parts at all frequencies [52]:

$$\Re\{\lambda_i(\omega)\} > 0 \quad \forall \omega \in \Omega, i = 1, \dots, n \quad (2.54)$$

Therefore, $\lambda_i(\omega)$ will not pass through the origin and not encircle it (i.e. its winding number is zero). As a result, since the determinant of a matrix is the product of its eigenvalues, we have:

$$\text{wno}\{\det(P^*P_c)\} = \text{wno}\left\{\prod_{i=1}^n \lambda_i\right\} = \sum_{i=1}^n \text{wno}\{\lambda_i\} = 0$$

Since K_c is a stabilizing controller, from (2.49) we have $\text{wno}\{\det(I + GK_c)\} = N_G + N_{K_c}$. Furthermore, $\text{wno}\{\det(Y)\} = N_K^{\text{stab}} = \delta - N_K$ and $\text{wno}\{\det(Y_c)\} = N_{K_c}^{\text{stab}} = \delta - N_{K_c}$, where δ is the order of $\det(Y)$ and $\det(Y_c)$ according to Condition 3. Now using (2.52),

we obtain:

$$\begin{aligned} \text{wno}\{\det(I + GK)\} &= \text{wno}\{\det(I + GK_c)\} - \text{wno}\{\det(Y)\} + \text{wno}\{\det(Y_c)\} \\ &= N_G + N_K \end{aligned} \quad (2.55)$$

which shows that Condition 1 of the Nyquist theorem is met.

We can also see from (2.54) that

$$\det(P^*P_c) = \prod_{i=1}^n \lambda_i(\omega) \neq 0 \quad \forall \omega \in \Omega \quad (2.56)$$

Therefore, $\det(P) = \det(I + GK) \det(Y) \neq 0$ and the Nyquist plot of $\det(I + GK)$ does not pass through the origin and Condition 2 of the Nyquist theorem is also satisfied. ■

Remark 1: A necessary and sufficient condition for $\det(Y) \neq 0$ is $Y^*Y > 0$. Since this constraint is concave, it can be linearized to obtain the following sufficient LMI:

$$Y^*Y_c + Y_c^*Y - Y_c^*Y_c > 0 \quad (2.57)$$

Remark 2: In practice, condition 3 of Theorem 2 is not restrictive. Any initial controller of lower order than the final controller can be augmented e.g. by adding an appropriate number of zeros and poles at the origin in X_c and Y_c , thus satisfying the condition without affecting the initial controller.

2.6.3 Multimodel uncertainty

The case of robust control design with multimodel uncertainty is very easy to incorporate in the given framework. Systems that have different frequency responses in q different operating points can be represented by a multimodel uncertainty set:

$$\mathcal{G}(j\omega) = \{G_1(\omega), G_2(\omega), \dots, G_q(j\omega)\} \quad (2.58)$$

Note that the models may have different orders and may contain pure input/output time delays.

This can be implemented by formulating a different set of constraints for each of the models. Let $P_i = Y + G_iX$ and $P_{c_i} = X_{c,i} + G_iY_{c,i}$, where $K_{c,i}$ is a stabilizing controller for model G_i . Again taking the mixed sensitivity problem from (2.29) as an example,

the formulation of this problem including the stability constraint would be:

$$\begin{aligned}
& \min_{X,Y} \gamma \\
& \text{subject to:} \\
& \begin{bmatrix} P_i^* P_{c_i} + P_{c_i}^* P_i - P_{c_i}^* P_{c_i} & (W_1 Y)^* & (W_2 X)^* \\ W_1 Y & \gamma I & 0 \\ W_2 X & 0 & \gamma I \end{bmatrix} > 0 \\
& Y^* Y_c + Y_c^* Y - Y_c^* Y_c > 0 \\
& \text{for } i = 1, \dots, q \quad ; \quad \forall \omega \in \Omega
\end{aligned} \tag{2.59}$$

2.6.4 Frequency-domain uncertainty

The frequency function may be affected by the measurement noise. In this case, the model uncertainty can be represented as :

$$\tilde{G}(\omega) = G(j\omega) + W_1(j\omega)\Delta W_2(j\omega) \tag{2.60}$$

where Δ is the unit ball of matrices of appropriate dimension and $W_1(j\omega)$ and $W_2(j\omega)$ are known complex matrices that specify the magnitude of and directional information about the measurement noise. A convex optimization approach is proposed in [53] to compute the optimal uncertainty filters from the frequency-domain data. The system identification toolbox of Matlab provides the variance of $G_{ij}(j\omega)$ (the frequency function between the i -th output and the j -th input) from the estimates of the noise variance that can be used for computing W_1 and W_2 .

The robust stability condition for this type of uncertainty is [54]: $\|W_2 K S W_1\|_\infty < 1$. If $W_1(j\omega)$ is in parametric transfer function form, it must be invertible for all $\omega \in \Omega$. If it is computed as frequency-domain data from measurements, it should be invertible at each calculated frequency point. Then a set of robustly stabilizing controllers can be given by the following spectral constraints:

$$\begin{aligned}
& \begin{bmatrix} P^* P_c + P_c^* P - P_c^* P_c & (W_2 X)^* \\ W_2 X & I \end{bmatrix} > 0 \\
& Y^* Y_c + Y_c^* Y - Y_c^* Y_c > 0 \quad ; \quad \forall \omega \in \Omega
\end{aligned} \tag{2.61}$$

where $P = W_1^{-1}(Y + GX)$ and $P_c = W_1^{-1}(Y_c + GX_c)$.

2.7 Implementation

Using the methods described above, we are now able to pose various control design problems as convex optimization problems with linear matrix inequality (LMI) constraints.

In this section, various practical aspects concerning the implementation of the algorithm will be discussed.

2.7.1 Frequency Gridding

The optimization problems formulated in this paper contain an infinite number of constraints (i.e. $\forall \omega \in \Omega$) and are called semi-infinite problems. A common approach to handle this type of constraints is to choose a reasonably large set of frequency samples $\Omega_N = \{\omega_1, \dots, \omega_N\}$ and replace the constraints with a finite set of constraints at each of the given frequencies. For discrete-time plants and/or controllers, the maximum frequency should be chosen as $\omega_N = \pi/T_s$. As the complexity of the problem scales linearly with the number of constraints, N can be chosen relatively large without severely impacting the solver time. The frequency range is usually gridded logarithmically-spaced. Since all constraints are applied to Hermitian matrices, any constraint at a frequency ω_i is automatically imposed at $-\omega_i$ as well, meaning the grid does not need to cover negative frequencies.

In some applications with low-damped resonance frequencies, the density of the frequency points can be increased around the resonant frequencies to prevent constraint violations. An alternative is to use a randomized approach for the choice of the frequencies at which the constraints are evaluated [55]. In this case, the probability of the violation of the constraints can be computed, and decreased by increasing the number of frequency points.

Two examples of the formulation of the gridded optimization problem are given below.

Mixed Sensitivity: The sampled mixed sensitivity problem from (2.29) with the additional stability constraint would be:

$$\begin{aligned}
 & \min_{X,Y} \gamma \\
 & \text{subject to:} \\
 & \begin{bmatrix} P^*P_c + P_c^*P - P_c^*P_c & (W_1Y)^* & (W_2X)^* \\ W_1Y & \gamma I & 0 \\ W_2X & 0 & \gamma I \end{bmatrix} (j\omega_k) > 0 \\
 & \begin{bmatrix} Y^*Y_c + Y_c^*Y - Y_c^*Y_c \end{bmatrix} (j\omega_k) > 0, \quad \omega_k \in \Omega_N
 \end{aligned} \tag{2.62}$$

H_2 Performance: The H_2 performance objective from (2.34) can be formulated by approximating $\Gamma(\omega)$ by a matrix variable $\Gamma_k \in \{\Gamma_1, \dots, \Gamma_N\}$ at each frequency $\omega_k \in \Omega_N$. Then, the integral in the objective function can be replaced by the sum of the matrix

variables as follows:

$$\min_{X,Y} \sum_{k=1}^N \text{trace}(\Gamma_k)$$

subject to:

$$\begin{bmatrix} \Gamma_k & (W_1 Y)^* \\ W_1 Y & P_{W_2}^* P_{c,W_2} + P_{c,W_2}^* P_{W_2} - P_{c,W_2}^* P_{c,W_2} \end{bmatrix} (j\omega_k) > 0$$

$$[Y^* Y_c + Y_c^* Y - Y_c^* Y_c] (j\omega_k) > 0, \quad \forall \omega_k \in \Omega_N$$

2.7.2 Controller Order

The choice of the order of the controller is sometimes not obvious. Often, a good initial guess of the order can be made from observing the dynamics of the plant (e.g. the number of resonance modes and couplings). Otherwise, a relatively low order of 4 to 6 is a good starting guess for most systems. After a controller has been designed, the order can be adjusted by evaluating the performance of the controller. If the desired specifications have been achieved, the order can often be lowered while retaining the result. On the other hand, if the final controller lies far from the desired specifications, sometimes increasing the order can improve the performance.

It has also been observed that for plants with complex dynamics, sometimes significantly better performance is achieved by using high controller orders (40 or higher). The order of the final controller can then often be reduced significantly through classical reduction techniques for easier implementation.

2.7.3 Initial controller

The stability conditions presented in Theorems 2 and 3 require a stabilizing initial controller K_c with a condition on the order of $\det(Y_c)$, and the same poles on the stability boundary as the desired final controller. For a stable plant, a stabilizing initial controller that satisfies condition on the order of $\det(Y_c)$ can always be found by choosing:

$$K_c = X_c Y_c^{-1}, \quad X_c = \epsilon z^p I, \quad Y_c = z^p I \quad (2.63)$$

with ϵ being a sufficiently small number. If the final controller contains fixed terms F_y with poles on the stability boundary, they must also be included in the initial controller. For example, to design a controller with integral action in all outputs, $Y_c = z^p(z-1)I$ can be considered.

When choosing an initial controller whose performance is far from the desired specifications, it may occur that either the optimization problem has no feasible solution, or that the solver runs into numerical problems which lead to an infeasible solution. These

problems can often be resolved by two approaches:

Re-initialization: A possibility to find an initial with a systematic approach for stable plants is by solving the following optimization problem using a nonlinear optimization solver with random initialization:

$$\begin{aligned} & \max_{X,Y} a \\ & \text{subject to:} \\ & \Re \left\{ \det(I + GXY^{-1}) \right\} \geq a \quad \forall \omega \in \Omega_N \end{aligned} \tag{2.64}$$

Any solution to the above optimization problem will be a stabilizing controller if the optimal value of a is greater than -1. The problem can be solved multiple times with different random initialization to generate a set of initial stabilizing controllers, which can be used to initialize the algorithm. It should be noted that this formulation can be overly conservative and may not always be feasible (e.g. if the plant has a double integrator).

Relaxation: We can relax or even remove some of the constraints. The relaxed optimization problem is then solved and the optimal controller is used to initialize the non-relaxed problem. As this new controller is comparatively close to the final solution, the issue is often solved with this approach.

It should be mentioned that the design of fixed-structure controllers in a model-based setting also requires an initialization with a stabilizing controller, which is usually integrated in the workflow. The methods based on non-smooth optimization like *hinfstruct* in Matlab [19] or the public-domain toolbox HIFOO [22] use a set of randomly chosen stabilizing controllers for initialization and take the best result. This set is constructed by solving a non-convex optimization problem that minimizes the maximum eigenvalue of a closed-loop transfer function. Other model-based approaches use an initial stabilizing controller to convert the bilinear matrix inequalities to LMIs and solve it with convex optimization algorithms. Therefore, from this point of view, this approach is subject to the same restrictions as the state-of-the-art approaches for fixed-structure controller design in a model-based setting.

2.7.4 Numerical Issues

All LMI constraints formulated so far are strict positive definiteness constraints. This is important especially for the stability constraints, where strict positive definiteness is crucial. However, numerical optimization generally does not support strict inequalities, meaning the stability constraints may be violated due to numerical precision. This issue

can be mitigated by defining a non-strict constraint with a sufficient margin:

$$\begin{bmatrix} P^*P_c + P_c^*P - P_c^*P_c & (W_1Y)^* \\ W_1Y & I \end{bmatrix} \geq \epsilon I \quad (2.65)$$

where $\epsilon \in \mathbb{R}$ is a small number. Practical experience has shown that often values around 10^{-10} can serve to improve numerical robustness without affecting the achieved performance.

To improve the numerical robustness of the optimization it is also crucial that the constraints are scaled properly. Especially for MIMO systems, all in- and outputs of the plant should be normalized properly in order to obtain good results. If necessary, individual LMI constraints can be scaled to increase the precision. Assume the following general convex-concave inequality:

$$\frac{1}{\eta}(F^*\gamma^{-1}F - P^*P) < 0 \quad (2.66)$$

where $\eta \in \mathbb{R}$ is a scaling factor. This can be transformed to either of the following convexified constraints:

$$\begin{bmatrix} \frac{1}{\eta}(P^*P_c + P_c^*P - P_c^*P_c) & \frac{1}{\sqrt{\eta}}F^* \\ \frac{1}{\sqrt{\eta}}F & \gamma I \end{bmatrix} > 0 \quad (2.67)$$

$$\begin{bmatrix} \frac{1}{\eta}(P^*P_c + P_c^*P - P_c^*P_c) & F^* \\ F & \eta\gamma I \end{bmatrix} > 0 \quad (2.68)$$

2.7.5 Iterative algorithm

Once a stabilizing initial controller is found, it is used to formulate the optimization problem. Any LMI solver can be used to solve the optimization problem and calculate a suboptimal controller K around the initial controller K_c . As we are only solving an inner convex approximation of the original optimization problem, K depends heavily on the initial controller K_c and the performance criterion can be quite far from the optimal value. The solution is to use an iterative approach that solves the optimization problem multiple times, using the final controller K of the previous step as the new initial controller K_c . This choice always guarantees closed-loop stability (assuming the initial choice of K_c is stabilizing). Since the objective function is non-negative and non-increasing, the iteration converges to a local optimal solution of the original non-convex problem [56]. The iterative process can be stopped once the change in the performance criterion is sufficiently small.

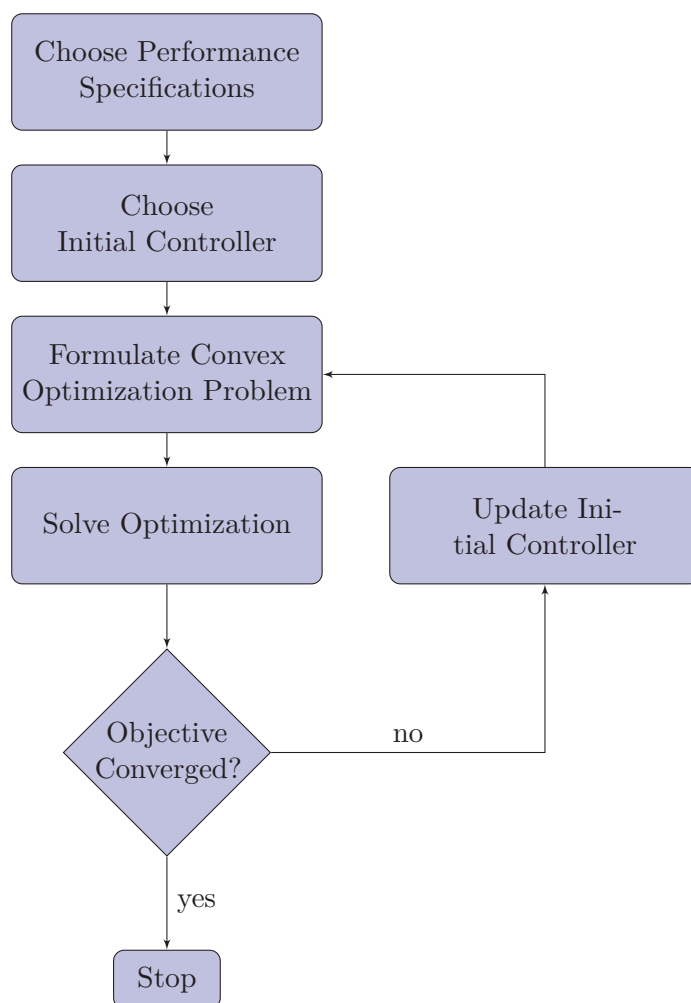


Figure 2.3 – The main steps of the control design method.

2.8 Simulation Examples

In this section, several simulation examples demonstrate the applicability of the method to general problems, and the obtained performance is compared with several state-of-the-art methods.

2.8.1 Compleib Examples

As an example, the mixed sensitivity problem for low-order continuous-time controllers is considered. 10 plants are drawn from the Compleib library [57]. For comparison, the achieved performance is compared with the results obtained using *hinfstruct* and HIFOO.

The objective is to solve the mixed sensitivity problem by minimizing the infinity-norm of (2.20), where $W_2 = I$ and $W_1 = (a_k s + 10)/(a_k s + 1)$ with a_k being chosen based on the bandwidth of the plant. Then, the optimization problem in (2.62) is formed with $N = 100$ logarithmically spaced frequency points in the interval $[0.01, 500]$ rad/s, where 500 is much larger than the bandwidth of all plants. A second-order controller $K(s) = X(s)Y(s)^{-1}$ is chosen as follows:

$$X(s) = X_2 s^2 + X_1 s + X_0 \quad , \quad Y(s) = I s^2 + Y_1 s + Y_0$$

where Y_i is a diagonal matrix in order to obtain a low-order controller. To have a fair comparison, the same method as in HIFOO is used to find a stabilizing initial controller. The method uses a non-convex approach to minimize the maximum of the spectral abscissa of the closed-loop plant, and yields a stabilizing static output feedback controller K_{SOF} . In order to satisfy Condition 3 of Theorem 2, the order of Y_c is increased without changing the initial controller :

$$X_c(s) = (s + 1)^2 K_{\text{SOF}} \quad , \quad Y_c(s) = (s + 1)^2 I \tag{2.69}$$

The names of the chosen plants in Compleib, the design parameters and the obtained norms are shown in Table 2.1. For comparison, the mixed sensitivity problems are also solved for a second-order state-space controller using HIFOO and *hinfstruct* with 10 random starts. It can be seen that the data-driven method generally achieves about the same or a lower norm. The superior results can be attributed to the fact that the controller structure is of matrix polynomial form, which has more parameters than a state-space controller of the same order due to the denominator not being equal for all entries.

The solver time of one iteration step depends almost linearly on the number of points used for the frequency gridding. It is also interesting to note that the controller order has a minimal impact on the solver time, making the algorithm well-suited for the design of higher-order controllers. The number of iterations until convergence mostly depends

Chapter 2. Fixed-Structure Control Design using Frequency-Domain Data

Table 2.1 – Comparison of optimal mixed sensitivity norms for 10 plants from Compleib

Plant Name	a_k	data-driven	<i>hinfstruct</i>	HIFOO
AC1	10	1.90	2.30	2.38
HE1	1	1.37	1.36	1.36
HE2	10	3.08	3.36	3.55
REA2	1	3.00	2.96	2.96
DIS1	1	7.27	7.31	7.34
TG1	0.1	9.54	8.89	9.75
AGS	1	2.14	2.16	2.16
BDT2	1	9.93	9.93	9.94
MFP	1	6.08	7.23	7.17
IH	1	4.83	10.01	28.73

on the choice of the initial controller and a solution is generally reached in less than 25 iterations.

2.8.2 Hard-disk Drive

This example is drawn from Matlab’s Robust Control Toolbox and treats the control design for a 9th-order model of a head-disk assembly in a hard-disk drive. In the Matlab example, *hinfstruct* is used to design a robust controller such that a desired open-loop response is achieved while satisfying a certain performance measure. We will show that an equivalent controller of the same order can be designed using the method presented in this paper.

The bode magnitude plot of the plant is shown in Fig. 2.4. The desired open-loop transfer function is given by:

$$L_d(s) = \frac{s + 10^6}{1000s + 1000} \quad (2.70)$$

Additionally, a constraint on the closed-loop transfer function is introduced to increase the robustness and performance: $\|W_1 T\|_\infty \leq 1$ and $W_1 = 1$. To stay in line with the data-driven aspect, we choose to design a discrete-time controller with the same order as the continuous-time controller given in the Matlab example:

$$K(z) = \frac{X_2 z^2 + X_1 z + X_0}{(z - 1)(z + Y_0)} \quad (2.71)$$

Since the plant is stable, an initial controller is easily found by setting X_0, X_2, Y_0 to zero and choosing a small enough value for X_1 . This results in the following initial controller:

$$K_c(z) = \frac{10^{-6} z}{z^2 - z} \quad (2.72)$$

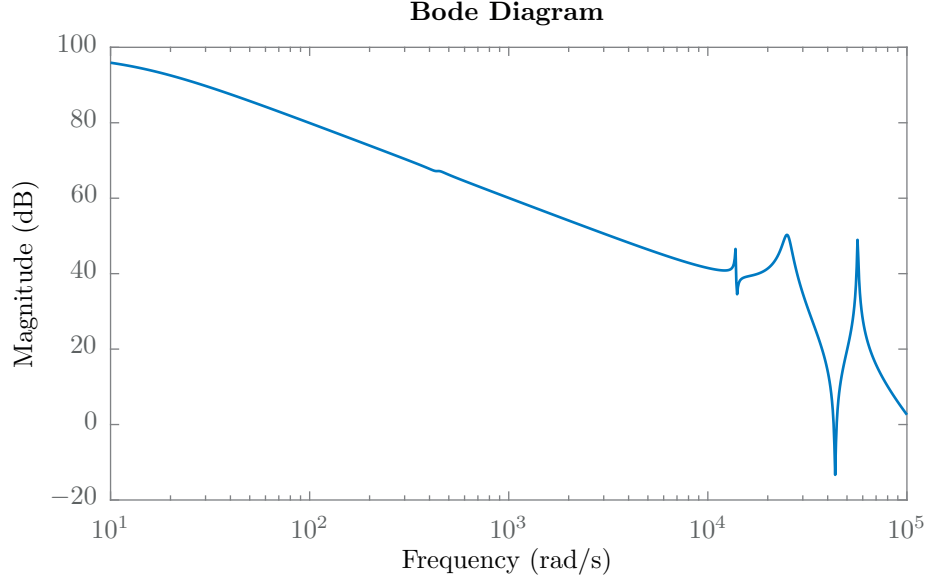


Figure 2.4 – Bode magnitude plot of the plant used in the hard-disk drive example.

Note how the pole on the unit circle introduced by the integrator is also included in the initial controller.

While with *hinfsstruct* the loop-shaping can only be formulated in the H_∞ sense, the H_2 -norm would arguably be better suited for this type of objective. We therefore choose to formulate the loop-shaping problem in the H_2 sense by minimizing $\|L - L_d\|_2$, which will lead to a better performance as shown below.

The semi-infinite formulation is sampled using 1000 logarithmically spaced frequency points in the interval $\Omega_N = [10, 5 \times 10^4\pi]$ (the upper limit being equal to the Nyquist frequency). The semi-definite problem is as follows:

$$\begin{aligned}
 & \min \sum_{k=1}^N \text{trace}[\Gamma_k] \\
 & \text{subject to:} \\
 & \begin{bmatrix} Y^*Y_c + Y_c^*Y - Y_c^*Y_c & (GX - L_dY)^* \\ GX - L_dY & \Gamma_k \end{bmatrix} (j\omega_k) > 0 \\
 & \begin{bmatrix} P^*P_c + P_c^*P - P_c^*P_c & (W_1GX)^* \\ W_1GX & I \end{bmatrix} (j\omega_k) > 0 \\
 & k = 1, \dots, N
 \end{aligned} \tag{2.73}$$

The algorithm converges within 10 iterations to a final, stabilizing controller that satisfies

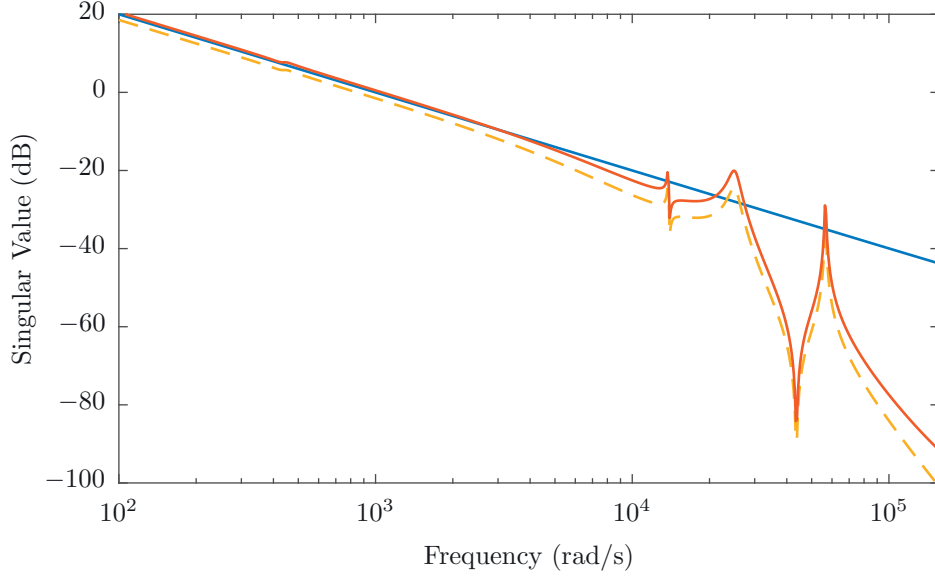


Figure 2.5 – Comparison of the open-loop transfer functions. In blue is the desired open-loop function L_d , in red the obtained open-loop function L with the proposed method, and in dashed yellow the obtained L with the *hinfstruct* controller.

the closed-loop constraint and has the following parameters:

$$K(z) = 10^{-4} \frac{2.287z^2 - 3.15z + 0.8631}{(z - 1)(z - 0.8598)} \quad (2.74)$$

Fig. 2.5 shows a comparison of the desired open-loop transfer function and the results produced by our method as well as the controller calculated in the Matlab example using *hinfstruct*. It can be seen that the result is very similar to the result generated by *hinfstruct*, with our result being closer to the desired transfer function at lower frequencies. This is especially noticeable when comparing the obtained 2-norm of the objective function, with our solution achieving a value that is around 30 times smaller. The controller obtained by our method is also already formulated in discrete-time, and no additional controller discretization step is necessary.

2.8.3 Multivariable System

This example demonstrates that the method is able to obtain near-optimal performance for low-order controllers, and shows that the convex approximation of the problem is not restrictive in practice. The mixed sensitivity problem of a 3×3 MIMO continuous-time plant model is considered. The globally optimal solution to this problem with a full-order controller can be obtained via Matlab using *mixsyn*. The plant is taken from the first

example in [43] and has the following transfer function:

$$G(s) = \begin{bmatrix} \frac{1}{s+1} & \frac{0.2}{s+3} & \frac{0.3}{s+0.5} \\ \frac{0.1}{s+2} & \frac{1}{s+1} & \frac{1}{s+1} \\ \frac{0.1}{s+0.5} & \frac{0.5}{s+2} & \frac{1}{s+1} \end{bmatrix} \quad (2.75)$$

The objective is to solve the mixed sensitivity problem by minimizing the following norm:

$$\min_{X,Y} \left\| \begin{bmatrix} W_1 S \\ W_2 K S \end{bmatrix} \right\|_{\infty} \quad (2.76)$$

where the weighting transfer functions are also taken from [43]:

$$W_1 = \frac{s+3}{3s+0.3} I, \quad W_2 = \frac{10s+2}{s+40} I \quad (2.77)$$

In this example we design a continuous-time controller to show that the developed frequency-domain LMIs in this paper can be used in the same way to design continuous-time controllers. The controller transfer function matrix is defined as $K(s) = X(s)Y^{-1}(s)$:

$$X(s) = X_p s^p + \dots + X_1 s + X_0 \quad (2.78)$$

$$Y(s) = I s^p + \dots + Y_1 s + Y_0 \quad (2.79)$$

where p is the controller order and $X_i, Y_i \in \mathbb{R}^{3 \times 3}$ are full matrices. The optimization problem is sampled using $N = 1000$ logarithmically spaced frequency points in the interval $\Omega_N = [10^{-2}, 10^2]$, resulting in the following optimization problem :

$$\begin{aligned} & \min_{X,Y} \gamma \\ & \text{subject to:} \\ & \begin{bmatrix} P^* P_c + P_c^* P - P_c^* P_c & (W_1 Y)^* & (W_2 X)^* \\ W_1 Y & \gamma I & 0 \\ W_2 X & 0 & \gamma I \end{bmatrix} (j\omega_k) > 0 \\ & [Y^* Y_c + Y_c^* Y - Y_c^* Y_c] (j\omega_k) > 0 \\ & k = 1, \dots, N \end{aligned} \quad (2.80)$$

Since the plant is stable, an initial controller can be found by setting the poles of the controller to -1 and choosing a low enough gain: $Y_c = (s+1)^p I$, $X_c = I$.

The problem is formulated for controller orders p from 1 to 5, implemented in Matlab using Yalmip [58], and solved with Mosek [59]. The algorithm converges quickly within 3 to 6 iterations. The value of the obtained norm is shown in Fig. 2.6. The number of design parameters is equal to $(2p+1) \times 9$. The figure also shows the globally optimal

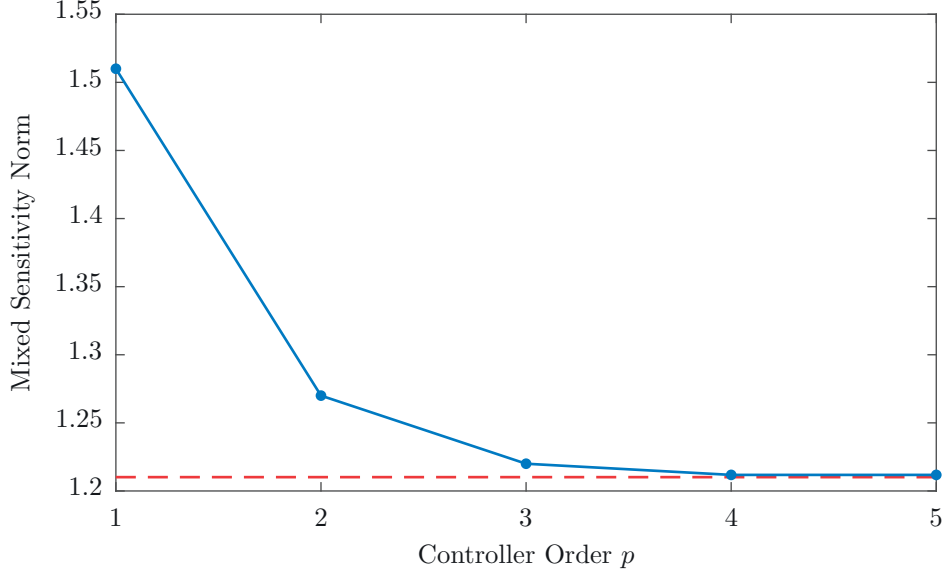


Figure 2.6 – Plot of the achieved mixed sensitivity norm for different controller orders p . The dashed red line shows the globally optimal value obtained by *mixsyn*.

norm for a full-order state-space controller with 289 design parameters obtained through *mixsyn*. It can be seen that already for $p = 3$ a good value is achieved with the following controller parameters:

$$\begin{aligned}
 X(s) = & \begin{bmatrix} 0.0794 & 0.0041 & -0.0032 \\ 0.0091 & 0.1076 & -0.0421 \\ 0.0131 & 0.031 & 0.0986 \end{bmatrix} s^3 + \begin{bmatrix} 4.5304 & -0.6974 & -0.8464 \\ -0.5345 & 3.2929 & -2.3889 \\ -0.3737 & -0.1412 & 3.421 \end{bmatrix} s^2 \\
 & + \begin{bmatrix} 9.0896 & -3.4091 & -2.6272 \\ 2.2293 & 4.0883 & -3.1235 \\ -3.0827 & -0.3391 & 3.4927 \end{bmatrix} s + \begin{bmatrix} 2.0218 & -1.0874 & -1.6883 \\ 2.4056 & 1.7292 & -0.6611 \\ -1.0974 & -0.1376 & 1.8895 \end{bmatrix} \\
 Y(s) = & \begin{bmatrix} 1 & 0 & 0 \\ 0 & 1 & 0 \\ 0 & 0 & 1 \end{bmatrix} s^3 + \begin{bmatrix} 5.1556 & -1.1562 & -0.5595 \\ -0.5993 & 1.9965 & -0.6899 \\ -0.9489 & -0.6155 & 2.2864 \end{bmatrix} s^2 \\
 & + \begin{bmatrix} 2.444 & -1.2479 & -0.7046 \\ 0.729 & 1.427 & 0.0589 \\ -0.9949 & -0.5552 & 1.1323 \end{bmatrix} s + \begin{bmatrix} 0.1514 & -0.1487 & -0.1067 \\ 0.2084 & 0.1941 & 0.1491 \\ -0.0116 & -0.0029 & 0.1791 \end{bmatrix}
 \end{aligned} \tag{2.81}$$

For $p = 5$, with only 99 design parameters the global optimum is achieved. This example shows that the proposed method is able to reach the global optimum value of the mixed

sensitivity norm for a general MIMO transfer function while having a significantly lower number of design parameters than classical state-space methods.

2.9 Conclusion

In this chapter, a frequency-domain control design method for fixed-structure controllers was presented that exhibits several key advantages as compared to traditional fixed-structure approaches. By only requiring the frequency response of the plant for the design, the complexity of the algorithm is independent of the order of the model, and is well suited for data-driven design. Not being limited to the LFT form, the method enables a broad range of H_∞ and H_2 performance constraints on any open- and closed-loop sensitivity. The full parametrization of the designed controllers greatly simplifies the choice of an appropriate controller structure, and being able to directly design in discrete-time allows to skip the intricate controller discretization step.

The rest of this thesis presents various applications of the control design methods on interesting and relevant examples. In Chapters 4 and 5 the method is applied to tackle complex challenges in the field of power systems. Further, in Appendices A and B the data-driven aspect is put into focus as the control design method is applied to two electromechanical setups that greatly benefit from data-driven design.

2.A Stability Proof - Continuous-Time

The continuous-time proof is almost analogous to the discrete-time case, with a subtle difference in Eq. 2.52 due to the different contours, which results in a slight change in the 3rd condition between Theorems 2 and 3.

Theorem 3 *Given a strictly proper plant model G , an initial stabilizing controller $K_c = X_c Y_c^{-1}$ with $\det(Y_c) \neq 0, \forall \omega \in \Omega$, and feasible solutions X and Y to the following LMI,*

$$\underbrace{(Y + GX)^*}_{P} \underbrace{(Y_c + GX_c)}_{P_c} + (Y_c + GX_c)^* (Y + GX) > 0 \quad (2.82)$$

for all $\omega \in \Omega$, then the controller $K = XY^{-1}$ stabilizes the closed-loop system if

1. $\det(Y) \neq 0, \forall \omega \in \Omega$.
2. *The initial controller K_c and the final controller K share the same poles on the stability boundary, i.e. $\det(Y) = \det(Y_c) = 0, \forall \omega \in B_y$.*
3. $\lim_{s \rightarrow \infty} \det(Y Y_c^{-1}) = \text{constant}$, i.e. *the order of $\det(Y)$ is less than or equal to the*

order of $\det(Y_c)$.

Remark: Note that the condition in (2.82) is always met when a convexified H_∞ or H_2 control problem has a feasible solution because $P^*P_c + P_c^*P > 0$ is included in the constraints.

Proof: The proof is based on the Nyquist stability criterion and the properties of the winding number. The winding number of the determinant of $P^*(z)P_c(z)$ is given by:

$$\begin{aligned} \text{wno}\{\det(P^*P_c)\} &= \text{wno}\{\det(P^*)\} + \text{wno}\{\det(P_c)\} \\ &= -\text{wno}\{\det(I + GK)\det(Y)\} + \text{wno}\{\det(I + GK_c)\det(Y_c)\} \\ &= -\text{wno}\{\det(I + GK)\} - \text{wno}\{\det(YY_c^{-1})\} + \text{wno}\{\det(I + GK_c)\} \end{aligned} \quad (2.83)$$

Note that the phase variation of $\det(P^*P_c)$ for the small detour in the Nyquist contour is zero, if Condition 2 of the theorem is satisfied. In fact, for each small detour, the Nyquist plot of $\det(I + GK)$ and $\det(I + GK_c)$ will have the same phase variation because K and K_c share the same poles on the imaginary axis. Because of the strictly properness of G and Condition 3 of the theorem, the winding number of $\det(P^*P_c)$ needs to be evaluated only on Ω instead of the complete Nyquist contour (and is constant on the infinite radius semi-circle).

Furthermore, the condition in (2.82) implies that $P^*(e^{j\omega})P_c(e^{j\omega})$ is a non-Hermitian positive definite matrix in the sense that :

$$\Re\{x^*P^*(e^{j\omega})P_c(e^{j\omega})x\} > 0 \quad \forall x \neq 0 \in \mathbb{C}^n \quad (2.84)$$

and $\forall \omega \in \Omega$. This, in turn, means that all eigenvalues of $P^*(e^{j\omega})P_c(e^{j\omega})$, denoted $\lambda_i(\omega)$ for $i = 1, \dots, n$, have positive real parts at all frequencies [52]:

$$\Re\{\lambda_i(\omega)\} > 0 \quad \forall \omega \in \Omega, i = 1, \dots, n \quad (2.85)$$

Therefore, $\lambda_i(\omega)$ will not pass through the origin and not encircle it (i.e. its winding number is zero). As a result, since the determinant of a matrix is the product of its eigenvalues, we have:

$$\text{wno}\{\det(P^*P_c)\} = \text{wno}\left\{\prod_{i=1}^n \lambda_i\right\} = \sum_{i=1}^n \text{wno}\{\lambda_i\} = 0$$

Since K_c is a stabilizing controller, based on the Nyquist theorem $\text{wno}\{\det(I + GK_c)\} = N_G + N_{K_c}$. Furthermore, obviously $\text{wno}\{\det(Y)\} = N_K$ and $\text{wno}\{\det(Y_c)\} = N_{K_c}$. Now

using (2.83), we obtain:

$$\begin{aligned} \text{wno}\{\det(I + GK)\} &= \text{wno}\{\det(I + GK_c)\} - \text{wno}\{\det(Y)\} + \text{wno}\{\det(Y_c)\} \\ &= N_G + N_K \end{aligned} \quad (2.86)$$

which shows that Condition 1 of the Nyquist theorem is met.

We can also see from (2.85) that

$$\det(P^* P_c) = \prod_{i=1}^n \lambda_i(\omega) \neq 0 \quad \forall \omega \in \Omega \quad (2.87)$$

Therefore, $\det(P) = \det(I + GK) \det(Y) \neq 0$ and the Nyquist plot of $\det(I + GK)$ does not pass through the origin and Condition 2 of the Nyquist theorem is also satisfied. ■

Remark 1: A necessary and sufficient condition for $\det(Y) \neq 0$ is $Y^* Y > 0$. Since this constraint is concave, it can be linearized to obtain the following sufficient LMI:

$$Y^* Y_c + Y_c^* Y - Y_c^* Y_c > 0 \quad (2.88)$$

This constraint can be added to the optimization problem in (2.29) in order to guarantee the closed-loop stability for the mixed sensitivity problem. For the loop-shaping problems in (2.39) and in (2.43), this condition is already included in the formulation.

3 Frequency-Domain Modeling of Power Grids

3.1 Introduction

In this chapter, a comprehensive frequency-domain approach towards the modeling of voltage and current dynamics as well as power flow dynamics is presented. The models also offer a straightforward way to combine white-, grey- and black-box models in a single framework, which enables a (partially) data-driven approach that is very appealing in power systems, where the grid parameters are often unknown.

3.1.1 State of the Art

The classical approach towards the modeling of electromagnetic and electromechanic transients in a power grid is through so-called small-signal models [60]. A small-signal model is typically a linear state-space model that describes the dynamics of the lines and generation units under small disturbances. While historically only applied to high-voltage transmission grids, the significant increase in distributed generation on the medium- and low-voltage level makes it necessary to develop suitable models for these types of grids as well. Furthermore, distributed generation units such as photovoltaics are interfaced to the grid through voltage source inverters, which introduce their own distinct dynamics that did not have to be considered before.

Various state-space modeling approaches for low-voltage grids with multiple VSI-interfaced generation units have been proposed in the literature [61–64]. However, the resulting state-space models are of very high order even for moderately-sized grids, which makes control design challenging. Model order reduction techniques have been applied to obtain simpler formulations [65–67], but choosing appropriate reduction techniques while guaranteeing that the reduced model represents the important dynamics is not obvious.

Several issues related to state-space models can be avoided by using frequency-domain models instead. In [68] a frequency-domain modeling approach for current and voltage

dynamics of a single VSIs with time delays is proposed. Similar approaches are used for stability analysis in a grid with multiple VSIs in [69, 70]. The frequency-domain approach has also been applied towards the modeling of power flow transient dynamics [71] using the concept of dynamic phasors. The model is only slightly more complex than a static power flow model, but offers the same accuracy as a small-signal model while also incorporating the generator dynamics. However, while having been used to model line dynamics and for stability analysis [72–74], this type of model has never been presented in a complete form that allows for any number of inverters, synchronous generators and loads.

3.2 Phasor Notation

Consider a balanced, three-phase quantity $\mathbf{e}(t)$:

$$\mathbf{e}(t) = \sqrt{2}e(t) \begin{bmatrix} \cos(\bar{\omega}t + \theta(t)) \\ \cos(\bar{\omega}t + \theta(t) - 2\pi/3) \\ \cos(\bar{\omega}t + \theta(t) + 2\pi/3) \end{bmatrix} \quad (3.1)$$

with $e(t)$ being the signal amplitude, $\theta(t)$ being the phase angle in rad, and $\bar{\omega}$ being the nominal grid frequency in rad/s.

The dynamic or time-varying phasor representation of $\mathbf{e}(t)$ in the rotating dq-frame is [71]:

$$\begin{aligned} \underline{e}(t) &= e_d(t) + je_q(t) = e(t) \cos(\theta(t)) + je(t) \sin(\theta(t)) \\ &= [1 \ j \ 0]B(t)\mathbf{e}(t) = \mathcal{P}(\mathbf{e}(t)) \end{aligned} \quad (3.2)$$

where $B(t)$ is the power-invariant Park transformation matrix:

$$B(t) = \sqrt{\frac{2}{3}} \begin{bmatrix} \cos(\bar{\omega}t) & \cos(\bar{\omega}t - \frac{2\pi}{3}) & \cos(\bar{\omega}t + \frac{2\pi}{3}) \\ -\sin(\bar{\omega}t) & -\sin(\bar{\omega}t - \frac{2\pi}{3}) & -\sin(\bar{\omega}t + \frac{2\pi}{3}) \\ \frac{1}{\sqrt{2}} & \frac{1}{\sqrt{2}} & \frac{1}{\sqrt{2}} \end{bmatrix} \quad (3.3)$$

Similarly, the dynamic phasors of the first and second time derivative of $\mathbf{e}(t)$ are [71]:

$$\mathcal{P}\left(\frac{d}{dt}\mathbf{e}(t)\right) = j\bar{\omega}\underline{e}(t) + \frac{d}{dt}\underline{e}(t) \quad (3.4)$$

$$\mathcal{P}\left(\frac{d^2}{dt^2}\mathbf{e}(t)\right) = -\bar{\omega}^2\underline{e}(t) + 2j\bar{\omega}\frac{d}{dt}\underline{e}(t) + \frac{d^2}{dt^2}\underline{e}(t) \quad (3.5)$$

The models derived in the following sections rely on this phasor notation.

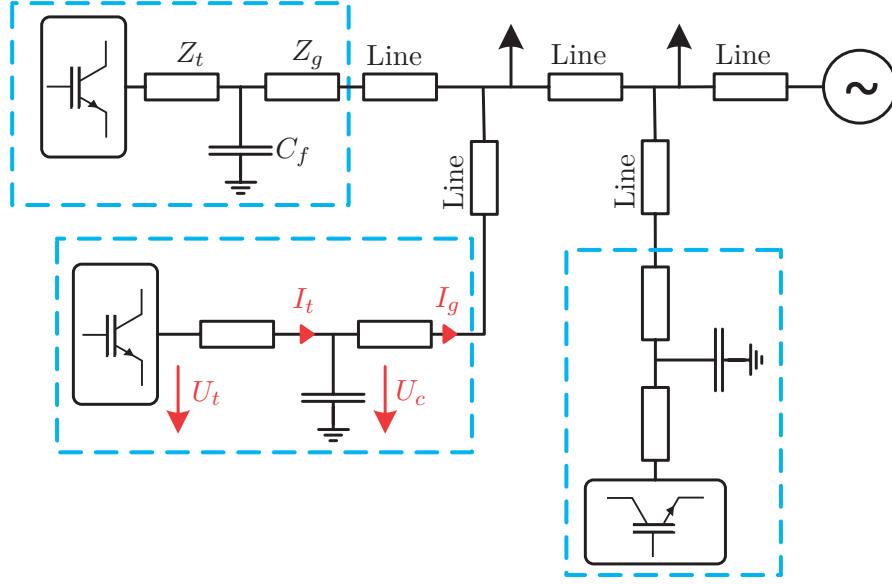


Figure 3.1 – One-line diagram of a distribution grid with multiple VSIs and constant current loads.

3.3 Frequency-Domain Model of Voltage and Current Dynamics

In this section, a transfer function model is constructed that accurately describes the voltage and current dynamics in a grid with any number of inverters with LCL output filters, including the electromagnetic dynamics of the lines, output filters and coupling effects. The model is formulated directly in the dq-frame, which is also where the control laws are typically formulated. The presented frequency-domain formulation offers the same modeling accuracy as a state-space small-signal model, but does not contain internal state variables, which greatly reduces the model complexity. For this model, all three-phase signals are assumed to be balanced.

3.3.1 Line Current Dynamics

Figure 3.1 shows the single-line diagram of a typical three-phase distribution grid with multiple power electronic devices. For low- and medium-voltage grids, lines can be modeled as simple R-L elements, and the shunt capacitance can be neglected. Furthermore, the line resistance and inductance matrices are assumed to be positive definite and circulant [75], which means symmetrical components can be used to study the system.

Then, we can write the current flowing from bus i to bus j in the following representation:

$$(R_{ij} + j\omega L_{ij})\underline{i}_{ij}(t) + L_{ij} \frac{d}{dt} \underline{i}_{ij}(t) = \underline{u}_i(t) - \underline{u}_j(t) \quad (3.6)$$

Chapter 3. Frequency-Domain Modeling of Power Grids

where $\underline{u}_i(t), \underline{i}_{ij}(t)$ are the complex bus voltage and line current, $\bar{\omega}$ is the nominal grid frequency and R_{ij}, L_{ij} are scalars describing the positive sequence line resistance and inductance. This can be written in the following Laplace transfer function form:

$$\underline{I}_{ij}(s) = \frac{sL_{ij} + R_{ij} - j\bar{\omega}L_{ij}}{(sL_{ij} + R_{ij})^2 + (\bar{\omega}L_{ij})^2}(\underline{U}_i(s) - \underline{U}_j(s)) \quad (3.7)$$

The arguments (t) and (s) are generally omitted for the rest of this section. Now, we can formulate the matrix transfer function of the line current in the dq-frame:

$$\begin{bmatrix} I_{ij,d} \\ I_{ij,q} \end{bmatrix} = \frac{1}{D} \begin{bmatrix} sL_{ij} + R_{ij} & \bar{\omega}L_{ij} \\ -\bar{\omega}L_{ij} & sL_{ij} + R_{ij} \end{bmatrix} \begin{bmatrix} U_{i,d} - U_{j,d} \\ U_{i,q} - U_{j,q} \end{bmatrix} \\ D = (sL_{ij} + R_{ij})^2 + (\bar{\omega}L_{ij})^2 \quad (3.8)$$

Now assume each bus in the grid is either connected to a VSI with LCL output filter, or to a constant current load. Furthermore, assume the grid-side impedances Z_g of the LCL filters are lumped with the lines, and define the voltage at a VSI bus to be the capacitor voltage U_c . We then define the following vectors:

$$I_{g,dq}^{\mathcal{I}} = [I_{g,d}^1, I_{g,q}^1, \dots, I_{g,d}^n, I_{g,q}^n]^T \quad (3.9)$$

$$U_{c,dq}^{\mathcal{I}} = [U_{c,d}^1, U_{c,q}^1, \dots, U_{c,d}^n, U_{c,q}^n]^T \quad (3.10)$$

where n is the number of VSIs in the grid, $I_{g,dq}^{\mathcal{I}}$ is a vector with all VSI grid currents (named I_g in Fig. 3.1) and $U_{c,dq}^{\mathcal{I}}$ is a vector with all capacitor voltages of the LCL output filters (named U_c in Fig. 3.1).

Using Kirchhoff's Current Law and the transfer function from Equation 3.8, we can then formulate the current-balance equations for every bus:

$$\underbrace{\begin{bmatrix} Y_1(s) & Y_2(s) \\ Y_3(s) & Y_4(s) \end{bmatrix}}_{Y(s)} \begin{bmatrix} U_{c,dq}^{\mathcal{I}} \\ U_{dq}^{\mathcal{N}} \end{bmatrix} = \begin{bmatrix} I_{g,dq}^{\mathcal{I}} \\ I_{dq}^{\mathcal{L}} \end{bmatrix} \quad (3.11)$$

where $U_{dq}^{\mathcal{N}}$ is a vector with the voltages at the load buses, and $I_{dq}^{\mathcal{L}}$ is a vector with the load currents. $Y_{1,\dots,4}$ are transfer function matrices according to Eq. 3.8. It is interesting to note that the frequency response evaluated at $\bar{\omega}$ of the matrix transfer function $Y(j\bar{\omega})$ is equal to the nodal admittance matrix of the grid. However, to study stability it is necessary to consider the dynamic transfer function formulation $Y(s)$.

The load bus voltages can then be eliminated to achieve the following formulation of the

3.3. Frequency-Domain Model of Voltage and Current Dynamics

VSI grid currents, with the load currents entering as a disturbance:

$$\begin{bmatrix} I_{g,dq}^{\mathcal{I}} \end{bmatrix} = \underbrace{(Y_1 - Y_2 Y_4^{-1} Y_3)}_{Y_{\mathcal{I}}} \begin{bmatrix} U_{c,dq}^{\mathcal{I}} \end{bmatrix} + \underbrace{Y_2 Y_4^{-1}}_{Y_d} \begin{bmatrix} I_{dq}^{\mathcal{L}} \end{bmatrix} \quad (3.12)$$

This transfer function models the complete dynamics of the output currents of all VSIs in the grid depending on the capacitor voltages, with the load currents entering as a disturbance. In [76], it is shown that Y_4 is always invertible as long as all buses are connected and all lines have non-zero resistance.

3.3.2 LCL Filter Dynamics

To create a complete model, the dynamics of the LCL output filters need to be taken into account. Based on Fig. 3.1, we can formulate the following equations for each individual LCL filter:

$$\mathbf{i}_t = C_f \frac{d}{dt} \mathbf{u}_c + \mathbf{i}_g \quad (3.13)$$

$$\mathbf{u}_t - \mathbf{u}_c = R_t \mathbf{i}_t + L_t \frac{d}{dt} \mathbf{i}_t \quad (3.14)$$

where $Z_t = R_t + j\bar{\omega}L_t$. $\mathbf{u}_t, \mathbf{u}_c$ are the terminal voltage and capacitor voltage, and $\mathbf{i}_t, \mathbf{i}_c$ are the inverter-side and grid-side current of the VSI. By inserting Eq. 3.13 in Eq. 3.14 we get:

$$\mathbf{u}_t - \mathbf{u}_c = R_t (C_f \frac{d}{dt} \mathbf{u}_c + \mathbf{i}_g) + L_t (C_f \frac{d^2}{dt^2} \mathbf{u}_c + \frac{d}{dt} \mathbf{i}_g) \quad (3.15)$$

Translating this equation to the dq-frame and writing it in the Laplace transfer function form yields:

$$\begin{aligned} & \left(L_t C_f (-\bar{\omega}^2 + 2j\bar{\omega}s + s^2) + R_t C_f (j\bar{\omega} + s) + 1 \right) \underline{U}_c \\ &= \underline{U}_t - (R_t + j\bar{\omega}L_t + s) \underline{I}_g \end{aligned} \quad (3.16)$$

from which we arrive at the following transfer function matrix:

$$\begin{aligned} \begin{bmatrix} U_{c,dq} \end{bmatrix} &= \begin{bmatrix} Y_{5,1} & -Y_{5,2} \\ Y_{5,2} & Y_{5,1} \end{bmatrix}^{-1} Y_6 \begin{bmatrix} U_{t,dq} \\ I_{g,dq} \end{bmatrix} \\ Y_{5,1} &= s^2 L_t C_f + s R_t C_f + (1 - L_t C_f \bar{\omega}^2) \\ Y_{5,2} &= s^2 L_t C_f \bar{\omega} + R_t C_f \bar{\omega} \\ Y_6 &= \begin{bmatrix} 1 & 0 & -(sL_t + R_t) & L_t \bar{\omega} \\ 0 & 1 & -L_t \bar{\omega} & -(sL_t + R_t) \end{bmatrix} \end{aligned} \quad (3.17)$$

Furthermore, from Eq. 3.8 we can straightforwardly write:

$$\begin{aligned} \begin{bmatrix} I_{t,dq} \end{bmatrix} &= \begin{bmatrix} Y_7 & -Y_7 \end{bmatrix} \begin{bmatrix} U_{t,dq} \\ U_{c,dq} \end{bmatrix} \\ Y_7 &= \frac{1}{(sL_t + R_t)^2 + (\bar{\omega}L_t)^2} \begin{bmatrix} sL_t + R_t & \bar{\omega}L_t \\ -\bar{\omega}L_t & sL_t + R_t \end{bmatrix} \end{aligned} \quad (3.18)$$

The transfer functions Y_1 to Y_7 describe the output filter dynamics for a single inverter. From this, the output filter dynamics for all VSIs in the grid can be written in the following compact matrix form:

$$\begin{bmatrix} U_{c,dq}^{\mathcal{I}} \end{bmatrix} = G^{U_t \rightarrow U_c} \begin{bmatrix} U_{t,dq}^{\mathcal{I}} \end{bmatrix} + G^{I_g \rightarrow U_c} \begin{bmatrix} I_{g,dq}^{\mathcal{I}} \end{bmatrix} \quad (3.19)$$

$$\begin{bmatrix} I_{t,dq}^{\mathcal{I}} \end{bmatrix} = G^{U_t \rightarrow I_t} \begin{bmatrix} U_{t,dq}^{\mathcal{I}} \end{bmatrix} + G^{U_c \rightarrow I_t} \begin{bmatrix} U_{c,dq}^{\mathcal{I}} \end{bmatrix} \quad (3.20)$$

where $G^{U_t \rightarrow U_c}, G^{I_g \rightarrow U_c}$ are matrix transfer functions constructed using Eq. 3.17, and $G^{U_t \rightarrow I_t}, G^{U_c \rightarrow I_t}$ are matrix transfer functions based on Eq. 3.18.

3.3.3 Complete Transfer Function Model

With all the building blocks in place, a transfer function model of the complete system can now be constructed. A block diagram of the model with the individual subsystems is shown in Fig. 3.2, where K in this example would be a current controller that is to be designed. From this block diagram, it is straightforward to compute the matrix transfer function from the modulation voltages and load currents to the inverter currents:

$$\begin{aligned} \begin{bmatrix} I_{t,dq}^{\mathcal{I}} \end{bmatrix} &= G_{\text{complete}} \begin{bmatrix} U_{t,dq}^{\mathcal{I}} \end{bmatrix} + G_d \begin{bmatrix} I_{dq}^{\mathcal{L}} \end{bmatrix} \\ G_{\text{complete}} &= G^{U_t \rightarrow I_t} + G^{U_c \rightarrow I_t} (\mathbf{I} - G^{I_g \rightarrow U_c} Y_{\mathcal{I}})^{-1} G^{U_t \rightarrow U_c} \\ G_d &= G^{U_c \rightarrow I_t} G^{I_g \rightarrow U_c} (\mathbf{I} - G^{I_g \rightarrow U_c} Y_{\mathcal{I}})^{-1} Y_d \end{aligned} \quad (3.21)$$

This frequency-domain model describes well the electromagnetic dynamics of the complete grid, including the dynamics of the LCL output filters and coupling effects. It is also straightforward to extend in order to include different types of output filters, to consider the inverter dynamics in more details, or to reshape in order to design a voltage controller. Another possible extension would be the inclusion of more complex load models.

3.4. Frequency-Domain Power Flow Model (Dynamic Phasor Model)

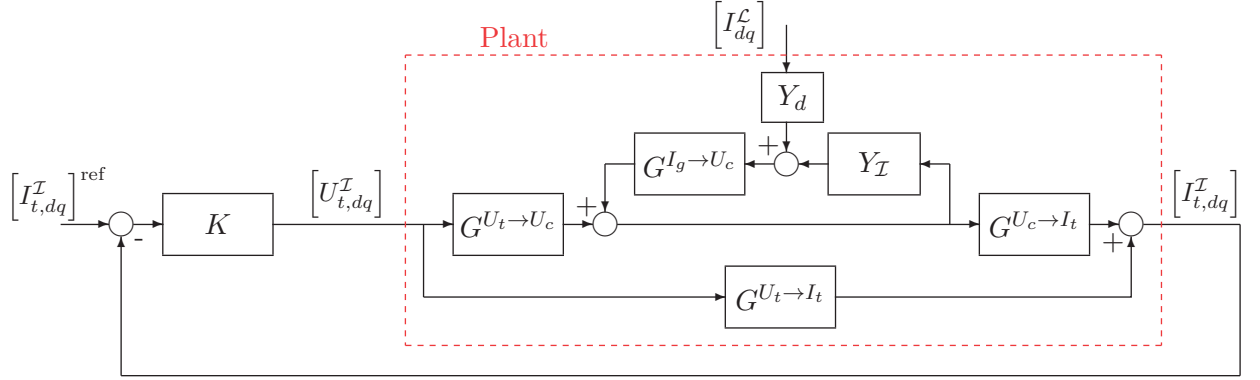


Figure 3.2 – Block diagram of the complete closed-loop model.

3.4 Frequency-Domain Power Flow Model (Dynamic Phasor Model)

In this section a linear power flow model based on dynamic phasors is presented. The dynamic phasor model is a frequency-domain model that is able to accurately represent the electromagnetic and electromechanic transient dynamics of the lines as well as various generation units, loads and other grid components. It has only a slightly increased complexity as compared to a static model, but provides the same accuracy as a small-signal model. The main advantage of this modeling approach is that the active and reactive power flow dynamics in the grid can be fully described by the voltage phase angle (or frequency) and the voltage magnitude at the generator buses. As the dynamic phasor model is a frequency-domain model, there are no internal state variables, which allows the use of detailed and high-order generator and load models without increasing its complexity.

3.4.1 Dynamic Power Flow Equations

As derived in (3.7), the current flowing from bus i to bus j can be written as:

$$\underline{I}_{ij}(s) = \frac{sL_{ij} + R_{ij} - j\bar{\omega}L_{ij}}{(sL_{ij} + R_{ij})^2 + (\bar{\omega}L_{ij})^2} (\underline{U}_i(s) - \underline{U}_j(s)) \quad (3.22)$$

The power flowing out of bus i into the line ij is defined as:

$$S_{ij} = P_{ij} + jQ_{ij} = 3\underline{I}_{ij}^* \underline{U}_i = \frac{sL_{ij} + R_{ij} + j\bar{\omega}L_{ij}}{(sL_{ij} + R_{ij})^2 + (\bar{\omega}L_{ij})^2} (\underline{U}_i^* - \underline{U}_j^*) \underline{U}_i \quad (3.23)$$

Chapter 3. Frequency-Domain Modeling of Power Grids

where P_{ij}, Q_{ij} are the active and reactive power flowing from bus i to bus j , and $(\cdot)^*$ denotes the complex conjugate. The dynamic phasor of the voltage can be written as:

$$\underline{U}_i(s) = U_i(s)e^{j\theta_i(s)} \quad (3.24)$$

where U_i is the voltage magnitude and θ_i is the phase angle at bus i . Then, the dynamic power flow becomes:

$$P_{ij} + jQ_{ij} = 3 \frac{sL_{ij} + R_{ij} + j\bar{\omega}L_{ij}}{(sL_{ij} + R_{ij})^2 + (\bar{\omega}L_{ij})^2} (U_i^2 - U_i U_j e^{j(\theta_i - \theta_j)}) \quad (3.25)$$

which can be expanded to:

$$\begin{aligned} P_{ij} + jQ_{ij} = & \frac{3}{(sL_{ij} + R_{ij})^2 + (\bar{\omega}L_{ij})^2} \\ & \left[(sL_{ij} + R_{ij})U_i^2 - (sL_{ij} + R_{ij})U_i U_j \cos(\theta_i - \theta_j) + \bar{\omega}L_{ij}U_i U_j \sin(\theta_i - \theta_j) \right. \\ & \left. + j \left(\bar{\omega}L_{ij}U_i^2 - (sL_{ij} + R_{ij})U_i U_j \sin(\theta_i - \theta_j) - \bar{\omega}L_{ij}U_i U_j \cos(\theta_i - \theta_j) \right) \right] \end{aligned} \quad (3.26)$$

Now, these equations can be linearized around $\theta_i = \theta_j = 0$ and $U_i = U_j = \bar{U}$ where \bar{U} is the nominal phase-to-ground RMS voltage. This leads to the linear dynamic power flow equations:

$$\begin{aligned} P_{ij}(s) = & \underbrace{3 \frac{\bar{\omega}L_{ij}}{(L_{ij}s + R_{ij})^2 + (\bar{\omega}L_{ij})^2} \bar{U}^2 \frac{1}{s}}_{G_{ij}^{\omega \rightarrow P}(s)} (\omega_i(s) - \omega_j(s)) \\ & + \underbrace{3 \frac{L_{ij}s + R_{ij}}{(L_{ij}s + R_{ij})^2 + (\bar{\omega}L_{ij})^2} \bar{U}}_{G_{ij}^{U \rightarrow P}(s)} (U_i(s) - U_j(s)) \end{aligned} \quad (3.27)$$

$$\begin{aligned} Q_{ij}(s) = & \underbrace{-3 \frac{L_{ij}s + R_{ij}}{(L_{ij}s + R_{ij})^2 + (\bar{\omega}L_{ij})^2} \bar{U}^2 \frac{1}{s}}_{G_{ij}^{\omega \rightarrow Q}(s)} (\omega_i(s) - \omega_j(s)) \\ & + \underbrace{3 \frac{\bar{\omega}L_{ij}}{(L_{ij}s + R_{ij})^2 + (\bar{\omega}L_{ij})^2} \bar{U}}_{G_{ij}^{U \rightarrow Q}(s)} (U_i(s) - U_j(s)) \end{aligned} \quad (3.28)$$

where the phase angle at a bus has been substituted with the frequency: $\theta_i = \frac{1}{s}\omega_i$. With the traditional assumption of lines being mostly inductive, and therefore R/X being small, it is interesting to note that the steady-state formulation of the dynamic power

3.4. Frequency-Domain Power Flow Model (Dynamic Phasor Model)

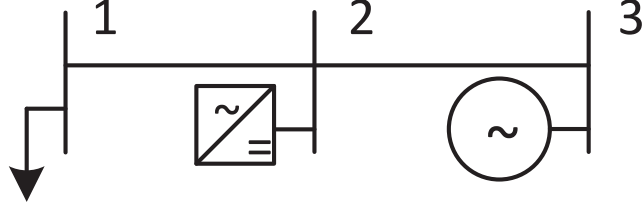


Figure 3.3 – Small example grid with one load, one VSI and one SG.

flow reduces to the well-known static power flow equations:

$$P_{ij} = 3 \frac{X_{ij}}{R_{ij}^2 + (\bar{\omega} L_{ij})^2} \bar{U}^2 \frac{1}{s} (\omega_i - \omega_j) \quad (3.29)$$

$$Q_{ij} = 3 \frac{X_{ij}}{R_{ij}^2 + (\bar{\omega} L_{ij})^2} \bar{U} (U_i - U_j) \quad (3.30)$$

Of course, this simplification usually does not hold in low- and medium-voltage grids, where the R/X -ratio of the lines is generally close to or larger than 1.

3.4.2 Line Power Flows Model

Now, the transfer function from the generator bus frequencies and voltages to the active and reactive line power flows can be developed. We assume that every bus in the grid is connected to either a VSI, an SG or a load. Without loss of generality, any zero-injection buses are assumed to be connected to virtual loads that do not draw any power, and are lumped with the load buses. Then, dividing the buses into VSI buses, SG buses and load buses, we can write:

$$\begin{bmatrix} P_{\mathcal{I}} \\ Q_{\mathcal{I}} \\ P_{\mathcal{S}} \\ Q_{\mathcal{S}} \\ P_{\mathcal{L}} \\ Q_{\mathcal{L}} \end{bmatrix} = \begin{bmatrix} G_1 & G_2 & G_3 \\ G_4 & G_5 & G_6 \\ G_7 & G_8 & G_9 \end{bmatrix} \begin{bmatrix} \omega_{\mathcal{I}} \\ U_{\mathcal{I}} \\ \omega_{\mathcal{S}} \\ U_{\mathcal{S}} \\ \omega_{\mathcal{L}} \\ U_{\mathcal{L}} \end{bmatrix} \quad (3.31)$$

Let p be the number of VSI buses, q the number of SG buses and l the number of load buses in the grid. $P_{\mathcal{I}}, Q_{\mathcal{I}} \in \mathbb{R}^{p \times 1}$, $P_{\mathcal{S}}, Q_{\mathcal{S}} \in \mathbb{R}^{q \times 1}$, $P_{\mathcal{L}}, Q_{\mathcal{L}} \in \mathbb{R}^{l \times 1}$ are vectors with the active and reactive power injected by the VSIs, sync. generators and loads (load powers usually have a negative sign). The matrix transfer functions $G_i (i = 1, \dots, 9)$ are constructed using the power flow transfer functions in equation (3.27), where G_1 is of dimension $2p \times 2p$, G_2 of $2p \times 2q$, G_3 of $2p \times 2l$, with the dimensions of $G_{4,\dots,9}$ accordingly.

As example, consider a radial grid with 3 buses shown in Fig. 3.3, with a load connected

at bus 1, a VSI at bus 2 and an SG at bus 3. Then, $G_{1,2,3}$ would be:

$$G_1 = \begin{bmatrix} G_{21}^{\omega \rightarrow P} + G_{23}^{\omega \rightarrow P} & G_{21}^{U \rightarrow P} + G_{23}^{U \rightarrow P} \\ G_{21}^{\omega \rightarrow Q} + G_{23}^{\omega \rightarrow Q} & G_{21}^{U \rightarrow Q} + G_{23}^{U \rightarrow Q} \end{bmatrix} \quad (3.32)$$

$$G_2 = \begin{bmatrix} -G_{23}^{\omega \rightarrow P} & -G_{23}^{U \rightarrow P} \\ -G_{23}^{\omega \rightarrow Q} & -G_{23}^{U \rightarrow Q} \end{bmatrix} \quad (3.33)$$

$$G_3 = \begin{bmatrix} -G_{21}^{\omega \rightarrow P} & -G_{21}^{U \rightarrow P} \\ -G_{21}^{\omega \rightarrow Q} & -G_{21}^{U \rightarrow Q} \end{bmatrix} \quad (3.34)$$

The frequency and voltage at the load buses is generally unknown. Assuming constant power loads, the dynamics are reformulated such that the power drawn by the loads enters the system as a disturbance. Thus, the power injected by the generators can be written as a function of the generator bus phasors, with the load power acting as a disturbance:

$$\begin{bmatrix} P_I \\ Q_I \\ P_S \\ Q_S \end{bmatrix} = G_{\text{grid}} \begin{bmatrix} \omega_I \\ U_I \\ \omega_S \\ U_S \end{bmatrix} + G_d \begin{bmatrix} P_L \\ Q_L \end{bmatrix} \quad (3.35)$$

with

$$G_{\text{grid}} = \begin{bmatrix} G_1 - G_3 G_9^{-1} G_7 & G_2 - G_3 G_9^{-1} G_8 \\ G_4 - G_6 G_9^{-1} G_7 & G_5 - G_6 G_9^{-1} G_8 \end{bmatrix} \quad (3.36)$$

$$G_d = \begin{bmatrix} G_3 G_9^{-1} \\ G_6 G_9^{-1} \end{bmatrix} \quad (3.37)$$

This formulation assumes G_9 to be invertible, which is always the case if all buses in the grid are connected.

It is important to note that G_{grid} describes the dynamics of the lines, but does not contain the dynamics of the generation units and sensors. The next sections will show how these dynamics can be incorporated in the model.

3.4.3 Voltage Source Inverter Model

A specific advantage of the presented formulation is that grey- and black-box models of VSIs can directly be incorporated, and no knowledge of the internal control loops and dynamics is required. Assuming a VSI operating in Frequency-Voltage mode, a simple way to model the closed-loop dynamics is as an ideal voltage source with the following

3.4. Frequency-Domain Power Flow Model (Dynamic Phasor Model)

first-order dynamics:

$$\begin{bmatrix} \omega_{\mathcal{I}} \\ U_{\mathcal{I}} \end{bmatrix} = G_{\mathcal{I}} \begin{bmatrix} \bar{\omega}_{\mathcal{I}} \\ \bar{U}_{\mathcal{I}} \end{bmatrix} \quad (3.38)$$

$$G_{\mathcal{I}} = \text{diag}\left(\frac{1}{\tau_{\omega}s + 1}, \frac{1}{\tau_U s + 1}\right) \quad (3.39)$$

where $\bar{\omega}_{\mathcal{I}}, \bar{U}_{\mathcal{I}}$ are the desired VSI bus frequency and voltage magnitude, and τ_{ω}, τ_U are the closed-loop time constants of the frequency and voltage control loop. If the VSI is outfitted with an L -type output filter, a simple way to model it is to lump it with the parameters of the lines connected to the VSI.

The dynamics of the VSI transfer function can easily be extended to include more complicated output filters, resonance modes and time delays. If the internal control loops and parameters are known, the model can also be augmented to include an exact formulation of the complete VSI dynamics. Furthermore, if experimental data is available it is also possible to directly use the measured frequency-response.

3.4.4 Synchronous Generator Model

The main frequency dynamics of a synchronous generator are well represented through the swing equation:

$$\frac{2H}{\bar{\omega}} \dot{\omega}_S = \frac{1}{S_S} (G_{\text{PM}} \bar{P}_{S,m} - P_S) \quad (3.40)$$

where $\bar{P}_{S,m}, P_S$ are the desired mechanical input power and the electrical output power of the generator, S_S is the rated apparent power of the generator, H is the inertia constant and G_{PM} contains the dynamics of the prime mover. The resulting transfer function is:

$$\omega_S = \begin{bmatrix} G_{S,m} & G_{S,e} \end{bmatrix} \begin{bmatrix} \bar{P}_{S,m} \\ P_S \end{bmatrix} \quad (3.41)$$

$$G_{S,m} = G_{\text{PM}} \frac{\bar{\omega}}{2HS_S}, \quad G_{S,e} = -\frac{\bar{\omega}}{2HS_S}$$

The voltage at an SG bus is commonly tightly regulated by the internal AVR (Automatic Voltage Regulator) of the machine. The closed-loop response of the AVR can again be formulated as a transfer function:

$$U_S = G_{S,U} \bar{U}_S \quad (3.42)$$

where \bar{U}_S is the desired SG bus voltage magnitude. A simple way to model the prime

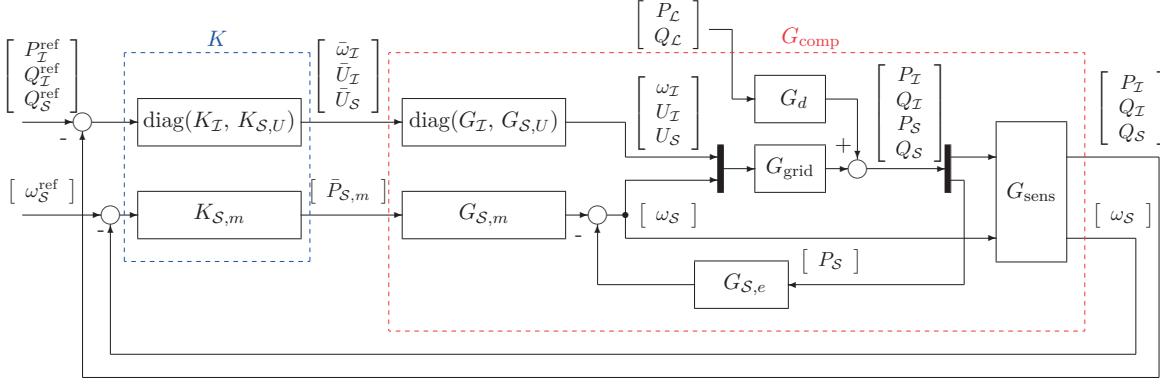


Figure 3.4 – Block diagram of the full dynamic phasor model.

mover and AVR dynamics is through the following first-order dynamics:

$$G_{PM} = \frac{1}{\tau_m s + 1}, \quad G_{S,U} = \frac{1}{\tau_U s + 1} \quad (3.43)$$

where τ_m, τ_U are the time constants of the prime mover and AVR. While this generator model is relatively simple, the transfer functions in (3.40) and (3.42) can easily be extended to include more complex dynamics and coupling effects thanks to the modular structure of the dynamic phasor model.

3.4.5 Complete Dynamic Phasor Model

Combining the transfer function models established in the previous sections, it is now possible to construct the complete dynamic phasor model of a grid with any number of VSIs, SGs and constant power loads. The closed-loop block diagram of the complete model is shown in Fig. 3.4. In a classical formulation, the controller transfer function matrices $K_I, K_{S,U}, K_{S,m}$ would be the droop controllers. G_{sens} is a $(2p + 2q) \times (2p + 2q)$ diagonal transfer function matrix containing the sensor dynamics.

In order to achieve a form suitable for control design, the plant is rewritten as single transfer function matrix G_{comp} (as indicated in Fig. 3.4), with the inputs and outputs corresponding to the classical droop control scheme. The inputs of G_{comp} are the setpoints of the VSI frequency, the VSI and SG voltage magnitude and the SG mechanical input power. The outputs are the VSI active power, the VSI and SG reactive power and the SG frequency. To achieve this, first G_{grid} from (3.35) is partitioned and reordered such

3.4. Frequency-Domain Power Flow Model (Dynamic Phasor Model)

that the following transfer functions are obtained:

$$\begin{bmatrix} P_{\mathcal{I}} \\ Q_{\mathcal{I}} \\ P_{\mathcal{S}} \\ Q_{\mathcal{S}} \end{bmatrix} = \begin{bmatrix} G_{\text{grid}}^{u \rightarrow P_{\mathcal{I}}} & G_{\text{grid}}^{\omega_{\mathcal{S}} \rightarrow P_{\mathcal{I}}} \\ G_{\text{grid}}^{u \rightarrow Q_{\mathcal{I}}} & G_{\text{grid}}^{\omega_{\mathcal{S}} \rightarrow Q_{\mathcal{I}}} \\ G_{\text{grid}}^{u \rightarrow P_{\mathcal{S}}} & G_{\text{grid}}^{\omega_{\mathcal{S}} \rightarrow P_{\mathcal{S}}} \\ G_{\text{grid}}^{u \rightarrow Q_{\mathcal{S}}} & G_{\text{grid}}^{\omega_{\mathcal{S}} \rightarrow Q_{\mathcal{S}}} \end{bmatrix} \begin{bmatrix} u \\ \omega_{\mathcal{S}} \end{bmatrix} \quad (3.44)$$

$$u = \begin{bmatrix} \omega_{\mathcal{I}} & U_{\mathcal{I}} & U_{\mathcal{S}} \end{bmatrix}^T$$

Now, the single block transfer function of the plant can be obtained as follows:

$$\begin{bmatrix} P_{\mathcal{I}} \\ Q_{\mathcal{I}} \\ Q_{\mathcal{S}} \\ \omega_{\mathcal{S}} \end{bmatrix} = G_{\text{comp}} \begin{bmatrix} \bar{u} \\ \bar{P}_{\mathcal{S},m} \end{bmatrix}, \quad \bar{u} = \begin{bmatrix} \bar{\omega}_{\mathcal{I}} & \bar{U}_{\mathcal{I}} & \bar{U}_{\mathcal{S}} \end{bmatrix}^T$$

$$G_{\text{comp}} = G_{\text{sens}} \begin{bmatrix} G_{11} & G_{12} \\ G_{21} & G_{22} \\ G_{31} & G_{32} \\ G_{41} & G_{42} \end{bmatrix} \begin{bmatrix} G_{\mathcal{I}} & 0 & 0 \\ 0 & G_{\mathcal{S},U} & 0 \\ 0 & 0 & I \end{bmatrix} \quad (3.45)$$

where I is the identity matrix, and:

$$\begin{aligned} G_{11} &= (G_{\text{grid}}^{u \rightarrow P_{\mathcal{I}}} - G_{\text{grid}}^{\omega_{\mathcal{S}} \rightarrow P_{\mathcal{I}}} G_{\mathcal{S},e} G_{51}) \\ G_{12} &= G_{\text{grid}}^{\omega_{\mathcal{S}} \rightarrow P_{\mathcal{I}}} (G_{\mathcal{S},m} - G_{\mathcal{S},e} G_{52}) \\ G_{21} &= G_{\text{grid}}^{u \rightarrow Q_{\mathcal{I}}} - G_{\text{grid}}^{\omega_{\mathcal{S}} \rightarrow Q_{\mathcal{I}}} G_{\mathcal{S},e} G_{51} \\ G_{22} &= G_{\text{grid}}^{\omega_{\mathcal{S}} \rightarrow Q_{\mathcal{I}}} (G_{\mathcal{S},m} - G_{\mathcal{S},e} G_{52}) \\ G_{31} &= G_{\text{grid}}^{u \rightarrow Q_{\mathcal{S}}} - G_{\text{grid}}^{\omega_{\mathcal{S}} \rightarrow Q_{\mathcal{S}}} G_{\mathcal{S},e} G_{51} \\ G_{32} &= G_{\text{grid}}^{\omega_{\mathcal{S}} \rightarrow Q_{\mathcal{S}}} (G_{\mathcal{S},m} - G_{\mathcal{S},e} G_{52}) \\ G_{41} &= -G_{\mathcal{S},e} G_{51} \\ G_{42} &= G_{\mathcal{S},m} - G_{\mathcal{S},e} G_{52} \\ G_{51} &= (I + G_{\text{grid}}^{\omega_{\mathcal{S}} \rightarrow P_{\mathcal{S}}} G_{\mathcal{S},e})^{-1} G_{\text{grid}}^{u \rightarrow P_{\mathcal{S}}} \\ G_{52} &= (I + G_{\text{grid}}^{\omega_{\mathcal{S}} \rightarrow P_{\mathcal{S}}} G_{\mathcal{S},e})^{-1} G_{\text{grid}}^{\omega_{\mathcal{S}} \rightarrow P_{\mathcal{S}}} G_{\mathcal{S},m} \end{aligned}$$

Written in this form, the matrix transfer function G_{comp} can readily be used for small-signal stability analysis and control design.

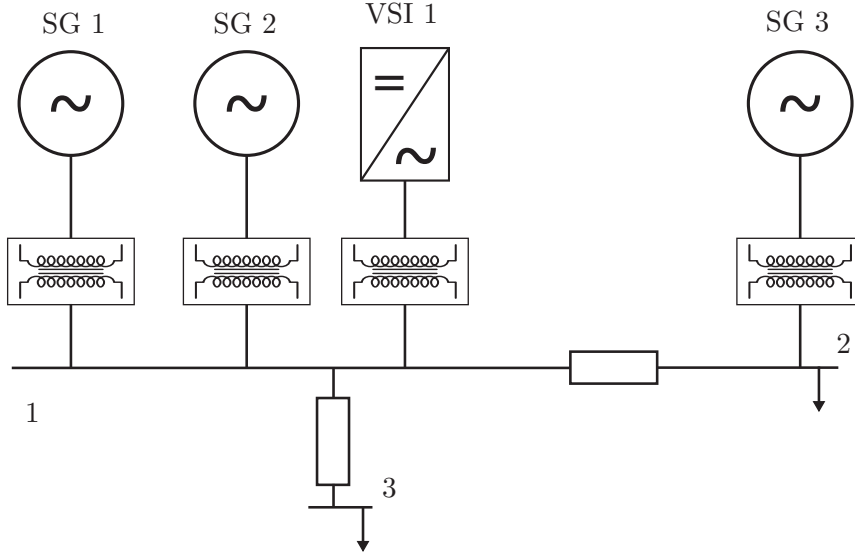
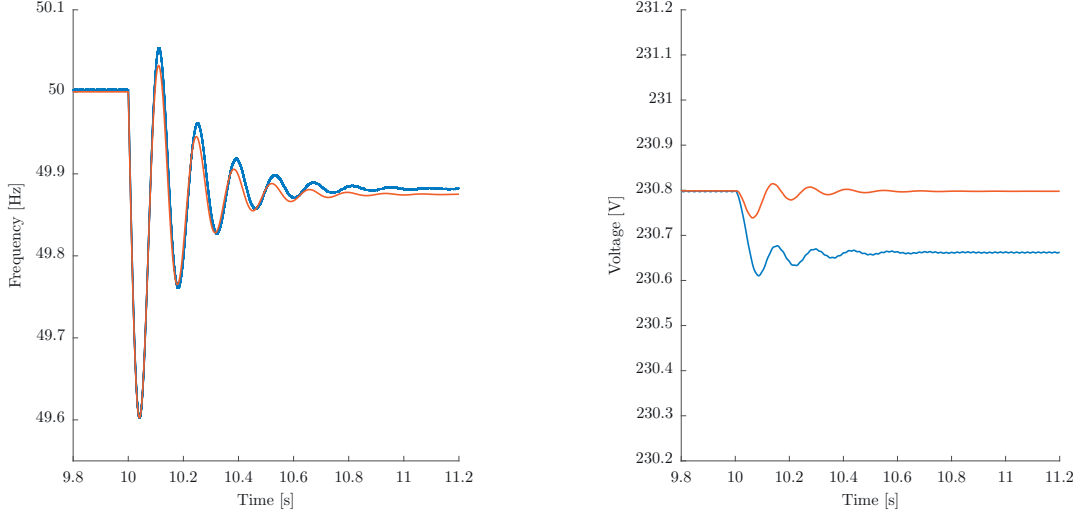


Figure 3.5 – One-line diagram of a 50 Hz/230 V islanded grid with 3 SGs and one VSI. The arrows denote constant power loads.

3.4.6 Validation of Dynamic Phasor Model

To validate the dynamic phasor model, the transient behaviour of a low-voltage islanded grid with 3 SGs, 1 VSI and 2 active power loads is evaluated (see Fig. 3.5). The VSI operates in grid-forming mode [77], where its frequency and voltage magnitude are controlled. A standard droop controller is used to provide primary frequency and voltage control, meaning the controllers $K_I, K_{S,U}, K_{S,m}$ in 3.4 are decentralized proportional controllers. The grid is implemented in Simulink using the Simpower toolbox, and the transient response of the generators to a change in the active power load at bus 3 is considered. For the nonlinear simulation, the VSI is modeled as an ideal voltage source with an L -type output filter. The SGs are modeled using the ‘Simplified Synchronous Machine’ model from the Simpower toolbox, which on the mechanical side models the swing equation, and on the electrical side consists of a voltage source behind a synchronous reactance and resistance. For the linear simulation, the model is implemented in Simulink as shown in Fig. 3.4.

In Figs. 3.6a and 3.6b the transients of the frequency and voltage magnitude of one of the SGs is shown after the active power load at bus 3 is stepped up. It can be seen that the dynamic phasor model represents the transient dynamics very well, with the frequency and magnitude of the oscillations being very similar to the nonlinear model. A steady-state error can be observed in both results, which is due to the linearization of the power flows. Similarly, in Figs. 3.7a and 3.7b the active and reactive output power of the SG is shown after a step in the active power load. Again it can be seen that the



(a) Frequency after an active power load step.

(b) Voltage after an active power load step.

Figure 3.6 – Comparison of frequency and voltage between nonlinear simulation (in blue) and linear dynamic phasor model (in red).

transient dynamics are modeled well by the dynamic phasor model ¹.

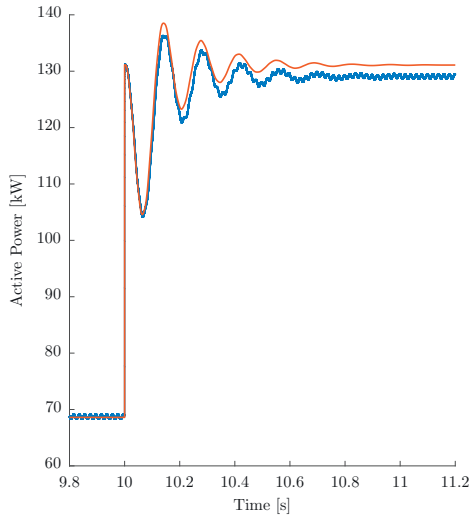
These results reinforce that the dynamic phasor model provides accurate results and is well suited for transient stability analysis and primary as well as secondary control design.

3.5 Conclusion

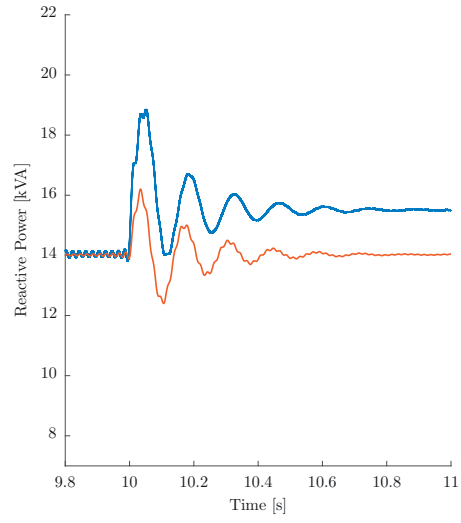
A frequency-domain modeling approach for low- and medium-voltage grids with VSI-interfaced devices as well as synchronous machines has been developed. In the first part it was shown how the voltage and current dq-frame dynamics can be formulated as a matrix transfer function model. An essential part of the model is that it also represents the dynamics of the VSI output filters and coupling effects, which play a crucial role for stability analysis and control design.

In the second part, a linear dynamic phasor model is derived that describes the dynamics of the grid frequencies and voltage magnitudes as well as active and reactive power flows. The model also includes the dynamics of VSI-interfaced generation units, synchronous machines and active power loads, which is of paramount importance when studying transient stability as well as primary and secondary control design. Simulation results show that the model is very well suited for the modeling of transient dynamics and to

¹Thanks a lot to Daniel Ryan from Monash University for providing these results!



(a) Active output power after an active power load step.



(b) Reactive output power after an active power load step.

Figure 3.7 – Comparison of power flows between nonlinear simulation (in blue) and linear dynamic phasor model (in red).

assess transient stability.

The model also forms a solid basis for the validation of data-driven models derived from measurement data, which is a very interesting and relevant approach especially in distribution grids, where the grid parameters are often unknown.

4 Current Control Design for Parallel Grid-Connected Inverters

4.1 Introduction

The scenario discussed in this chapter is motivated by a real case study [78], which was conducted to identify the source of instability problems in a rural Swiss distribution grid very similar to the one shown in Fig. 4.1. The figure depicts a typical 50 Hz/400 V distribution grid with resistive lines (R/X -ratio greater than 6), four inverter-interfaced PV generation units with LCL output filters situated close together, and a relatively long line connecting to the main grid. As is often the case in this type of grid, if power generation is high the VSI buses suffer overvoltage problems. Also, since the lines are mostly resistive, reactive power injection has almost no effect on the voltage level. To resolve the overvoltage situation, the local DSO decided to add a Line Voltage Regulator (LVR) to the grid, which is tap-changing transformer that becomes active whenever an over- or undervoltage situation is detected.

However, the LVR also significantly increases the inductance of the line and brings the R/X -ratio close to 1, which has a significant impact on the electromagnetic dynamics of the grid. In the case study, the commercial VSIs were current-controlled by a standard combination of PI controllers on the current and a feedback loop on the capacitor voltage to improve the performance. However, as can be seen in Fig. 4.2, the standard controllers were clearly not able to deal with the new grid dynamics: turning on the LVR leads to large oscillations in the current and voltage, followed by a shutdown of all PV units.

As will be discussed in this chapter, this example nicely exhibits the challenges of control design for multiple parallel VSIs in weak grids. It will be shown that the addition of the LVR strongly affects the coupling resonances introduced by the parallel configuration of the VSI output filters, which are not at all considered in classical single-inverter control design. The control design method from Chapter 2 and the frequency-domain model from Chapter 3 are then combined to propose a new paradigm for inverter control design, where the controllers for any number of VSIs can be designed in a single step while

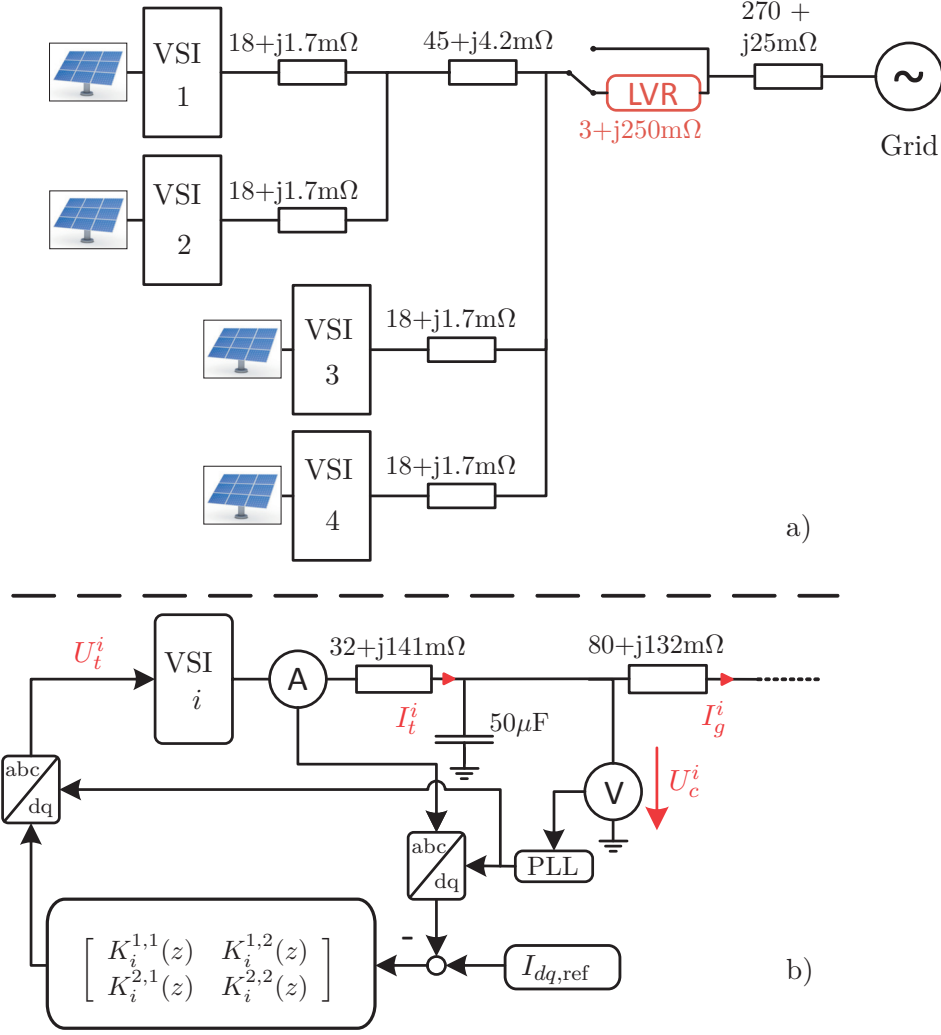


Figure 4.1 – Electrical one-line diagrams: a) a rural distribution grid with 4 VSIs and a Line Voltage Regulator (LVR), b) the output filter configuration and controller block diagram of the VSIs.

guaranteeing robust stability and performance. An additional challenge is that new VSIs are added to existing grids at a rapid pace. Controllers have to be designed for this plug-and-play installation without affecting the operation of the already installed VSIs. This plug-and-play design will also be explored in this chapter, and it will be shown that the control design method is very well suited for this task.

4.1.1 State of the Art

In recent years, the increase in distributed generation, distributed storage and drive loads has significantly increased the proportion of power electronic devices in distribution grids. These devices are commonly connected to the grid through voltage source inverters (VSIs) with passive output filters. A desirable filter structure is the LCL filter, which

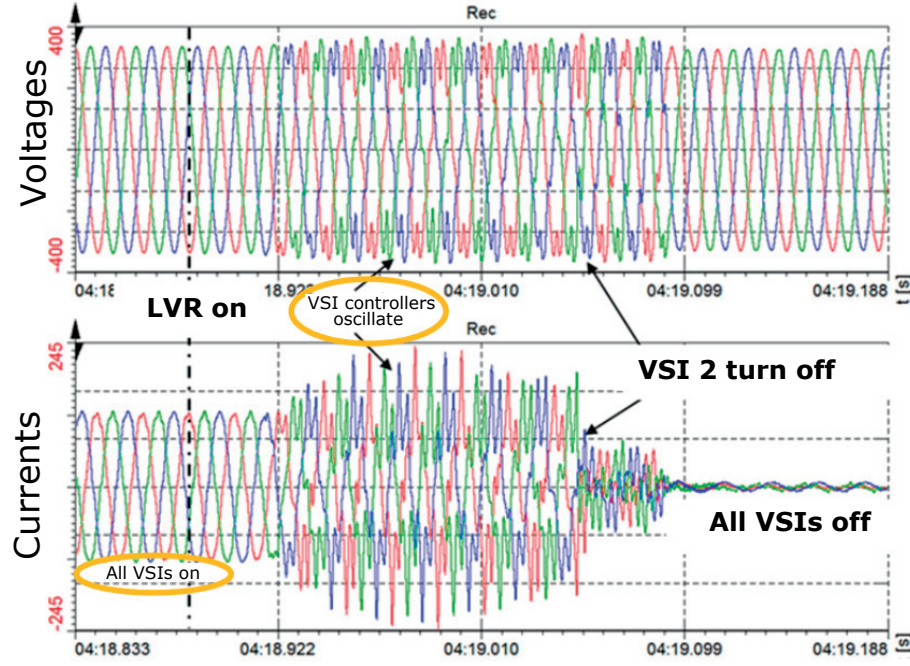


Figure 4.2 – Measurements of three-phase current and voltage at the LVR after it is switched on [78].

exhibits many advantageous features. However, the parallel operation of VSIs with LCL filters also introduces new resonance frequencies and coupling effects to the grid, which present a challenge for stability analysis and control design [69, 79–82].

For single VSIs, many active damping methods have been proposed in the literature. A common approach is to introduce active filter elements to the feedback loop, and tune the parameters based on the model of a single-inverter infinite bus system. A comprehensive review of the state-of-the-art methods is given in [83]. However, using a single-inverter model neglects all coupling dynamics in the grid, and there is no guarantee for stability or performance in a system with multiple VSIs.

In [62, 84, 85] a state-space model of the complete system is constructed, and the resonance modes are classified based on modal participation factors. A drawback of this approach is that accurate representations with multiple generation units lead to very high-order models which become difficult to analyze. Another avenue is to use impedance-based transfer function models and frequency-domain analysis methods [69, 86, 87]. These approaches break the system into interconnected component models that are easier to handle than a complete model. Various approaches for tuning the current controllers of any number of parallel PV inverters are presented in [88, 89], however the stability analysis assumes that all inverters are identical. In [90] a multivariable transfer function model for grids with multiple VSIs is developed, and it is shown that the model can be used for stability analysis through Nyquist diagrams. The modeling approach is further used in [91, 92] to derive various design rules for proportional controllers based on root

locus curves.

Common features of the methods discussed above are that controller and filter parameters are adjusted using iterative procedures, and that stability is evaluated a posteriori. A drawback of this approach is that for systems with large numbers of generation units the plant order and the number of design parameters becomes very high, which makes it difficult to tune all variables in an efficient manner. Furthermore, reaching explicit performance specifications is challenging when using manual tuning methods.

Attempts have been made to apply classical robust control design methods to the problem [93–95]. This allows to guarantee robust stability and performance, and makes it possible to design higher-order controllers that would be very challenging to tune manually. Furthermore, in [96, 97] methods are proposed to design controllers that are robust towards parametric uncertainties in the plant model. A major drawback is that these methods require a state-space model of the system, but don't scale well with the number of states. This means that even moderately sized problems become very hard to solve efficiently. This limits the applicability of the methods in practice.

A way to avoid the issues of high-order state-space models in control design is to use frequency-domain methods. In [39, 98] a multivariable PI current controller for a single grid-tied VSI is tuned using an optimization-based method and a nonparametric model. The same approach is also used in [99] to tune a higher order current controller for a VSI with an LCL output filter. However, the method only allows for linearly parametrized controllers and generally yields very conservative results for multivariable systems.

Another important aspect is plug-and-play capability, which describes the procedure to add a new VSI to an existing grid while maintaining stability and performance. Iterative tuning approaches are presented in [100–102], where the stability is evaluated a posteriori, which is impractical for controllers with multiple tuning parameters. In [103] a method is presented where the controllers of neighbouring VSIs have to be retuned as well. In [97] the addition of a new VSI is treated as an uncertainty, however the method is generally too conservative.

4.2 Control Design

In this section, it will be shown how a decentralized current controller for all four VSIs in Fig. 4.1 can be designed in a single step while guaranteeing stability and various performance specifications.

4.2.1 Grid Model

Using the method described in Section 3.3, two transfer function models for the grid shown in Fig. 4.1 without and with the LVR are constructed. For the modeling, the LVR is modeled as an R-L element using the simplified equivalent circuit transformer model, and the grid-side impedances of the filters and the impedance of the LVR are lumped with the lines. According to Eq. 3.21 this leads to the following models:

$$\begin{aligned} \begin{bmatrix} I_{t,dq}^{\mathcal{I}} \end{bmatrix} &= G_1 \begin{bmatrix} U_{t,dq}^{\mathcal{I}} \end{bmatrix} \\ \begin{bmatrix} I_{t,dq}^{\mathcal{I}} \end{bmatrix} &= G_2 \begin{bmatrix} U_{t,dq}^{\mathcal{I}} \end{bmatrix} \end{aligned} \quad (4.1)$$

where

$$I_{g,dq}^{\mathcal{I}} = \left[I_{g,d}^1, I_{g,q}^1, I_{g,d}^2, I_{g,q}^2, I_{g,d}^3, I_{g,q}^3, I_{g,d}^4, I_{g,q}^4 \right]^T \quad (4.2)$$

$$U_{t,dq}^{\mathcal{I}} = \left[U_{t,d}^1, U_{t,q}^1, U_{t,d}^2, U_{t,q}^2, U_{t,d}^3, U_{t,q}^3, U_{t,d}^4, U_{t,q}^4 \right]^T \quad (4.3)$$

and where G_1, G_2 are 10×10 matrix transfer functions from the VSI modulation voltages to the inverter currents without and with the LVR.

To visualize the effect of the LVR on the frequency response of the system, the maximum singular value plots of G_1, G_2 for both grid configurations are shown in Fig. 4.3. The singular value plot is an extension of the Bode magnitude plot for multivariable systems, and is a very useful tool for robustness analysis [104].

The expected resonance peaks of the LCL output filters can be seen around 1400 Hz. However, the model without LVR also exhibits additional resonance peaks at 1200 Hz that stem from the coupling of the LCL filters, and would not be represented in a classical single-inverter model. Furthermore, with the inclusion of the LVR the frequency of the coupling resonance decreases to 1000 Hz and now dominates the dynamic response, which further accentuates the importance of using a complete grid model.

4.2.2 Control Specifications

The controller should satisfy the following performance specifications for both grid configurations (without and with the LVR):

1. Closed-loop bandwidth of at least 500 Hz
2. Small overshoot
3. Robustness towards modeling errors
4. Good decoupling of currents in d and q axis

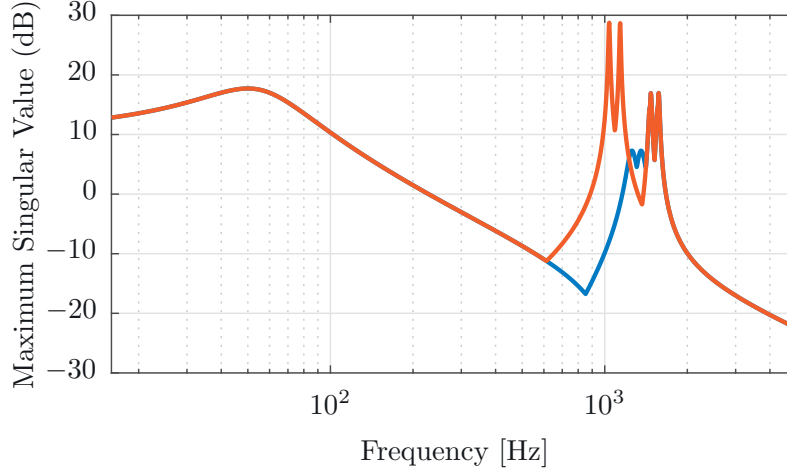


Figure 4.3 – Maximum singular value plots of the grid model. The model without the LVR is in blue, and with the LVR in red.

A good way to limit the impact of strong resonance modes on the closed-loop performance is to limit the closed-loop sensitivity transfer functions. In order to achieve a desired closed-loop bandwidth and to limit the impact of an output disturbance on the tracking error, the following norm is minimized:

$$\min_{X,Y} (\max(\|W_1 S_1\|_\infty, \|W_1 S_2\|_\infty)), \quad W_1 = \left(\frac{s \omega_{bw}}{s + \omega_{bw}} \right)^{-1} \mathbf{I} \quad (4.4)$$

$$S_1 = (I + G_1 K)^{-1}, \quad S_2 = (I + G_2 K)^{-1}$$

where $\omega_{bw} = 2\pi \cdot 500$ is the desired bandwidth and S_1, S_2 are the sensitivity transfer functions of the two plants (without and with the LVR).

Similarly, the second and third specifications are satisfied by placing constraints on the two closed-loop sensitivity functions T_1, T_2 that enforces a roll-off at frequencies above the desired bandwidth:

$$\|W_2 T_1\|_\infty < 1, \quad \|W_2 T_2\|_\infty < 1, \quad W_2 = \left(1.1 \frac{\omega_{bw}}{s + \omega_{bw}} \right)^{-1} \mathbf{I} \quad (4.5)$$

$$T_1 = G_1 K (I + G_1 K)^{-1}, \quad T_2 = G_2 K (I + G_2 K)^{-1}$$

The chosen gain of 1.1 for W_2 guarantees low overshoot and little ringing in the closed-loop response by keeping the maximum of T small.

Finally, a constraint is placed on the input sensitivities U_1, U_2 to prevent saturation and

fast oscillations in the input:

$$\begin{aligned} \|W_3 U_1\|_\infty < 1, \quad \|W_3 U_2\|_\infty < 1, \quad W_3 = (5.5B)^{-1}\mathbf{I} \\ U_1 = K(I + G_1 K)^{-1}, \quad U_2 = K(I + G_2 K)^{-1} \end{aligned} \quad (4.6)$$

where B is a second-order discrete-time Butterworth low-pass filter with a cutoff frequency of 2500 Hz. The gain of 5.5 for W_3 was tuned to guarantee that the input does not reach saturation for the maximum expected disturbance.

These constraints are combined to formulate the following robust control design problem, where $\gamma \in \mathbb{R}$ is an auxiliary scalar variable:

$$\begin{aligned} & \min_{X,Y} \gamma \\ & \text{subject to:} \\ & \|W_1 S_1\|_\infty < \gamma, \quad \|W_1 S_2\|_\infty < \gamma \\ & \|W_2 T_1\|_\infty < 1, \quad \|W_2 T_2\|_\infty < 1 \\ & \|W_3 U_1\|_\infty < 1, \quad \|W_3 U_2\|_\infty < 1 \end{aligned} \quad (4.7)$$

4.2.3 Controller Structure

A decentralized, multivariable 4th-order controller with a sampling frequency of 10 kHz is designed, where every VSI has access only to its local current measurements. The input to the controller is the current error, and the output is the modulation voltage (see Fig. 3.2). The controllers of the 4 VSIs in Fig. 4.1 can be compounded as a single block-diagonal transfer function matrix according to the multivariable plant model from Eq. 4.1:

$$\begin{aligned}
 K &= \begin{bmatrix} K_1^{1,1} & K_1^{1,2} & & & \\ K_1^{2,1} & K_1^{2,2} & & & \\ & & \ddots & & \\ & & & K_4^{1,1} & K_4^{1,2} \\ & & & K_4^{2,1} & K_4^{2,2} \end{bmatrix} = XY^{-1} \\
 X &= \begin{bmatrix} X_1^{1,1} & X_1^{1,2} & & & \\ X_1^{2,1} & X_1^{2,2} & & & \\ & & \ddots & & \\ & & & X_4^{1,1} & X_4^{1,2} \\ & & & X_4^{2,1} & X_4^{2,2} \end{bmatrix} \\
 Y &= \begin{bmatrix} Y_1^{1,1} & & & & \\ & Y_1^{2,2} & & & \\ & & \ddots & & \\ & & & Y_4^{1,1} & \\ & & & & Y_4^{2,2} \end{bmatrix} \circ (z-1)\mathbf{I} \\
 X_k^{i,j} &= X_{k,4}^{i,j}z^4 + X_{k,3}^{i,j}z^3 + X_{k,2}^{i,j}z^2 + X_{k,1}^{i,j}z + X_{k,0}^{i,j} \\
 Y_k^{i,j} &= z^4 + Y_{k,3}^{i,j}z^3 + Y_{k,2}^{i,j}z^2 + Y_{k,1}^{i,j}z + Y_{k,0}^{i,j}
 \end{aligned} \tag{4.8}$$

where X has a block-diagonal and Y has a diagonal structure. The final 2×2 controller of each individual VSI contains 28 tunable parameters, which allows for many degrees of freedom during the design, but would be very difficult to tune manually. This demonstrates well the benefits of using an optimization-based approach.

4.2.4 Convex Formulation

To solve the optimization problem formulated in Equation 4.7, a frequency grid with 300 logarithmically-spaced frequency points in the interval $\Omega_N = \{1, 10^4\pi\}$ rad/s is chosen, where the upper limit is the Nyquist frequency of the controller. Furthermore, the 6 main resonance frequencies of the plant are explicitly added to the frequency grid. As stabilizing initial controller, a decentralized integral controller with a low gain is chosen:

$$X_c = 0.01z^4\mathbf{I}, \quad Y_c = z^4(z-1)\mathbf{I} \tag{4.9}$$

Then, as described in Chapter 2, the control design problem with multimodel uncertainty

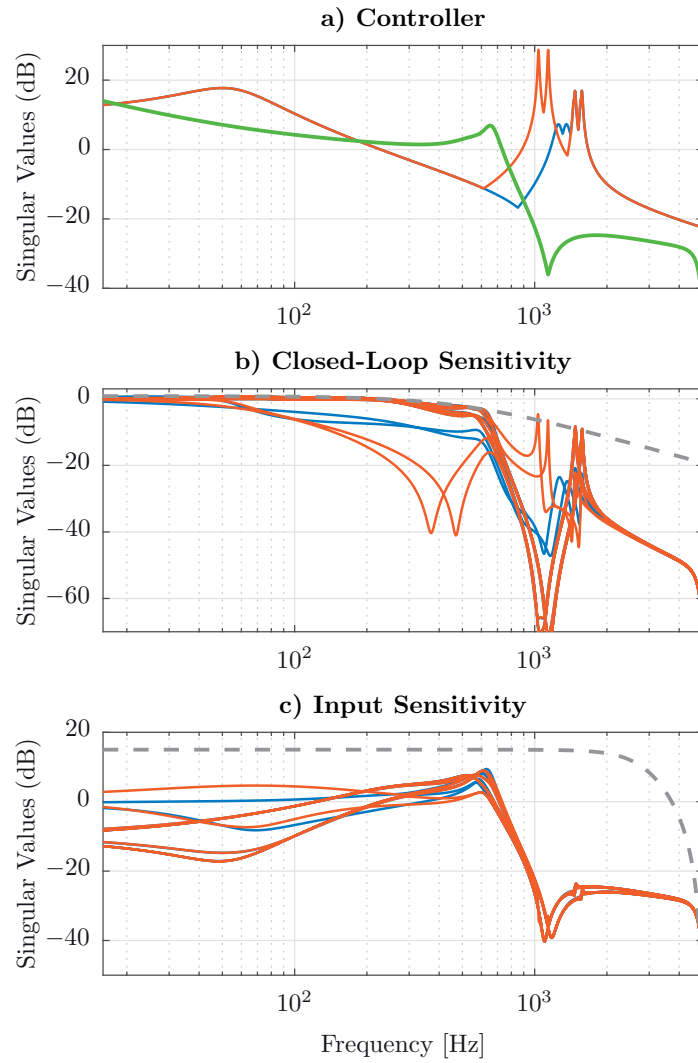


Figure 4.4 – Maximum singular values plots: a) the controller (in green) and the plant without and with the LVR (in blue and red), b) the closed-loop sensitivities and c) the input sensitivities without and with the LVR. The dashed lines indicate the constraints.

is reformulated as a convex optimization problem:

$$\begin{aligned}
 & \min_{X,Y} \gamma \\
 & \text{subject to:} \\
 & \begin{bmatrix} P_i^* P_{c_i} + P_{c_i}^* P_i - P_{c_i}^* P_{c_i} & (W_1 Y)^* \\ W_1 Y & \gamma I \end{bmatrix} (j\omega_k) > 0 \\
 & \begin{bmatrix} P_i^* P_{c_i} + P_{c_i}^* P_i - P_{c_i}^* P_{c_i} & (W_2 G_i X)^* \\ W_2 G_i X & I \end{bmatrix} (j\omega_k) > 0 \\
 & \begin{bmatrix} P_i^* P_{c_i} + P_{c_i}^* P_i - P_{c_i}^* P_{c_i} & (W_3 X)^* \\ W_3 X & I \end{bmatrix} (j\omega_k) > 0 \\
 & (Y^* Y_c + Y_c^* Y - Y_c^* Y_c) (j\omega_k) > 0 \\
 & \text{for } i = 1, 2 \quad ; \quad \omega_n \in \Omega_N
 \end{aligned} \tag{4.10}$$

where G_1, G_2 are the plant models without and with the LVR. The optimization problem is formulated in Matlab using Yalmip [58], and solved with Mosek [59]. The algorithm converges within 7 iterations, which takes around 30 minutes on a standard laptop computer in our simple implementation.

The singular value plots of the controller as well as the achieved sensitivities are shown in Fig. 4.4. It can be seen that the frequency response of the controller cancels the resonance peaks of the plant as expected, and is also robust towards plant uncertainties. Specifically, even if the resonance frequencies in the real grid are different from the model, they are still sufficiently attenuated. The controller also successfully dampens the resonance peaks in the closed-loop response. Furthermore, the constraints on the closed-loop and input sensitivity are satisfied.

4.2.5 Simulation Results

To verify the controller performance, the example grid from Fig. 4.1 is implemented in Simulink using the Simpower toolbox. An averaged model is used for the VSIs, and the switching and DC-side dynamics are neglected. The step response of the inverter current of VSI 1 without and with the LVR is shown in Fig. 4.5. It can be seen that the transients are smooth and there is no ringing. The top of the figure shows a zoomed-in view of the step responses of $I_{t,d}^1$ and $I_{t,q}^1$ without the LVR, with the 10-90 % rise-times being 1.2 ms. With the LVR, the rise times are slower at 4.5 ms and 4.6 ms respectively. These values correspond well with the minimum desired closed-loop bandwidth of 500 Hz. The maximum overshoot is 6.7 %, and the decoupling of the d-q axes is excellent. The step responses of the VSIs 2, 3 and 4 exhibit almost equal performance.

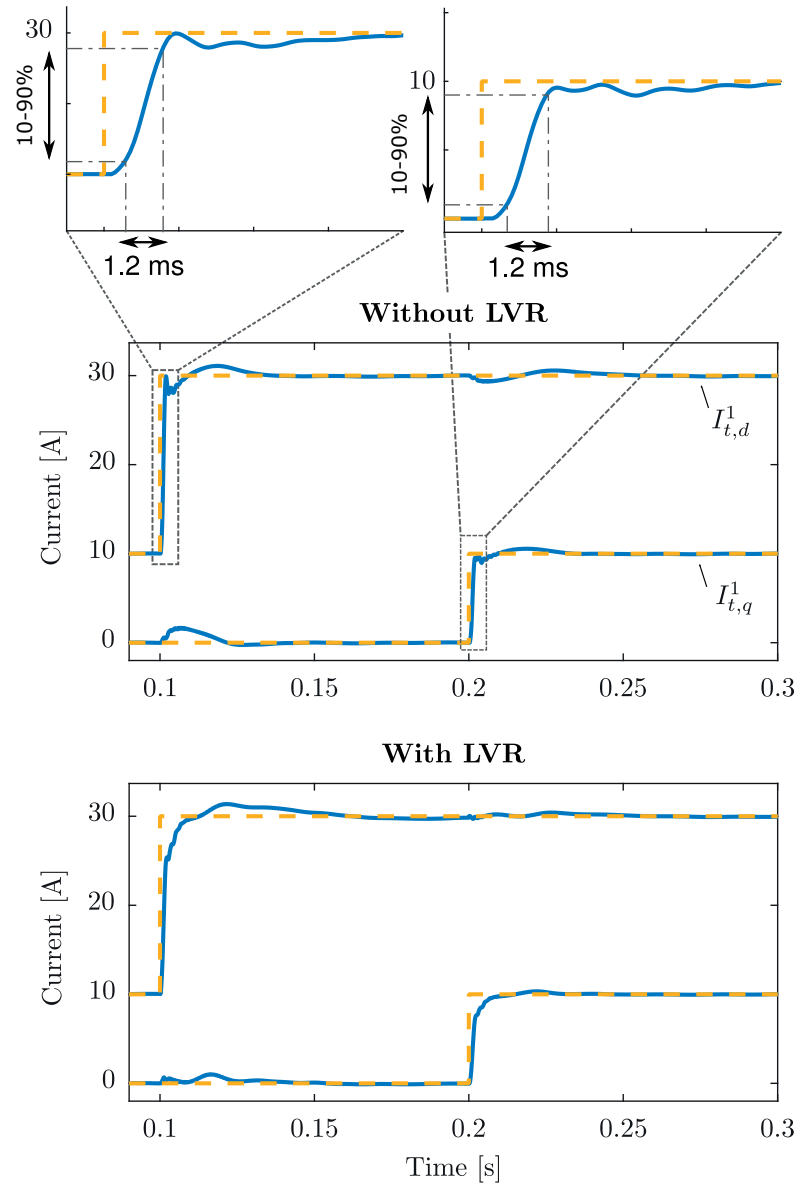


Figure 4.5 – Inverter current step response of VSI 1 without and with the LVR. The dashed line shows the current reference.

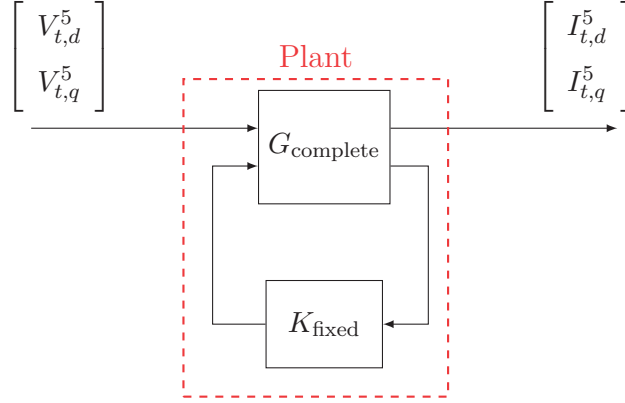


Figure 4.6 – Block diagram of plant for plug-and-play design.

4.3 Plug-and-Play Design

The control design method can also be used for plug-and-play design, where the goal is to design a current controller for a new VSI that is added to an existing grid, without retuning the current controllers of the other VSIs.

Consider again the example presented in the previous section, and let K_{fixed} be the current controller designed for VSIs 1 through 4. The goal is to design a current controller for a new VSI 5 connected to the same bus as VSIs 1 and 2 in a decentralized fashion and without changing K_{fixed} .

Again, two transfer function models of the grid without and with the LVR are constructed. Then, the existing controller K_{fixed} is used to close the feedback loops for VSIs 1 through 4. Then, a new plant with only 2 inputs and 2 outputs can be formed, where the inputs are the modulation voltage and the outputs are the inverter current of VSI 5 (see Fig. 4.6), which leads to the following controller structure:

$$\begin{bmatrix} V_{t,d}^5 \\ V_{t,q}^5 \end{bmatrix} = XY^{-1} \begin{bmatrix} I_{t,d}^5 \\ I_{t,q}^5 \end{bmatrix} \quad (4.11)$$

$$X = \begin{bmatrix} X_5^{1,1} & X_5^{1,2} \\ X_5^{2,1} & X_5^{2,2} \end{bmatrix}, \quad Y = \begin{bmatrix} Y_5^{1,1} & 0 \\ 0 & Y_5^{2,2} \end{bmatrix} \circ (z - 1)\mathbf{I}$$

$$X_5^{i,j} = X_{5,4}^{i,j}z^4 + X_{5,3}^{i,j}z^3 + X_{5,2}^{i,j}z^2 + X_{5,1}^{i,j}z + X_{5,0}^{i,j}$$

$$Y_5^{i,j} = z^4 + Y_{5,3}^{i,j}z^3 + Y_{5,2}^{i,j}z^2 + Y_{5,1}^{i,j}z + Y_{5,0}^{i,j} \quad (4.12)$$

The same performance specifications on the rise-time and overshoot as in the previous section are used, and a controller is designed. The grid is again simulated in Simulink, and the step response of the inverter current of VSI 5 without and with the LVR is shown in Fig. 4.7.

The 10-90 % rise-times of $I_{t,d}^5$, $I_{t,q}^5$ are 1.4 ms and 1.1 ms without the LVR, and 5.1 ms and 1.5 ms with the LVR, which again satisfies the specifications. The overshoot is larger than for the centrally designed controller, but is still limited to 10 %, and the decoupling is good.

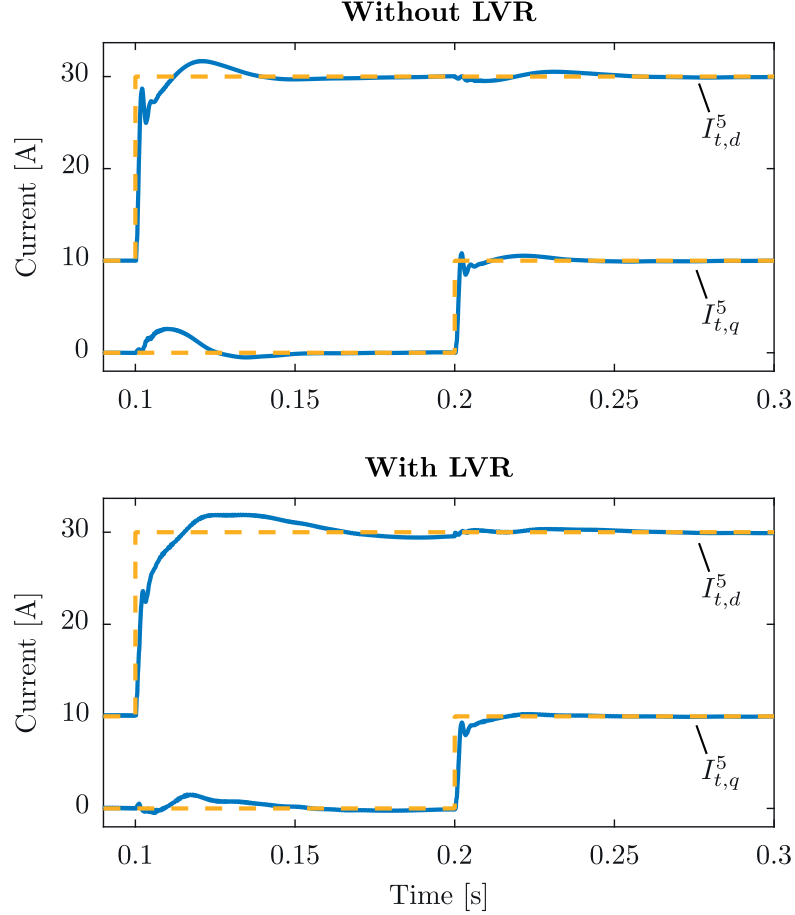


Figure 4.7 – Inverter current step response of the plug-and-play controller of VSI 5 without the LVR. The dashed line shows the current reference.

4.4 Experimental Results

To validate the simulation results obtained in the previous section, the performance of the current controllers is also implemented on a power-hardware-in-the-loop (PHIL) setup, and experimental results are obtained ¹.

¹The results in this chapter have been achieved in collaboration with Salvatore D'Arco and Atsed G. Endegnanew at SINTEF in Trondheim, Norway. The exchange has been organized by Merkebu Z. Degefa through the ERIGrid transnational access program. Thanks a lot to everyone involved!

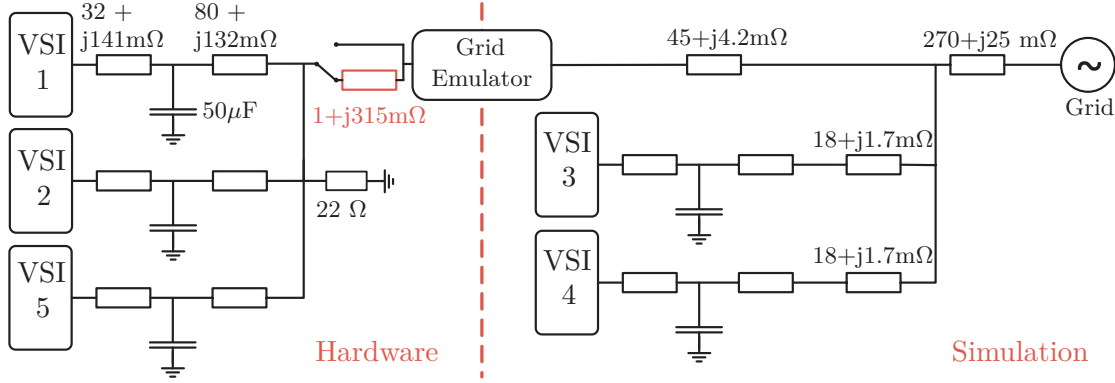


Figure 4.8 – One-line diagram of the PHIL setup. The output filter impedances are identical for all VSIs.

4.4.1 PHIL Setup

The grid layout of the PHIL experiments is shown in Fig. 4.8, and exhibits several differences compared to the simulation example. The hardware side does not contain the line impedances, and the position of the LVR has been moved such that it can be included on the hardware side. Additionally, a resistive 22Ω load is added on the hardware side to stabilize the PHIL feedback loop. For the PHIL experiment, the LVR is represented by an inductor with $R_{\text{LVR}} = 1\text{m}\Omega$ and $L_{\text{LVR}} = 1000\mu\text{H}$, with the change in voltage level being provided by the grid emulator.

The grid emulator is a 200 kW high bandwidth grid emulator (EGSTON-COMPISO). The three 2-level inverters are custom-designed prototypes with a rating of 60 kVA at 400 V ac (line-to-line RMS) and 700 V dc (see Fig. 4.9). They are identical in construction and are based on Semikron integrated IGBT modules. The converter terminals include an LCL filter on the ac side, and a dc bus capacitor with a capacitance of 4 mF. They are isolated from the grid through a decoupling transformer, the impedance of which is included in the grid impedance of the filter. The control of the converters is implemented entirely in the OPAL-RT platform where a custom programmed FPGA dedicated to sampling and conditioning of the measurements and to the generation of the gate signals is also included. The inverters are connected to the same busbars both on the dc and ac side. Additionally, during the experiments, strong 5th and 7th harmonics were observed due to the switching dead-time of the VSIs. A harmonic compensation scheme based on multiple synchronous reference frames was added in order to reduce their effect [105].

4.4.2 PHIL Results

It should be emphasized that the current controllers for the PHIL experiments were designed based on the nominal model of the grid in Fig. 4.1, which is quite different from the experimental setup. This conveniently illustrates the robustness of the designed controllers towards changes in the line impedances and grid layout.

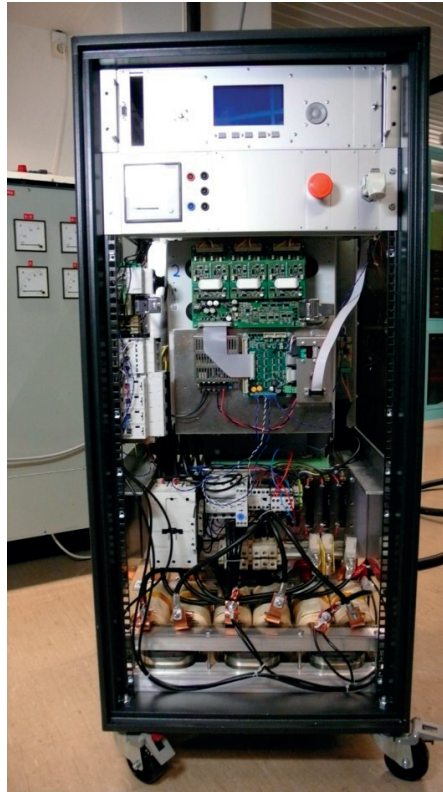


Figure 4.9 – Photo of a custom-designed inverter used for the PHIL experiments.

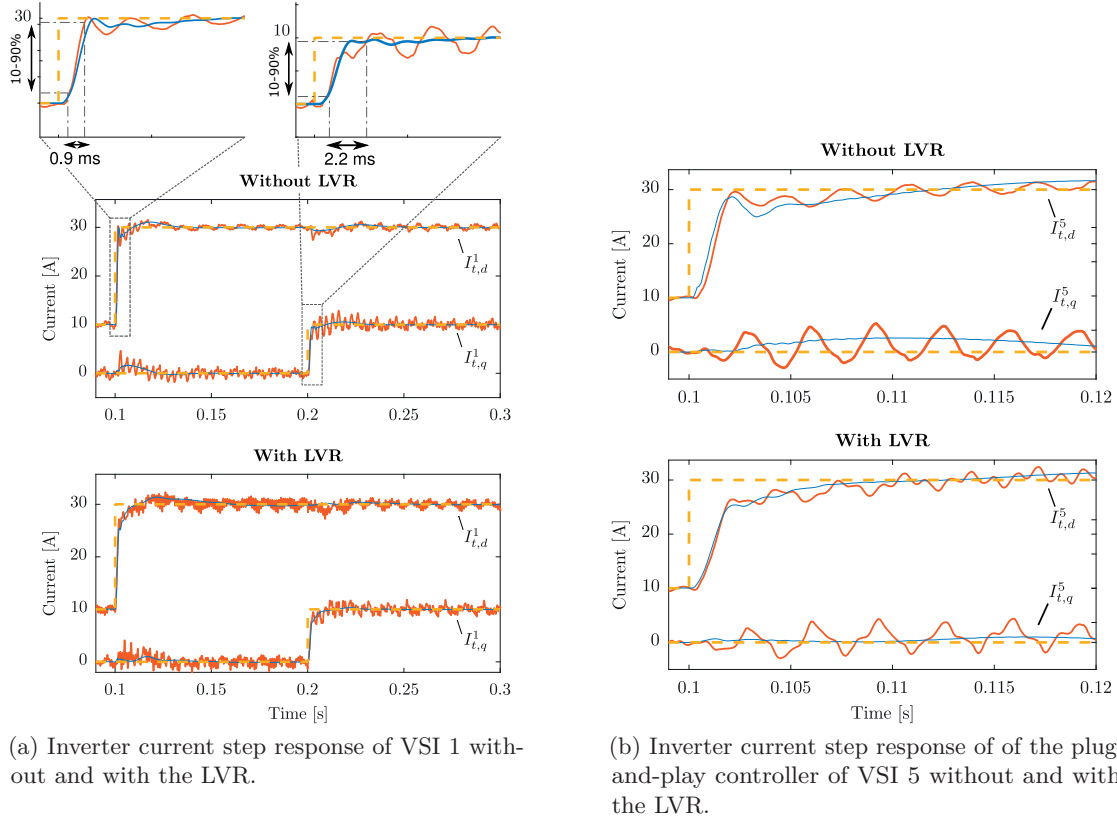


Figure 4.10 – The PHIL results are in red, simulation results are in blue, the dashed line shows the current reference.

The step response of the inverter current of VSI 1 without and with the LVR is shown in Fig. 4.10a. Similarly, the inverter current step response of VSI 5 with the plug-and-play controller is shown in Figs. 4.10b. It can be seen that the designed current controllers are able to guarantee the stability for both grid configurations in a PHIL setting. The obtained transient performance is very close to the simulation results. The difference in rise-time and overshoot are almost purely due to the harmonic oscillations present in the grid. It can also be seen that the harmonic oscillations are temporarily increased after the steps, which is due to the transient response of the harmonic compensation scheme.

Finally, the three-phase voltage and current measurements of VSI 1 during the step of $I_{t,d}^1$ without and with the LVR are shown in Fig 4.11. The obtained voltage waveform is clean, and only some minor high-frequency harmonic distortion is visible on the current.

4.5 Conclusion

A controller synthesis method for the current control design of multiple VSIs has been presented. It was shown how the frequency-domain control design method and transfer-

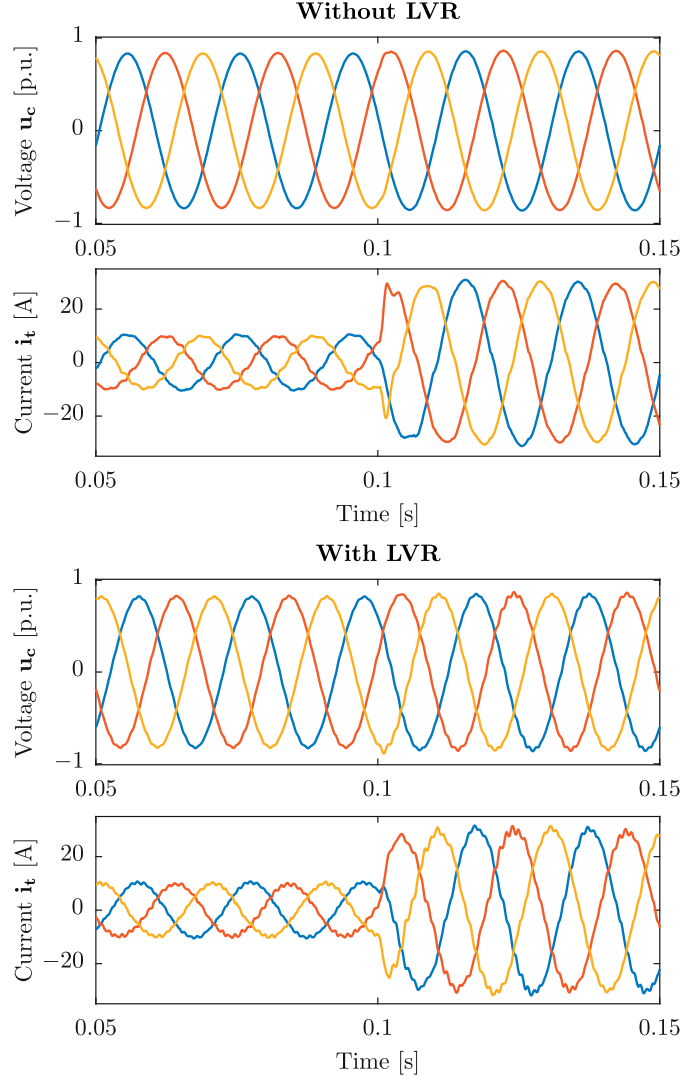


Figure 4.11 – Three-phase voltage and current of VSI 1 without and with the LVR during the step of $I_{t,d}^1$.

function model can be used to design higher-order, robust current controllers for multiple VSIs in a single step. Robust stability and performance are guaranteed by design. This is a significant advantage opposed to traditional iterative approaches where stability has to be evaluated a posteriori at each design step, which makes the tuning process lengthy and difficult.

The effectiveness of the designed controllers in addressing instability problems in power-electronics-dominated grids has been demonstrated in a realistic scenario through simulation as well as through experimental results on a PHIL setup. A very promising avenue that should be explored in future works especially for plug-and-play design is the data-driven aspect of the control design method, where a parametric model of the grid would no longer be necessary.

5 Distributed Primary and Secondary Control in Islanded Grids

5.1 Introduction

This chapter treats the problem of robust control design for distributed primary and secondary frequency and voltage control of islanded, meshed, low-voltage grids with distributed generation (also referred to as microgrids). The main control objectives are to keep the grid frequency and voltage magnitudes at each bus within a certain range from the nominal setpoints, and to balance active and reactive power flows in the grid. Traditionally, a hierarchical structure is employed: the primary level balances generation and demand, maintains frequency synchronicity and provides proportional load sharing between generation units. This is achieved via so-called droop control, which is a decentralized proportional controller that relates the active and reactive output power of a generator to the frequency and voltage magnitude at its bus. Since droop control naturally introduces a steady-state error in frequency and voltage, on a secondary control layer a centralized integral controller is used to recover the nominal values (especially for the frequency). The nominal values are given by a tertiary control layer that operates on a slow scale and is outside the scope of this chapter.

Classical power grids consist of few, high-power generators with large rotating masses that provide a lot of inertia. This leads to a system with relatively slow and well-behaved dynamics, and droop control historically provided adequate performance in most scenarios. However, in modern (micro)grids distributed generation units (DGs) are on the rise. They predominantly consist of voltage source inverter (VSI) interfaced DGs (e.g. photovoltaics or batteries), while only relatively few synchronous generators (SGs) present in the grid (e.g. hydropower or diesel generators). This results in grids with very low inertia, and requires the VSIs to participate in primary and secondary control to maintain stability. Another important issue in medium- and low-voltage grids is that the R/X -ratio of the lines is often close to 1, which means the standard decoupling assumption of active and reactive power is not applicable. This presents a challenge for standard droop controllers, whose performance is fundamentally based on this assumption. Droop control also suffers

from bad transient performance especially in grids with low inertia, being unable to actively dampen any oscillations. Furthermore, the necessary separation of timescales between decentralized droop and centralized secondary control leads to large frequency deviations and a slow recovery of the frequency after a disturbance.

5.1.1 State of the Art

This topic has gained relevance in situations such as remote communities or ship-based power grids, and has been widely treated in the literature [106]. A common approach for primary control of VSIs is the virtual synchronous generator, where the dynamics of an SG are emulated in the VSI controller [107–110]. However, no methodical way towards choosing the parameters of the virtual dynamics is given. Furthermore, the virtual SG is again controlled using droop control. Also, imposing virtual SG dynamics removes a key advantage of a VSI, which is that the frequency is not linked to a physical state.

The work in [111, 112] advocates the use of a primary controller with multiple degrees of freedom in order to improve transient stability and performance. However, no method to achieve a desired control performance is presented, and the electromagnetic line dynamics are neglected. In [113, 114] the global stability of droop control is proven, but the line resistance and electromagnetic dynamics are neglected, and control design is not treated. A systematic control design approach is pursued in [63], where an improved primary controller for a low-inertia grid is designed based on the Block Gerschgorin theorem. The drawback of this approach is that it often yields very conservative results for strongly coupled systems such as the power grid.

To achieve decoupling between active and reactive power, in [115] a transformation based on the R/X -ratio of the lines is used. However, the ratio has to be known and equal throughout the grid. A related approach is virtual impedance control, where filters are added to the VSI control scheme in order to emulate a resistive or inductive output impedance [116–118]. While this approach has the potential to improve control performance and power quality, no systematic approach to the tuning of the gains is given, and the stability can only be evaluated a posteriori. Also, the analysis is generally restricted to grids with only VSIs and no SGs.

Concerning distributed secondary control, many approaches based on distributed consensus algorithms have been presented [113, 119–122]. An extensive survey of the topic can be found in [123]. Further, in [124] the effect of communication delays on the stability and performance is studied. In [125] a distributed control architecture for stability and reactive power sharing is presented. However, while the proposed methods are able to provide secondary control without a centralized architecture, the hierarchical structure of primary and secondary control is maintained, and a separation of timescales is necessary.

To tackle some of the issues mentioned so far, various classical control design methods

Table 5.1 – Line Parameters

Line	R [Ω]	X [Ω]	Line	R [Ω]	X [Ω]
1 - 2	0.018	0.0034	4 - 8	0.09	0.017
1 - 3	0.018	0.0034	8 - 9	0.045	0.0085
2 - 7	0.15	0.11	5 - 6	0.09	0.017
2 - 10	0.3	0.22	6 - 7	0.3	0.22
3 - 4	0.45	0.085	9 - 10	0.3	0.22
3 - 5	0.3	0.22			

have been applied to design state-space controllers based on small-signal models. In [126–129] the application of optimal control design techniques for microgrids with multiple VSIs has been explored. Classical H_∞ -methods are used in [130–132] to improve the transient performance of primary frequency control. Another state-space H_∞ design method has been applied in [97, 133] to design distributed controllers for primary control. In [134] a plug-and-play approach for voltage and frequency control is proposed, and stabilizing controllers are found through optimization. However, the scope of these papers is restricted to primary control, and SGs are not considered in the model.

A general issue of state-space based methods is that they are not well suited for high-order models. This is problematic when considering power grids with multiple DGs and complete DG dynamics, which results in high-order small-signal models. To avoid the problem of high-order models, the use of dynamic phasor models has been proposed [74, 135, 136].

In this chapter, an approach is presented that aims to break the hierarchy between primary and secondary control, and results in a distributed controller that is able to provide both in a unified framework. Furthermore, the approach is well suited for grids that contain both VSIs and SGs, and the corresponding dynamics are emphasized in the design. Based on a dynamic phasor model, it is demonstrated how a large range of performance specifications such as transient performance, proportional power sharing or no frequency steady-state error can be formulated as standard frequency-domain specifications. Simulation results demonstrate the viability of the approach.

5.2 Grid Model

The design process is illustrated using an example of a 50 Hz/230 V islanded grid (see Fig. 5.1) with 2 inverter-interfaced battery energy storage systems (BESS), 1 synchronous generator (SG), 3 PV generation units and 4 constant power loads. The lines are either resistive with an R/X-ratio of 5.3, or mixed with an R/X-ratio close to 1 (see Table 5.1). Furthermore, each VSI is fitted with an LCL-type output filter. The SG is operated in speed control mode and is equipped with an internal speed controller, and the VSIs of the BESS are voltage controlled (grid forming). The PV units are represented by an ideal DC voltage source that is interfaced to the grid through a current-controlled VSI.

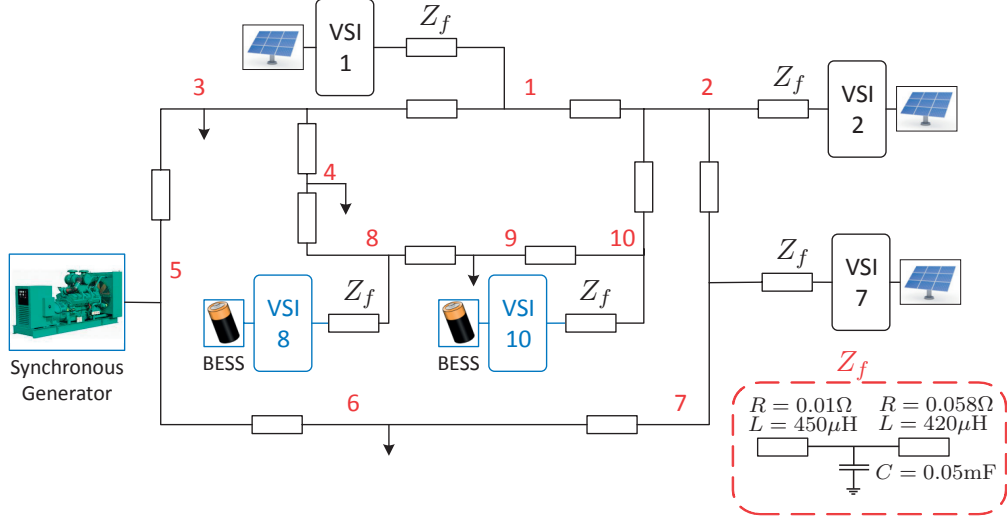


Figure 5.1 – One-line diagram of a 50 Hz/230 V islanded grid. The bus numbers are indicated in red and the arrows denote constant power loads.

Using the approach presented in Section 3.4.2, the following transfer function matrices are constructed that describe the dynamic output power of the BESS and SG:

$$\begin{aligned}
 \begin{bmatrix} P_{DG} \\ Q_{DG} \end{bmatrix} &= G_{\text{grid}} \begin{bmatrix} \omega_{DG} \\ U_{DG} \end{bmatrix} + G_d \begin{bmatrix} P_{\mathcal{L}} \\ Q_{\mathcal{L}} \end{bmatrix} \\
 [P_{DG}, Q_{DG}]^T &= [P_5, P_8, P_{10}, Q_5, Q_8, Q_{10}]^T \\
 [\omega_{DG}, U_{DG}]^T &= [\omega_5, \omega_8, \omega_{10}, U_5, U_8, U_{10}]^T \\
 [P_{\mathcal{L}}, Q_{\mathcal{L}}]^T &= [P_1, P_2, P_3, P_4, P_6, P_7, P_9, \\
 &\quad Q_1, Q_2, Q_3, Q_4, Q_6, Q_7, Q_9]^T
 \end{aligned} \tag{5.1}$$

where P_i, Q_i are the active and reactive power injected by the DG unit or load at bus i (load powers are usually negative), and ω_i, U_i are the frequency and voltage magnitude at bus i . G_{grid} is a matrix transfer function with 6 inputs and 6 outputs that describes the dynamics of the generator output powers based on the generator frequencies and voltage magnitudes. The power injected by the loads and PVs is usually stochastic and unknown, and is therefore modeled as an output disturbance, with G_d being a matrix transfer function with 14 inputs and 6 outputs.

5.2.1 VSI Dynamics

The VSIs connected to the BESS are operated in f-U mode. They receive desired setpoints for the output frequency and voltage magnitude, and are assumed to be equipped with

internal control loops that guarantee an adequate closed-loop response. The main idea is that there is no need to explicitly model the internal dynamics of the VSI and the internal controller, which are generally unknown. Rather, the dynamics of the VSI including the output filter can simply be described by the closed-loop response, which is typically provided by the manufacturer, or can be measured experimentally. For this example we assume the VSI exhibits the following closed-loop response:

$$\begin{bmatrix} \omega_{\mathcal{I}} \\ U_{\mathcal{I}} \end{bmatrix} = \begin{bmatrix} G_{\mathcal{I},\omega} & 0 \\ 0 & G_{\mathcal{I},U} \end{bmatrix} \begin{bmatrix} \bar{\omega}_{\mathcal{I}} \\ \bar{U}_{\mathcal{I}} \end{bmatrix} \quad (5.2)$$

$$G_{\mathcal{I},\omega} = \frac{1}{\tau_{\omega}s + 1}, \quad G_{\mathcal{I},U} = \frac{1}{\tau_U s + 1}$$

where $\bar{\omega}_{\mathcal{I}}, \bar{U}_{\mathcal{I}}$ are the reference VSI frequency and voltage magnitude, and τ_{ω}, τ_U are the closed-loop time constants of the frequency and voltage control loop.

This simple model is sufficient for the given example, but an advantage of the dynamic phasor model as compared to state-space models is that it can be easily extended to include detailed, high-order models without increasing the complexity. More complicated dynamics such as resonance modes, coupling effects or time delays are straightforward to consider. If measurement data is available, it is also possible to use the measured frequency response instead.

5.2.2 Synchronous Generator Dynamics

The synchronous generator is assumed to be operated in speed control mode, and the speed controller parameters are assumed to be known. The main frequency dynamics of a synchronous generator are well represented through the swing equation:

$$\frac{2H}{\bar{\omega}} \dot{\omega}_S = \frac{1}{S_S} (G_{PM} \bar{P}_{S,m} - P_S) \quad (5.3)$$

where $\bar{P}_{S,m}, P_S$ are the reference mechanical input power and the electrical output power of the generator, S_S is the rated apparent power of the generator, H is the inertia constant and G_{PM} contains the dynamics of the prime mover. The resulting transfer function is:

$$\omega_S = \begin{bmatrix} G_{S,m} & G_{S,e} \end{bmatrix} \begin{bmatrix} \bar{P}_{S,m} \\ P_S \end{bmatrix} \quad (5.4)$$

$$G_{S,m} = G_{PM} \frac{\bar{\omega}}{2HS_S}, \quad G_{S,e} = -\frac{\bar{\omega}}{2HS_S}$$

For this example, the dynamics of the prime mover are modeled with the following

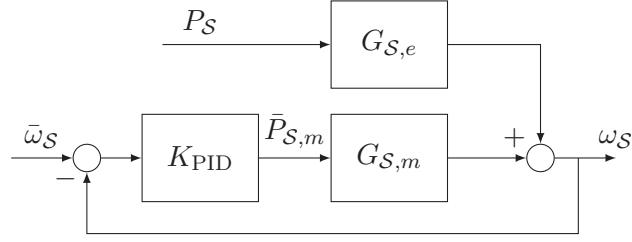


Figure 5.2 – Block diagram of speed-controlled synchronous generator.

first-order response:

$$G_{PM} = \frac{1}{\tau_m s + 1} \quad (5.5)$$

A block-diagram of the speed-controller SG is shown in Fig. 5.2, where $K_{PID} = k_p + \frac{k_i}{s} + k_d \frac{s}{T_f s + 1}$ is the speed controller. The transfer function of the closed-loop system is:

$$\omega_S = \left[\frac{K_{PID} G_{S,m}}{1 + K_{PID} G_{S,m}}, G_{S,e} \frac{K_{PID} G_{S,m}}{1 + K_{PID} G_{S,m}} \right] \begin{bmatrix} \bar{\omega}_S \\ P_S \end{bmatrix} \quad (5.6)$$

where $\bar{\omega}_S$ is the reference SG frequency. Finally, the terminal voltage is assumed to be regulated by an internal AVR with the following closed-loop response:

$$G_{S,U} = \frac{1}{\tau_U s + 1} \quad (5.7)$$

where τ_U is the time constant of the AVR. While the generator model used for this example is relatively simple, the transfer functions in (5.3) and (5.7) can easily be extended to include more complex dynamics and coupling effects, or be replaced by measured frequency responses.

5.2.3 Complete Transfer Function Model

Using the generator parameters given in Table 5.2, the dynamic phasor models for the BESS and SG in Fig. 5.1 can be computed. Then, according to Eq. 3.45 the complete dynamic phasor model of the generator dynamics can be assembled:

$$\begin{bmatrix} P_{DG} \\ Q_{DG} \end{bmatrix} = G_{comp} \begin{bmatrix} \bar{\omega}_{DG} \\ \bar{U}_{DG} \end{bmatrix} \quad (5.8)$$

$$[\bar{\omega}_{DG}, \bar{U}_{DG}]^T = [\bar{\omega}_5, \bar{\omega}_8, \bar{\omega}_{10}, \bar{U}_5, \bar{U}_8, \bar{U}_{10}]^T$$

where $\bar{\omega}_i, \bar{U}_i$ are the reference frequency and voltage magnitude of the DG at bus i . In Fig. 5.3 a block diagram of the closed-loop system is shown, where K is the controller.

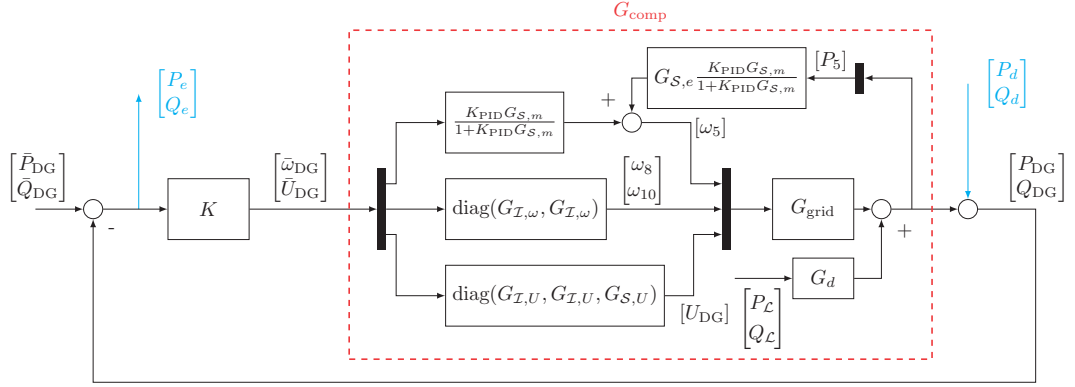


Figure 5.3 – Block diagram of complete dynamic phasor model of the grid from Fig. 5.1. The block K is the controller.

Table 5.2 – DG Units Parameters

BESS	
Bus:	[8, 10]
Output filter Parameters:	$R_t = 10\text{m}\Omega$, $L_t = 450 \mu\text{H}$ $R_g = 58\text{m}\Omega$, $L_g = 420 \mu\text{H}$, $C_f = 50 \mu\text{F}$
Time Constants:	$\tau_\omega = 5 \cdot 10^{-4}$, $\tau_U = 5 \cdot 10^{-4}$
Nom. Active/Reactive Power:	$\bar{P} = [20, 40] \text{ kW}$ / $\bar{Q} = [0, 0] \text{ pu}$
Synchronous Generator	
Bus:	[5]
Inertia Constant:	$H = 1.5$
Internal Impedance:	$R_o = 19\text{m}\Omega$, $L_o = 2.7 \text{ mH}$
Time Constants:	$\tau_m = 0.1$, $\tau_U = 0.05$
Speed Controller:	$k_p = 3.18$, $k_i = 4.77$, $k_d = 0.8$, $T_f = 0.05$
Nom. Active/Reactive Power:	$\bar{P} = 30 \text{ kW}$ / $\bar{Q} = 0 \text{ pu}$
PV	
Bus:	[1, 2, 7]
Output filter Parameters:	$R_t = 10\text{m}\Omega$, $L_t = 450 \mu\text{H}$ $R_g = 58\text{m}\Omega$, $L_g = 420 \mu\text{H}$, $C_f = 50 \mu\text{F}$
Active Power:	10 kW
Loads	
Bus:	[3, 4, 6, 9]
Active/Reactive Power:	$[-30, -20, -25, -45] \text{ kW}$ / $[0, 0, 0, 0] \text{ Var}$

A classical choice for K is a droop controller, which is commonly used in the literature for SG control and virtual inertia emulation.

5.3 Control Design

In this section, it will be shown how based on the dynamic phasor model from Chapter 3 typical performance specifications for primary and secondary control can be formulated as a robust control design problem with frequency-domain constraints.

The standard approach towards primary and secondary control for the grid in Fig. 5.3 is

to use a droop controller combined with a centralized integral controller:

$$\begin{aligned} \begin{bmatrix} \bar{\omega}_{\text{DG}} \\ \bar{U}_{\text{DG}} \end{bmatrix} &= \text{diag}(K_p, K_q) \begin{bmatrix} P_{\text{DG}} - \Delta P_{\text{DG}} \\ Q_{\text{DG}} \end{bmatrix} \quad (\text{Primary Control}) \\ [\Delta P_{\text{DG}}] &= \text{diag}(\bar{P}_5, \bar{P}_8, \bar{P}_{10}) \frac{k_i}{s} (\bar{\omega}_5 + \bar{\omega}_8 + \bar{\omega}_{10}) \quad (\text{Secondary Control}) \\ K_p &= [k_{p,5}, k_{p,8}, k_{p,10}], K_q = [k_{q,5}, k_{q,8}, k_{q,10}] \end{aligned} \quad (5.9)$$

While this controller structure provides proportional active power sharing and no steady-state error in the frequency, it also exhibits several problems:

1. SG frequency transients show large oscillations
2. R/X-ratio of lines around 1 introduces coupling between active and reactive output power and leads to large, undesired reactive power flows between DGs
3. Separation of timescale between primary and secondary control leads to slow recovery of nominal frequency
4. Centralized secondary controller necessary

The following sections will show how a single distributed controller can be designed that alleviates these issues.

5.3.1 Control Specifications

Based on the dynamic phasor model, it will now be shown how the issues listed above can be addressed using frequency domain specifications.

SG Frequency Oscillations: From Fig. 5.3, let G_{ω_5} be the open-loop transfer function from $[\bar{\omega}_{\text{DG}}, \bar{U}_{\text{DG}}]^T$ to ω_5 . Then, the transient performance of the SG frequency can be improved by minimizing the 2-norm of the transfer function $V = G_{\omega_5} K (I + G_{\text{comp}} K)$ from an output power disturbance $[P_d, Q_d]^T$ to the SG frequency ω_5 :

$$\min \|W_{\omega_5} V\|_2^2 \quad (5.10)$$

where W_{ω_5} is a weighting function. For example, if $W_{\omega_5} = \frac{1}{s}$ is chosen, this objective is equivalent to minimizing the 2-norm of the step response of the frequency to a change in output power in the time domain.

Performance in disturbance rejection and coupling: To reduce the coupling between active and reactive output power and vice versa, the sensitivity function $S =$

$(I + G_{\text{comp}}K)^{-1}$ is split into 4 parts:

$$\begin{bmatrix} P_e \\ Q_e \end{bmatrix} = \begin{bmatrix} S_{11} & S_{12} \\ S_{21} & S_{22} \end{bmatrix} \begin{bmatrix} P_d \\ Q_d \end{bmatrix} \quad (5.11)$$

Nominal performance can be guaranteed through the diagonal elements:

$$\min_K \|W_1 S_{11}\|_2^2, \min_K \|W_2 S_{22}\|_2^2 \quad (5.12)$$

where W_1, W_2 are performance weights. The coupling is reduced by minimizing the off-diagonal elements:

$$\min_K \|S_{12}\|_2^2, \min_K \|S_{21}\|_2^2 \quad (5.13)$$

Power Sharing: Proportional active power sharing can be achieved by shaping the sensitivity S_{11} defined above. Proportional power sharing means that in steady-state any active output power disturbance (e.g. a change in load) should be shared proportionally among the generators. For example, assume an active power disturbance $P_{d,5}$ is applied to the SG at bus 5:

$$\begin{bmatrix} P_{e,5} \\ P_{e,8} \\ P_{e,10} \end{bmatrix} = S_{11} \begin{bmatrix} P_{d,5} \\ 0 \\ 0 \end{bmatrix} \quad (5.14)$$

Then, if power is shared proportionally the following steady-state tracking errors should be obtained:

$$P_{e,5} = \frac{\bar{P}_5}{P_{\text{tot}}} P_{d,5}, \quad P_{e,8} = \frac{\bar{P}_8}{P_{\text{tot}}} P_{d,5}, \quad P_{e,10} = \frac{\bar{P}_{10}}{P_{\text{tot}}} P_{d,5} \quad (5.15)$$

where $P_{\text{tot}} = \bar{P}_5 + \bar{P}_8 + \bar{P}_{10}$. The same relation should also hold for the other disturbances, which means $S_{11}(\omega = 0)$ should take the following value:

$$S_{11}^0 = \frac{1}{P_{\text{tot}}} \begin{bmatrix} \bar{P}_5 & \bar{P}_5 & \bar{P}_5 \\ \bar{P}_8 & \bar{P}_8 & \bar{P}_8 \\ \bar{P}_{10} & \bar{P}_{10} & \bar{P}_{10} \end{bmatrix} \quad (5.16)$$

This leads to the following constraint:

$$S_{11}(\omega = 0) = S_{11}^0 \quad (5.17)$$

Frequency and Voltage Performance: The maximum deviation of the frequency and voltage magnitudes after an output power disturbance as well as the frequency steady-state error can be limited through shaping the input sensitivity $U = K(I + G_{\text{comp}}K)$,

where:

$$\begin{bmatrix} \omega_{\text{DG}} \\ U_{\text{DG}} \end{bmatrix} = \begin{bmatrix} U_{11} & U_{12} \\ U_{21} & U_{22} \end{bmatrix} \begin{bmatrix} P_d \\ Q_d \end{bmatrix} \quad (5.18)$$

The maximum deviation of the frequency and voltage can be limited by constraining the weighted infinity-norm of U :

$$\|W_3 U\|_\infty \leq 1, \quad W_3 = \begin{bmatrix} W_{31} & 0 \\ 0 & W_{32} \end{bmatrix} \quad (5.19)$$

where W_{31}, W_{32} are the performance weights. A higher weight will result in a lower deviation. Furthermore, in order to reduce the frequency steady-state error W_{31} should have high gain (which in turn leads U_{11}, U_{12} to be small) at low frequencies.

Complete Design Problem: Combining these specifications leads to the following multiobjective optimization problem:

$$\begin{aligned} \min_K \quad & \underbrace{\|W_{\omega_5} V\|_2^2}_{\text{SG Frequency}} + \underbrace{\|W_1 S_{11}\|_2^2 + \|W_2 S_{22}\|_2^2}_{\text{Disturbance Rejection}} + \underbrace{\|S_{12}\|_2^2 + \|S_{21}\|_2^2}_{\text{Decoupling}} \\ \text{subject to:} \quad & \\ S_{11}(j\omega = 0) = S_{11}^0 \quad & \text{(Power Sharing)} \\ \|W_3 U\|_\infty \leq 1 \quad & \text{(Frequency/Voltage Performance)} \end{aligned} \quad (5.20)$$

5.3.2 Controller Structure

As the design is based upon frequency-domain methods, it is possible to directly design a discrete-time controller using the frequency response of a continuous-time plant. It is assumed that the DGs at buses 5 and 10 are able to communicate with the DG at bus 8, but not directly with each other. There is also a communication delay of 10 ms between the DGs. Then, a 6th-order distributed controller structure with a sampling

time $T_s = 0.001$ s is chosen as follows:

$$\begin{aligned}
 & \begin{bmatrix} \bar{\omega}_5, \bar{U}_5, \bar{\omega}_8, \bar{U}_8, \bar{\omega}_{10}, \bar{U}_{10} \end{bmatrix} \\
 &= XY^{-1} \begin{bmatrix} P_{e,5}, Q_{e,5}, P_{e,8}, Q_{e,8}, P_{e,10}, Q_{e,10} \end{bmatrix} \\
 X(z) &= (X_6 z^6 + \dots + X_1 z + X_0) \circ F_x \\
 Y(z) &= Iz^6 \dots + Y_1 z + Y_0
 \end{aligned} \tag{5.21}$$

$$X_i = \begin{bmatrix} \begin{array}{cc|cc|cc} \text{Local} & & \text{Distributed} & & & \\ \hline X_i^{1,1} & X_i^{1,2} & X_i^{1,3} & X_i^{1,4} & 0 & 0 \\ X_i^{2,1} & X_i^{2,2} & X_i^{2,3} & X_i^{2,4} & 0 & 0 \\ \hline X_i^{3,1} & X_i^{3,2} & X_i^{3,3} & X_i^{3,4} & X_i^{3,5} & X_i^{3,6} \\ X_i^{4,1} & X_i^{4,2} & X_i^{4,3} & X_i^{4,4} & X_i^{4,5} & X_i^{4,6} \\ \hline 0 & 0 & X_i^{5,3} & X_i^{5,4} & X_i^{5,5} & X_i^{5,6} \\ 0 & 0 & X_i^{6,3} & X_i^{6,4} & X_i^{6,5} & X_i^{6,6} \end{array} \end{bmatrix} \tag{5.22}$$

$$F_x = \begin{bmatrix} \mathbf{1} & z^{-10}\mathbf{1} & 0 \\ z^{-10}\mathbf{1} & \mathbf{1} & z^{-10}\mathbf{1} \\ 0 & z^{-10}\mathbf{1} & \mathbf{1} \end{bmatrix} \tag{5.23}$$

$$Y_i = \text{diag}(Y_i^1, Y_i^2, Y_i^3, Y_i^4, Y_i^5, Y_i^6) \tag{5.24}$$

where $X_i^{n,m}, Y_i^n \in \mathbb{R}$ are variables denoting the controller parameters, F_x is a fixed-term describing the communication delay and \circ denotes the element-wise matrix multiplication. For the formulation of the optimization, the entries are pivoted to match the in- and outputs of the plant in (5.8).

5.3.3 Convex Formulation

An obvious choice of initial controller for this case is an augmented version of the droop controller:

$$X_c = \text{diag}(K_p, K_q)z^6, \quad Y_c = Iz^6 \tag{5.25}$$

where the order is increased to satisfy the conditions on the order of the initial controller imposed by the design algorithm.

To formulate the constraints in the given framework, the following transformation can

be applied to S :

$$\begin{bmatrix} S_{11} & \epsilon S_{12} \end{bmatrix} = \underbrace{\begin{bmatrix} I & 0 \end{bmatrix}}_{W_{11}} S \underbrace{\text{diag}(I, \epsilon I)}_{W_{12}} \quad (5.26)$$

$$\begin{bmatrix} \epsilon S_{21} & S_{22} \end{bmatrix} = \underbrace{\begin{bmatrix} 0 & I \end{bmatrix}}_{W_{21}} S \underbrace{\text{diag}(\epsilon I, I)}_{W_{22}} \quad (5.27)$$

where $\epsilon \in \mathbb{R}$ is a small number to make W_{12}, W_{22} invertible. Then, the performance objectives in Eqs. 5.12 and 5.13 can be approximated as follows:

$$\|W_1(W_{11}SW_{12})\|_2^2 = \|W_1[S_{11} \quad \epsilon S_{12}]\|_2^2 = \|W_1S_{11}\|_2^2 + \epsilon^2\|W_1S_{12}\|_2^2 \approx \|W_1S_{11}\|_2^2 \quad (5.28)$$

and equivalently:

$$\|W_2(W_{21}SW_{22})\|_2^2 = \|W_2S_{22}\|_2^2 + \epsilon^2\|W_2S_{21}\|_2^2 \approx \|W_2S_{22}\|_2^2 \quad (5.29)$$

$$\|W_{11}SW_{22}\|_2^2 = \|S_{12}\|_2^2 + \epsilon^2\|S_{11}\|_2^2 \approx \|S_{12}\|_2^2 \quad (5.30)$$

$$\|W_{21}SW_{12}\|_2^2 = \|S_{21}\|_2^2 + \epsilon^2\|S_{22}\|_2^2 \approx \|S_{21}\|_2^2 \quad (5.31)$$

Another practical problem arises from the power sharing constraint formulated in (5.17). As the plant contains an integrator, its frequency response at $\omega = 0$ is infinite, which means the LMI constraint cannot be formulated. This can be resolved by instead evaluating the following 2-norm constraint at the lowest frequency point:

$$\begin{aligned} & \min_{X,Y} \|W_{11}S(j\omega_1)W_{12} - [S_{11}^0 \quad 0]\|_2^2 \\ & = \min_{X,Y} \|S_{11}(j\omega_1) - S_{11}^0\|_2^2 + \epsilon^2\|S_{12}(j\omega_1)\|_2^2 \approx \min_{X,Y} \|S_{11}(j\omega_1) - S_{11}^0\|_2^2 \end{aligned} \quad (5.32)$$

Since $S(j\omega_1)$ has imaginary components, the equality constraint from (5.17) has to be relaxed by formulating a minimization problem instead. This also has the additional benefit of guaranteeing a minimum bandwidth ω_1 after which proportional power sharing is achieved.

Then, using the method presented in Chapter 2 the robust control design problem in Eq. (5.20) can be written as a convex optimization problem with LMI constraints:

$$\begin{aligned}
 \min_{X,Y} \sum_{k=1}^N & \underbrace{\text{trace}(\Gamma_{\omega,k})}_{\text{SG Frequency}} + \underbrace{\text{trace}(\Gamma_{S_{11},k}) + \text{trace}(\Gamma_{S_{22},k})}_{\text{Disturbance Rejection}} \\
 & + \alpha_1 \underbrace{(\text{trace}(\Gamma_{S_{12},k}) + \text{trace}(\Gamma_{S_{21},k}))}_{\text{Decoupling}} + \alpha_2 \underbrace{(\text{trace}(\Gamma_{ps,k}))}_{\text{Power Sharing}}
 \end{aligned} \tag{5.33}$$

subject to:

$$\begin{aligned}
 & \begin{bmatrix} \Gamma_{\omega,k} & (W_{\omega_5} G_{\omega_5} X)^* \\ W_{\omega_5} G_{\omega_5} X & P^* P_c + P_c^* P - P_c^* P_c \end{bmatrix} (j\omega_k) > 0 \\
 & \begin{bmatrix} \Gamma_{S_{11},k} & (W_1 W_{11} Y)^* \\ W_1 W_{11} Y & P_{W_{12}}^* P_{c,W_{12}} + P_{c,W_{12}}^* P_{W_{12}} - P_{c,W_{12}}^* P_{c,W_{12}} \end{bmatrix} (j\omega_k) > 0 \\
 & \begin{bmatrix} \Gamma_{S_{22},k} & (W_2 W_{21} Y)^* \\ W_2 W_{21} Y & P_{W_{22}}^* P_{c,W_{22}} + P_{c,W_{22}}^* P_{W_{22}} - P_{c,W_{22}}^* P_{c,W_{22}} \end{bmatrix} (j\omega_k) > 0 \\
 & \begin{bmatrix} \Gamma_{S_{12},k} & (W_{11} Y)^* \\ W_{11} Y & P_{W_{22}}^* P_{c,W_{22}} + P_{c,W_{22}}^* P_{W_{22}} - P_{c,W_{22}}^* P_{c,W_{22}} \end{bmatrix} (j\omega_k) > 0 \\
 & \begin{bmatrix} \Gamma_{S_{21},k} & (W_{21} Y)^* \\ W_{21} Y & P_{W_{12}}^* P_{c,W_{12}} + P_{c,W_{12}}^* P_{W_{12}} - P_{c,W_{12}}^* P_{c,W_{12}} \end{bmatrix} (j\omega_k) > 0 \\
 & \begin{bmatrix} P^* P_c + P_c^* P - P_c^* P_c & (W_3 X)^* \\ W_3 X & I \end{bmatrix} (j\omega_k) > 0 \\
 & \begin{bmatrix} \Gamma_{ps,k} & \mathbf{W}^* \\ \mathbf{W} & P_{W_{12}}^* P_{c,W_{12}} + P_{c,W_{12}}^* P_{W_{12}} - P_{c,W_{12}}^* P_{c,W_{12}} \end{bmatrix} (j\omega_1) > 0 \\
 & \mathbf{W} = W_{11} Y - [S_{11}^0 \quad 0] W_{12}^{-1} (Y + G X) \\
 & Y^* Y_c + Y_c^* Y - Y_c^* Y_c > 0 \\
 & \forall \omega_k \in \Omega_N
 \end{aligned}$$

where $P = Y + G_{\text{comp}} X$, $P_c = Y_c + G_{\text{comp}} X_c$. The scalars $\alpha_i \in \mathbb{R}$ are weighting factors that denote the importance of the respective criterion.

5.4 Simulation Results

Now, a controller can be designed by solving the convex optimization problem given in (5.33). To improve numerical stability, all controller inputs and outputs are normalized to per unit with the following values:

$$U_{\text{base}} = 325 \text{ V}, \quad \omega_{\text{base}} = 50 \cdot 2\pi \text{ rad/s}, \quad S_{\text{base}} = 100 \text{ kW} \tag{5.34}$$

When choosing the original frequency droop gains, there is a trade-off: higher gains

Chapter 5. Distributed Primary and Secondary Control in Islanded Grids

reduce the steady-state error, but also introduce oscillations in the response. Similarly, higher voltage droop gains reduce the reactive power flows, but also increase the deviation from the nominal voltage. Droop gains with acceptable performance have been chosen as follows:

$$K_p = [0.02, 0.03, 0.015], K_q = [0.1, 0.1, 0.1], k_i = 100 \quad (5.35)$$

where the integral gain k_i is chosen to achieve a separation of timescales between primary and secondary control.

The performance weights W_1, W_2, W_{ω_5} are set equal to 1. This choice leads to less overall oscillations in frequency and voltage, and reduces the frequency nadir of the SG. Furthermore, while ideally ϵ should be very small, this may lead to numerical difficulties during the optimization. For this example, $\epsilon = 0.01$ is sufficiently small to achieve the desired performance while avoiding numerical problems. The weighting factors are chosen as $\alpha_1 = 40$ and $\alpha_2 = 400$ to put a large emphasis on decoupling and accurate power sharing.

For the input sensitivity U , the following filter is chosen:

$$W_3 = \text{blkdiag} \left(\alpha_3 \frac{s}{s+10} I, \alpha_4 I \right)^{-1} \quad (5.36)$$

$$\alpha_3 = 0.06, \alpha_4 = 0.3 \quad \forall \omega \leq 100 \text{ rad/s}$$

$$\alpha_3 = 0.12, \alpha_4 = 0.6 \quad \forall \omega > 100 \text{ rad/s}$$

Adding this inverse of a high-pass filter to the weighting function of the frequency will remove the steady-state error in the frequency below a bandwidth of 10 rad/s. Furthermore, the constraint is relaxed in frequencies above 100 rad/s to allow larger input action, which improves transient behavior.

The problem is sampled using 400 logarithmically-spaced frequency points in the interval $\Omega_N = \{10^{-1}, 10^3 \cdot \pi\}$ rad/s where the upper limit is the Nyquist frequency of the controller. The optimization problem is then formulated in Matlab using Yalmip [58], and solved with Mosek [59]. The algorithm converges within 6 iterations, which takes around 45 minutes on a standard desktop computer in our simple implementation.

To validate the performance of the obtained controller, the example grid from Fig. 5.1 is implemented in Simulink using the Simpower toolbox. The VSIs of the BESS and PVs are modeled using average models, and the DC-side dynamics are neglected. The SG is modeled using the ‘Simplified Synchronous Machine’ model from the Simpower toolbox, which on the mechanical side models the swing equation, and on the electrical side consists of a voltage source behind a synchronous reactance and resistance.

The response of the new controller after an active power load step is compared with a

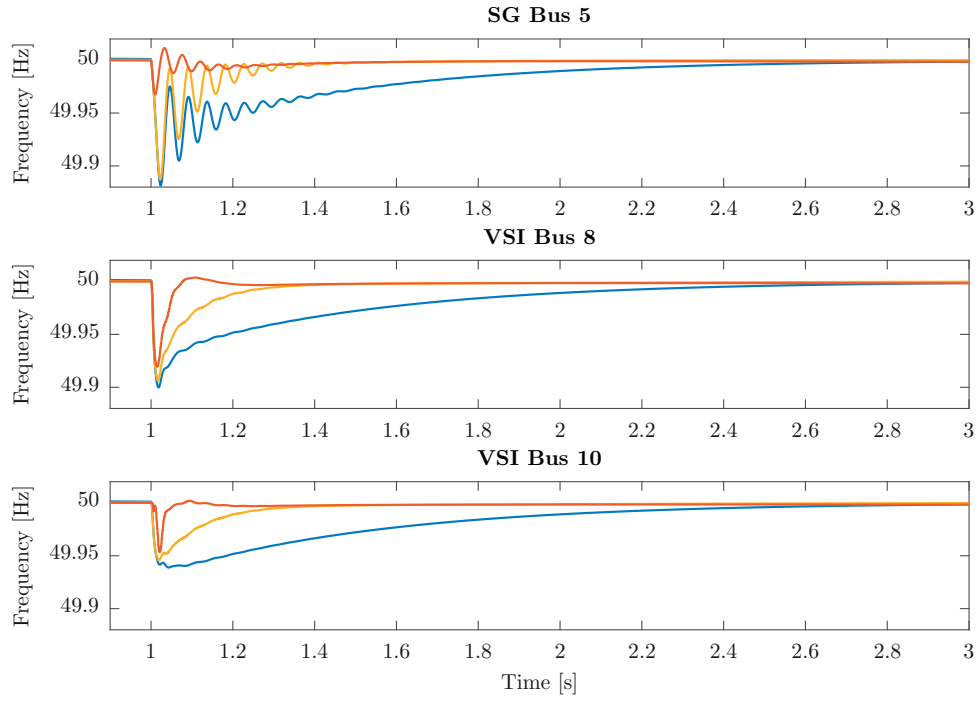


Figure 5.4 – Frequency of the DG units after an active power load step. The new controller is in red, droop in blue and DAPI in yellow.

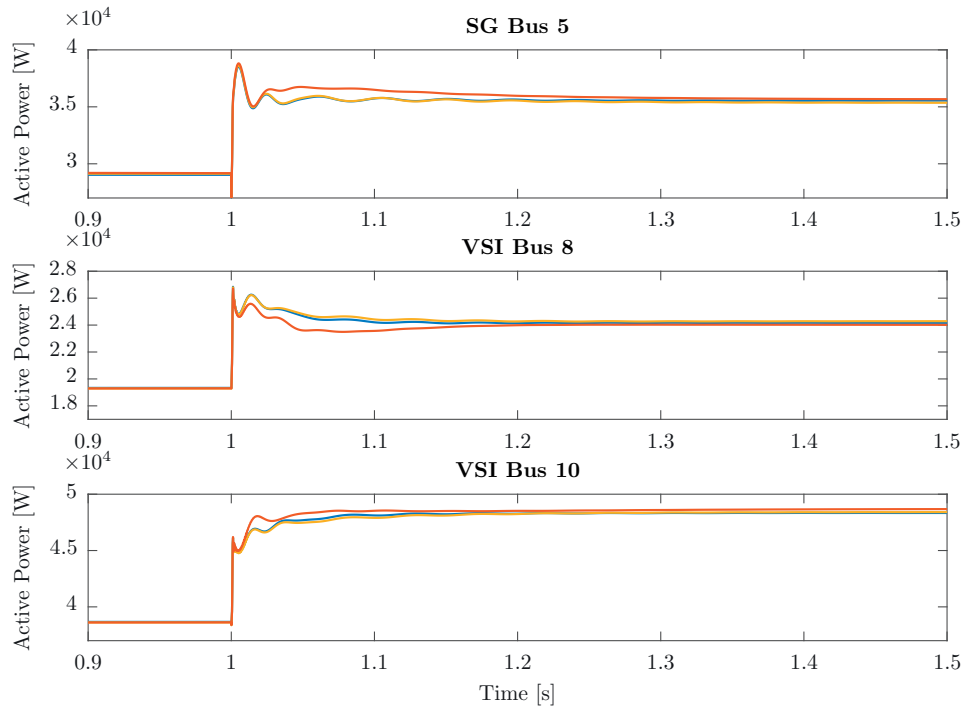


Figure 5.5 – Active output power of the DG units after an active power load step. The new controller is in red, droop in blue and DAPI in yellow.

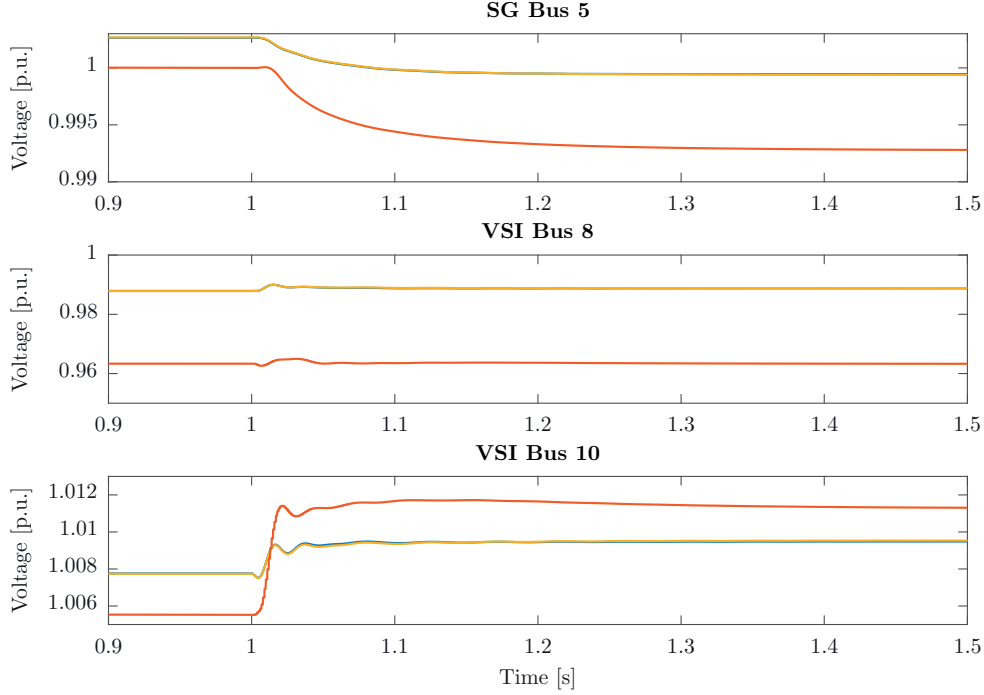


Figure 5.6 – Voltage magnitude of the DG units after an active power load step. The new controller is in red, droop in blue and DAPI in yellow.

classical droop controller with centralized secondary control, as well as with a droop controller with a distributed averaging PI (DAPI) control scheme presented in [113]. The gains of the droop controller are taken from (5.35), and for the DAPI controller also $k_i = 100$ is chosen.

For all three controllers, the active power load at bus 6 is stepped up from 25 kW to 50 kW at $t = 1$ s. In Fig. 5.4 the frequency transient after the load step is shown. It can be seen that both for droop and DAPI, the SG frequency experiences significant oscillation. Further, due to the separation of timescales between primary and secondary control, it takes a long time until the nominal frequency is recovered. On the other hand, the controller designed in this paper is able to reduce the frequency nadir of the SG by more than 75% while improving the settling time, and recovers the nominal frequency significantly faster.

Figure 5.5 shows the active output power of the DGs. It can be seen that the new controller provides smooth transients, and that all methods achieve proportional power sharing. The voltage magnitude and reactive output power of the DGs is shown in Fig. 5.6 and Fig. 5.7, respectively. It can be seen that the new controller significantly reduces the reactive output powers. This is achieved through a trade-off by allowing larger voltage deviations at steady-state, which is acceptable as long as the voltage remains

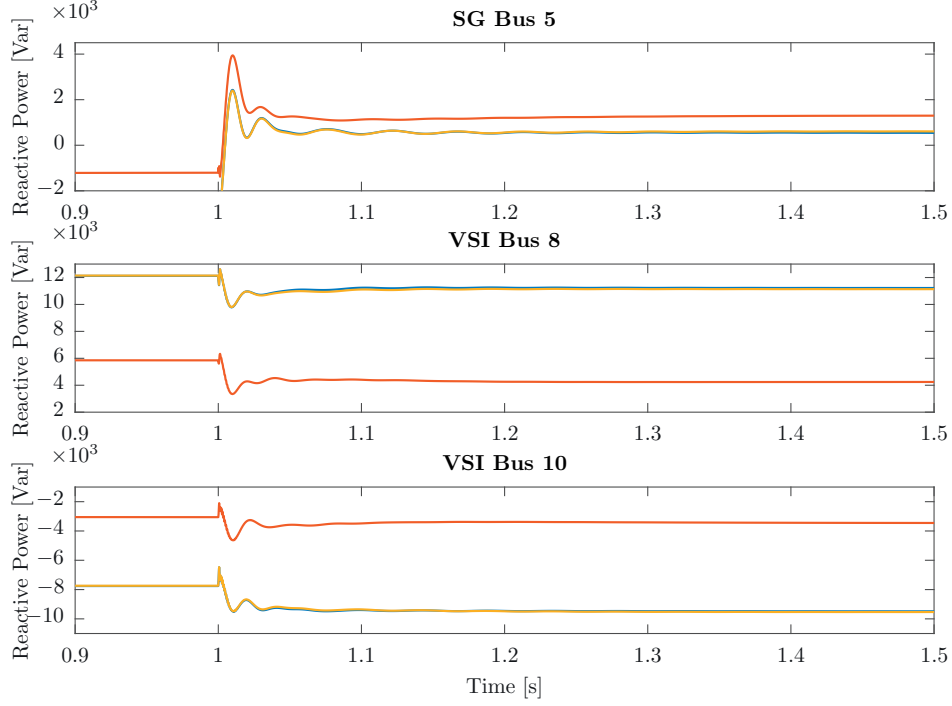


Figure 5.7 – Reactive output power of the DG units after an active power load step. The new controller is in red, droop in blue and DAPI in yellow.

within the nominal limits. By decreasing the parameter α_4 in (5.36), the voltage deviation can be reduced if deemed necessary. Note that in order to achieve the same behaviour with droop control, the gains K_q would have to be increased. However, increasing K_q also introduces oscillatory behaviour both in active and reactive power, and gains higher than 0.4 result in instability, which further demonstrates the inadequacy of droop control in the given scenario.

5.5 Conclusion

It has been shown how the problem of primary and secondary control design for islanded microgrids with both voltage source inverters and synchronous generators can be expressed in an H_2 and H_∞ framework. Expressing desired performance specifications as convex constraints on sensitivity functions makes it possible to apply a convex optimization method to design the controller parameters. This results in a systematic design approach that guarantees robust stability and allows the realization of difficult performance objectives such as proportional active power sharing. The approach also allows to combine primary and secondary control in a single framework, and to consider communication time delays during the design. Simulation results show that significantly superior performance can be achieved as compared to classical hierarchical droop approaches.

The given example lends itself towards various interesting extensions such as more accurate generator models or different types of loads. Furthermore, the given performance specifications could be refined, and more study into the effect of time-delays is warranted. Finally, the data-driven aspect has not yet been considered in this work, and would provide a very interesting and relevant topic for further research.

5.A Primary and Secondary Control Design: Additional Results

The initial publications related to this project did not yet consider a unified architecture for primary and secondary control, and relied on the classical hierarchical structure [6, 7]. Some results of these studies will be shown in this appendix.

5.A.1 Example Grid

A grid model based on the three-phase islanded Subnetwork 1 of the CIGRE benchmark medium voltage distribution network is used [137]. The network is a meshed network with mixed lines consisting of 11 buses (see Fig. 5.8).

The following modifications are made compared to the original system: the nominal phase-to-phase RMS voltage is lowered from 20 kV to 3.3 kV. Only 2 VSI-interfaced battery storage units connected to buses 5, 9 and one SG connected to bus 10 are considered. The photovoltaics are assumed to operate in maximum power point tracking mode and are absorbed into the loads. The loads at buses 1, 5, 9 and 10 are neglected. Since the grid is running in islanded mode, the loads and power ratings of the generation units are scaled such that nominal generation and load is at an equilibrium. To prevent the dynamics from being dominated by a single generation unit, the power ratings are in a similar range for all three units.

The line impedances of the grid are taken from [137], the other relevant parameters are listed in Table 5.3, including the values of the initial droop controller. R_f, L_f are the resistance and inductance of the VSI L -type output filters, R_o, L_o the resistance and inductance of the internal impedance of the SG. Finally, the line between buses 9 and 10 can be opened or closed, leading to a change in topology.

5.A.2 Improved Primary Control Performance

In a first step, the goal is to design a decentralized controller to improve the frequency and voltage transient performance, while maintaining proportional active power sharing. The VSI output filters and the internal impedance of the SG are lumped with the line impedances. The line 9-10 is assumed to be open. For the sensor dynamics, the active

5.A. Primary and Secondary Control Design: Additional Results

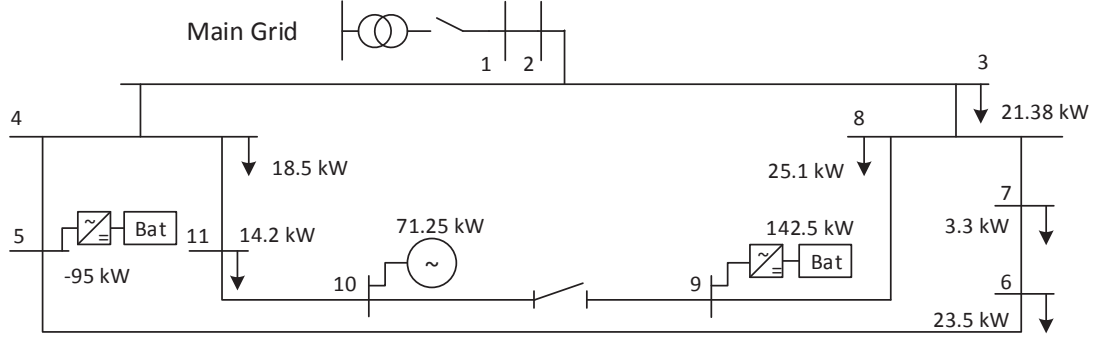


Figure 5.8 – Model adapted from [137] with 11 buses, 2 inverter-interfaced batteries, 1 synchronous generator and 6 loads. The sign \downarrow denotes the loads.

Table 5.3 – CIGRE Grid Parameters

Base Values	$S_{base} = 475 \text{ kVA}$, $U_{base} = 3.3 \text{ kV}$, $f = 50 \text{ Hz}$
Batteries	
bus	[5 9]
$R_f = 0.5 \Omega$	$L_f = 10 \cdot 10^{-3} \text{ H}$
$\tau_\omega = 5 \cdot 10^{-4}$	$\tau_U = 5 \cdot 10^{-4}$
\bar{P}_I	[-0.2 0.3] pu
\bar{Q}_I	[0.07 0.07] pu
k_p^{VSI}	diag(1.3125, 0.875) $\frac{\text{Hz}}{\text{pu}}$
k_q^{VSI}	diag(110, 110) $\frac{\text{V}}{\text{pu}}$
Diesel Generator	
bus	[10]
$R_o = 0.011 \Omega$	$L_o = 15.6 \cdot 10^{-3} \text{ H}$
Inertia Constant	1.5
$\tau_m = 0.1$	$\tau_U = 0.1$
\bar{P}_S	[0.15] pu
\bar{Q}_S	[0.07] pu
k_ω^{SG}	$\frac{1}{1.75} \frac{\text{pu}}{\text{Hz}}$
k_q^{SG}	110 $\frac{\text{V}}{\text{pu}}$
Loads	
bus	[3 4 6 7 8 11]
$P_{\mathcal{L}}$	[0.050 0.043 0.054 0.008 0.058 0.033] pu
$Q_{\mathcal{L}}$	[0 0 0.211 0 0 0] pu

Chapter 5. Distributed Primary and Secondary Control in Islanded Grids

and reactive power measurements are filtered using a first-order low-pass filter with a cutoff frequency of 50 Hz. The SG frequency measurement is assumed to not have any sensor dynamics.

The plant model G_{comp} is then constructed as shown in Section 3.4.5

Performance Specifications

The closed-loop response of the initial droop controller exhibits long settling times and exorbitant ringing. In order to address these issues, a 6th-order decentralized controller with a sampling time of $T_s = 1$ ms is designed that guarantees stability and proportional power sharing, while significantly improving the transient performance. All inputs and outputs of the plant are normalized to per unit, using the base power, voltage and frequency given in Table 5.3.

The main control objective for this scenario is to dampen the oscillations in the frequency transients of the SG after a change in output power. Therefore, as objective function the infinity norm of the weighted sensitivity $\|W_1 S\|_\infty$ is minimized, where the weighting filter is chosen as $W_1 = \text{diag}(0, 0, 0, 0, 0, 1)$.

Additionally, the maximum input sensitivity is constrained to prevent excessive control action and guarantee good transient performance. Also, a roll-off at high frequencies is added to the input sensitivity weight in order to prevent undesired fast oscillations in the inputs:

$$\|W_2 K S\|_\infty < 1 \quad (5.37)$$

The entries of the performance weight are chosen based on the input sensitivity U_{droop} of the initial droop controller:

$$W_2^{-1} = 2 \text{ diag}(1.05, 1.08, 0.13, 0.11, 0.18, 300) B$$

where the values in the diagonal matrix are equal to the maximum singular values of the individual rows of U_{droop} , and B is a second-order discrete-time Butterworth low-pass filter with a cutoff frequency of 500 rad/s. The factor 2 can be seen as a tuning parameter in order to increase or decrease the overall input sensitivity.

Proportional power sharing is maintained by constraining the steady-state gains of the new controller to be equal to the droop gains. The constraint can be formulated as follows:

$$X(1)Y(1)^{-1} = \text{diag}(k_p^{\text{VSI}}, k_q^{\text{VSI}}, k_q^{\text{SG}}, k_\omega^{\text{SG}}) \quad (5.38)$$

which can be expressed as a linear equality constraint:

$$\sum_{i=1}^4 X_i = \text{diag}(k_p^{\text{VSI}}, k_q^{\text{VSI}}, k_q^{\text{SG}}, k_\omega^{\text{SG}}) \sum_{i=1}^4 Y_i \quad (5.39)$$

As stabilizing initial controller, the original droop controller is used:

$$X_c(z) = \text{diag}(k_p^{\text{VSI}}, k_q^{\text{VSI}}, k_q^{\text{SG}}, k_\omega^{\text{SG}}) \quad ; \quad Y_c(z) = I \quad (5.40)$$

The problem is sampled using 600 logarithmically-spaced frequency points in the interval $\Omega_N = \{1, 10^3\pi\}$ rad/s where the upper limit is the Nyquist frequency of the controller.

Finally, the control design problem is reformulated as a convex optimization problem:

$$\begin{aligned} & \min_{X,Y} \gamma & (5.41) \\ & \text{subject to:} \\ & \begin{bmatrix} P^*P_c + P_c^*P - P_c^*P_c & (W_1Y)^* \\ W_1Y & \gamma I \end{bmatrix} (j\omega_n) > 0 \\ & \begin{bmatrix} P^*P_c + P_c^*P - P_c^*P_c & (W_2X)^* \\ W_2X & I \end{bmatrix} (j\omega_n) > 0 \\ & [Y_c^*Y + Y^*Y_c - Y_c^*Y_c] (j\omega_n) > 0 \\ & \sum_{i=1}^4 X_i = \text{diag}(k_p^{\text{VSI}}, k_q^{\text{VSI}}, k_q^{\text{SG}}, k_\omega^{\text{SG}}) \cdot \sum_{i=1}^4 Y_i \\ & \omega_n \in \Omega_N \end{aligned}$$

The optimization problem is formulated in Matlab using Yalmip [58], and solved with Mosek [59]. The algorithm converges within 8 iterations, which takes less than 5 minutes on a standard desktop computer in our simple implementation. The achieved maximum singular values of the sensitivity of the original droop controller and the new controller are shown in Fig. 5.9. It can be seen that the 20 dB resonance peak in the SG sensitivity has been successfully attenuated.

Simulation Results

To validate the performance, the grid is simulated in Simulink using the Simpower toolbox, and the performance of the new controller is compared with the original droop controller. In Fig. 5.10a the evolution of the frequency of the generators is shown after the active power load at bus 3 is stepped up by 70 kW at $t = 1$ s. The improved primary controller reduces the settling time from 0.8 s to 0.2 s. The plots also show that the ringing is successfully damped.

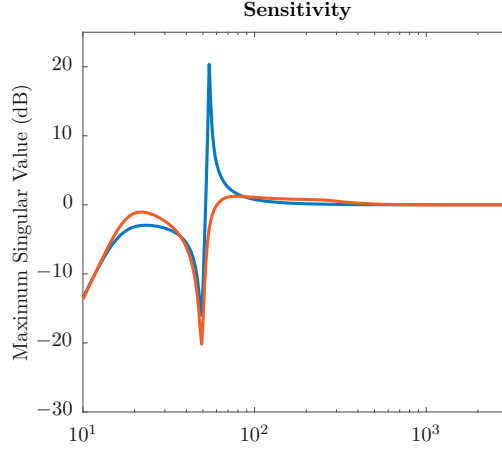


Figure 5.9 – Maximum singular value plots of the SG sensitivity W_1S . Blue is the droop controller, red is the new controller.

The active and reactive output power of the generators is shown in Figs. 5.10b and 5.11. It is interesting to note that with droop control, the active power load step also introduces significant ringing in the reactive output power of the generators. This is due to the R/X ratio of the lines being greater than 1, which introduces a coupling between the generator frequency and reactive output power. The settling time is again significantly improved with the new controller, and both transients are smoother with minimal ringing. It can also be seen that proportional active power sharing is maintained.

5.A.3 Robustness Towards Topology Change

For the second part of this example, the line between buses 9 and 10 is closed, leading to a change in topology. While the controller designed in Part 1 satisfies the desired performance specifications as long as the line is open, there is no guarantee of stability or performance when it is closed.

While the stability of the controller designed in Part 1 with line 9-10 closed could be determined a posteriori, a preferable approach is to directly consider both models during the design process. This can be done by introducing a multimodel uncertainty to the control design problem, as described in Section 2.6.3.

First, G_{comp} is formed for line 9-10 open and closed respectively. The optimization problem in Eq. (5.41) is then solved for the multimodel case, using the same performance specifications and initial controller. The performance of the resulting controller after closing line 9-10 is evaluated in simulation. The frequency of the generation units after line 9-10 is closed at $t = 1$ s is shown in Fig. 5.12 both for the multimodel controller and the original droop controller. It can be seen that the settling times of the frequency transients are significantly reduced by the multimodel controller. Also, stability and

5.A. Primary and Secondary Control Design: Additional Results

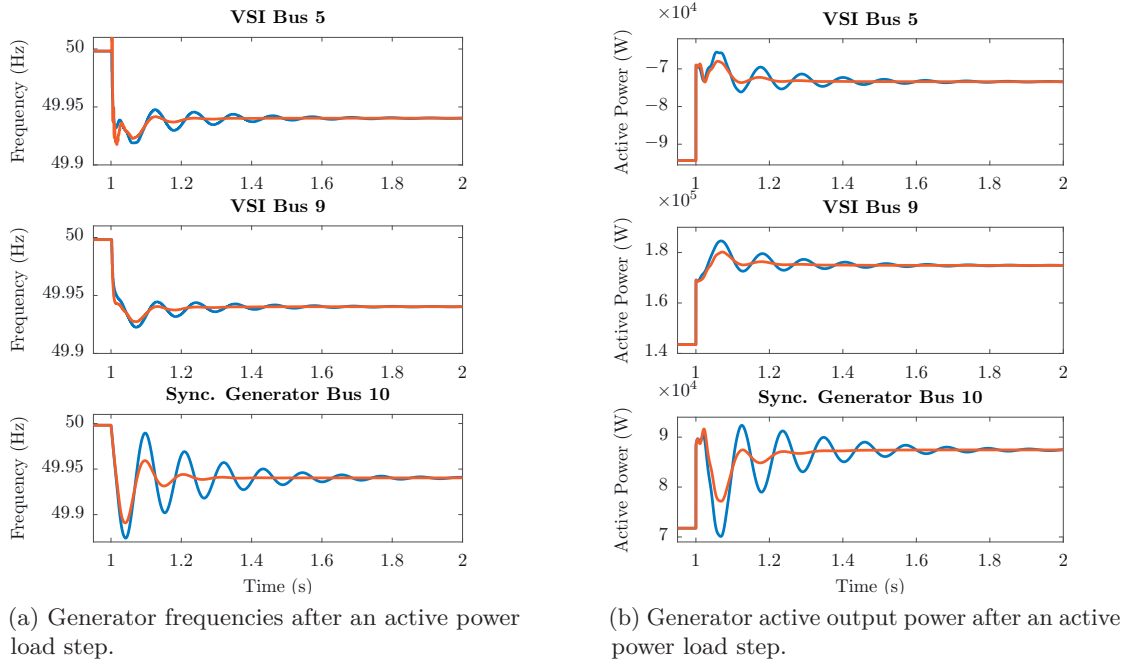


Figure 5.10 – Comparison of simulation results. Blue is the droop controller, red is the new primary controller

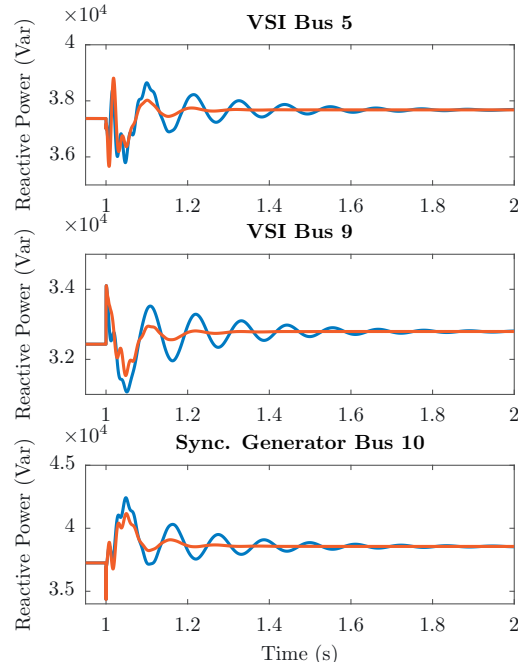


Figure 5.11 – Generator reactive output power after an active power load step. Blue is the droop controller, red is the new primary controller.

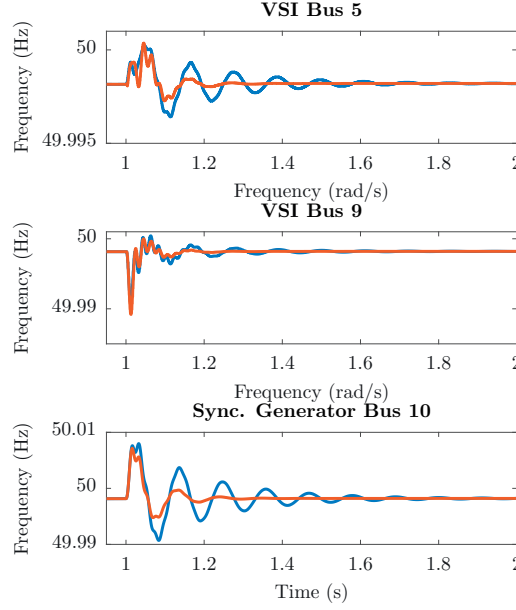


Figure 5.12 – Generator frequency after line 9-10 is closed. Blue is the droop controller, red is the new primary controller.

performance are guaranteed for both topologies by design.

5.A.4 Distributed Secondary Control

While the controllers designed in the previous sections improve the transient performance, as can be seen in Fig. 5.10a the lack of integral action still introduces a significant steady-state error in the frequency after a load change. The simplest solution for this issue would be to add decentralized integrators to the controller of each generation unit, which would not require any additional communication lines. However, in practice this approach is not feasible, as any bias in the measurements or control inputs would render the system unstable. Therefore, the controller structure is augmented with a distributed part that fulfills the task of traditional centralized secondary frequency control, but at a significantly higher bandwidth. In [113] a distributed integral control scheme is proposed that adjusts the active power setpoints of the generation units in order to eliminate the frequency error. However, no method to tune the controller gains is given. The presented control design method will be used to calculate the gains such that the integral action achieves a desired bandwidth, while guaranteeing closed-loop stability and performance. It is important to point out that the ability of our method to directly design discrete-time controllers is critical in this example. Whereas the continuous-time formulation of the distributed integral controller is stable for any choice of positive controller gains, in discrete-time decreasing the gains leads to a degradation of transient performance, and eventually instability. Therefore, being able to design the controller

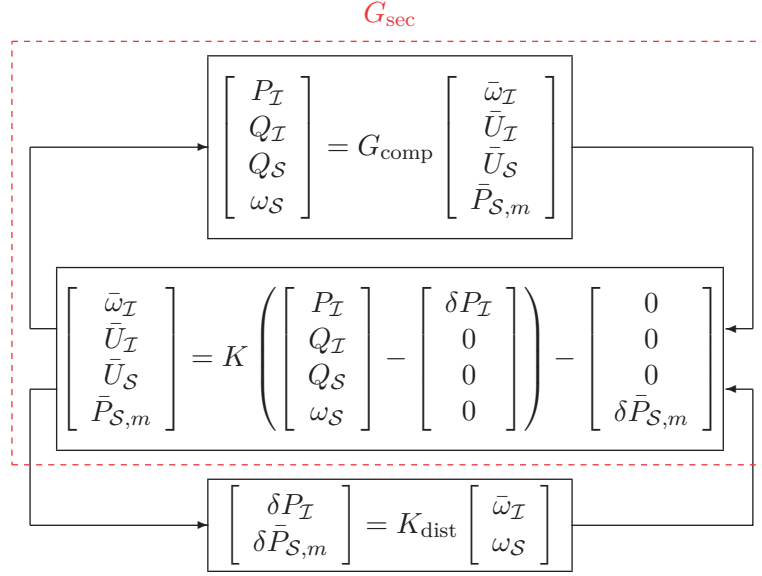


Figure 5.13 – Block diagram of the distributed secondary controller.

directly in discrete-time is a significant advantage.

According to [113], the distributed integral controller has the following dynamics:

$$\begin{aligned}
 K_I \begin{bmatrix} \delta \dot{P}_I \\ \delta \dot{P}_{S,m} \end{bmatrix} &= K_P^{-1} \begin{bmatrix} \bar{\omega}_I \\ \omega_S \end{bmatrix} - L_c K_P \begin{bmatrix} \delta P_I \\ \delta \bar{P}_{S,m} \end{bmatrix} \\
 K_P &= \text{diag}(k_p^{\text{VSI}}, (k_\omega^{\text{SG}})^{-1})
 \end{aligned} \tag{5.42}$$

where K_I is a diagonal matrix containing the integral gains, $\delta P_I, \delta \bar{P}_{S,m}$ are adjustments of the active power setpoints of the VSIs and SG, and L_c is the Laplacian matrix of the communication graph. For this example, a non-full graph is assumed, where the generators at bus 5 and 10 are able to communicate with the generator at bus 9, but not directly with each other. By using the backward Euler transformation, the controller can be rewritten as a discrete-time transfer function with a sampling time $T_s = 1$ ms:

$$\begin{aligned}
 \begin{bmatrix} \delta P_I \\ \delta \bar{P}_{S,m} \end{bmatrix} &= K_{\text{dist}} \begin{bmatrix} \bar{\omega}_I \\ \omega_S \end{bmatrix} \\
 K_{\text{dist}} &= T_s (K_P K_I z + (K_P L_c K_P - K_P K_I))^{-1}
 \end{aligned} \tag{5.43}$$

In this form, the controller can now be easily written in the form $K_{\text{dist}} = XY^{-1}$. The block diagram of the augmented system is shown in Fig. 5.13, where K is the improved primary controller calculated in Part 2 of this example.

Performance Specifications

In order to design the gains K_I according to classical performance specifications, we need to formulate the plant G_{sec} . First, we define the following four sensitivity functions:

$$\begin{aligned} S_{11} &= K(I + KG_{\text{comp}})^{-1} & S_{12} &= (I + KG_{\text{comp}})^{-1} \\ S_{21} &= (I + G_{\text{comp}}K)^{-1} & S_{22} &= G_{\text{comp}}(I + G_{\text{comp}}K)^{-1} \end{aligned}$$

Using these sensitivity functions, we can formulate the plant as follows:

$$\begin{bmatrix} \bar{\omega}_{\mathcal{I}} \\ \omega_{\mathcal{S}} \end{bmatrix} = G_{\text{sec}} \begin{bmatrix} \delta P_{\mathcal{I}} \\ \delta \bar{P}_{\mathcal{S},m} \end{bmatrix} = \begin{bmatrix} G_{\text{sec}}^{11} & G_{\text{sec}}^{12} \\ G_{\text{sec}}^{21} & G_{\text{sec}}^{22} \end{bmatrix} \begin{bmatrix} \delta P_{\mathcal{I}} \\ \delta \bar{P}_{\mathcal{S},m} \end{bmatrix} \quad (5.44)$$

with

$$\begin{aligned} G_{\text{sec}}^{11} &= S_{11}^{\delta P_{\mathcal{I}} \rightarrow \bar{\omega}_{\mathcal{I}}} & G_{\text{sec}}^{12} &= S_{12}^{\delta \bar{P}_{\mathcal{S},m} \rightarrow \bar{\omega}_{\mathcal{I}}} \\ G_{\text{sec}}^{21} &= S_{21}^{\delta P_{\mathcal{I}} \rightarrow \omega_{\mathcal{S}}} & G_{\text{sec}}^{22} &= S_{22}^{\delta \bar{P}_{\mathcal{S},m} \rightarrow \omega_{\mathcal{S}}} \end{aligned}$$

A straightforward choice for the controller structure is:

$$X = I, \quad Y = K_{\text{dist}}^{-1} \quad (5.45)$$

where Y is linear in K_I . As a design objective, the gains in K_I are minimized. As (5.43) depends on the inverse of K_I , this in turn maximizes the bandwidth of the integral action. Additionally, a constraint on the weighted sensitivity is introduced to maintain a smooth transient:

$$\|W_1 S\|_{\infty} < 1, \quad W_1 = 0.2I \quad (5.46)$$

with $S = (I + G_{\text{sec}}K_{\text{dist}})^{-1}$. The initial controller is formed with $K_I = \text{diag}(10^3, 10^3, 10^3)$, which leads to a stabilizing controller with a very low bandwidth. The problem is sampled using 600 logarithmically-spaced frequency points in the interval $\Omega_N = \{1, 10^3\pi\}$ rad/s where the upper limit is the Nyquist frequency of the controller. The resulting convex

optimization problem is as follows:

$$\begin{aligned}
 & \min_{K_I} \gamma & (5.47) \\
 & \text{subject to:} \\
 & K_I < \gamma I \\
 & \begin{bmatrix} P^*P_c + P_c^*P - P_c^*P_c & (W_1Y)^* \\ W_1Y & \gamma I \end{bmatrix} (j\omega_n) > 0 \\
 & [Y_c^*Y + Y^*Y_c - Y_c^*Y_c] (j\omega_n) > 0 \\
 & \omega_n \in \Omega_N
 \end{aligned}$$

Simulation Results

As before, the resulting controller is evaluated in Simulink using the Simpower toolbox. In Fig. 5.14a a comparison of the evolution of frequency of the generators is shown after the active power load at bus 3 is stepped up by 47.5 kW at $t = 1$ s. With the addition of the distributed secondary controller, it can be seen that the frequency is returned to the nominal value within 1 s and with no overshoot. The transient response of the droop and improved primary controller are also plotted for comparison, showing that the settling time of the latter is similar to that of the distributed controller.

The active output power of the generators is shown in Fig. 5.14b. With the chosen performance constraints, the transients for the distributed controller are smooth with minimal ringing, but the output power takes longer to settle at the new steady-state than with the improved primary controller.

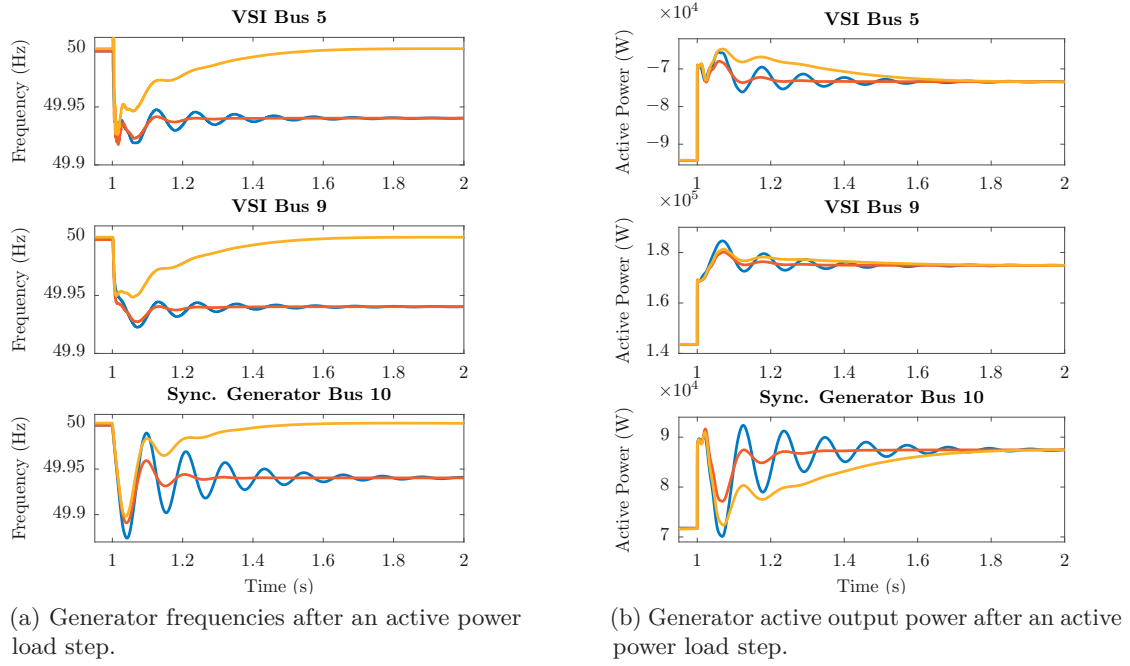


Figure 5.14 – Comparison of simulation results for secondary control. Blue is the droop controller, red is the improved primary controller, yellow is with the distributed controller.

6 Conclusion

6.1 Summary

In this thesis, a novel fixed-structure control design method for multivariable systems based on frequency-domain data and convex optimization was developed. The main advantages of the control design method can be summarized as follows:

- Only the frequency response of the plant is required for the design. The order of the model has little effect on the computational complexity of approach. It is also possible to directly use the measured frequency response for the design, thus enabling a data-driven approach where no parametric model is required.
- H_∞ and H_2 performance constraints on any loop transfer function can be considered, which allows for a much wider range of design specifications than many other approaches.
- The method is convex, and the solution converges to a locally optimal solution of the original non-convex problem.
- Since the design relies only on frequency-domain data, discrete-time controllers can be designed for continuous-time plants (and vice versa). Most other methods can only be used to design continuous-time controllers, and a discretization step is required. However, properly discretizing a controller is often challenging, and performance can be lost. By directly designing in discrete-time, these problems are avoided.
- Controllers are fully parametrized, as opposed to most frequency-data-based methods in the literature that rely on linearly parametrized controllers, which allows to achieve better performance. The structure is very general and covers most representations.

The method was employed to tackle challenging and relevant problems in present-day and future power systems. Two complex and relevant case studies show how difficult control problems in power systems can be solved using the new method.

The first example treats the problem of current control design for parallel grid-connected inverters. A methodical and rigorous controller synthesis procedure is proposed that presents a notable improvement over existing methods in the field. Performance specifications such as desired bandwidth, decoupling and robustness are directly formulated as design objectives. Whereas most other approaches for the tuning of current controllers rely on an iterative procedure, where stability and performance are evaluated a posteriori, the optimization-based approach is able to compute a controller that guarantees stability and performance by design. It also allows to implement higher order and multivariable controllers that would be very challenging to tune manually. The result is a design process that is much faster and at the same time achieves better performance than classical methods.

The second example demonstrates the design of a distributed controller that is able to provide primary and secondary frequency and voltage control in a unified framework. It is shown how non-standard performance specifications such as proportional power sharing, no frequency steady-state error and decoupling can be formulated as frequency-domain constraints on closed-loop sensitivity functions. A generic problem formulation is presented that is able to accommodate any number of inverters and synchronous generators, and makes no assumption on the grid structure and line parameters. The result is a new architecture that allows the abolishment of the classical hierarchical separation of primary and secondary control, and opens a new perspective on distributed control design in power systems.

The thesis highlights some of the issues introduced by large-scale distributed generation, but it also shows how control design methods are a crucial piece of the puzzle that is the future power grid. The author hopes that it is able to impart some fundamental concepts of power systems to control engineers, and on the other hand demonstrate to power engineers the possibilities of modern control design methods. The formulation of power system performance specifications in a frequency-domain framework has proven to be very versatile and powerful, and provides a timeless and generic architecture that enables the application of a large range of advanced methods now and in the future.

6.2 Future Research

Control Design Method

While the developed control design method covers a wide range of applications, there are several possible extensions that would be worthwhile to pursue. An important issue is

the numerically robust implementation of the convex optimization. While the algorithm performs well in many cases, numerical problems can occur, especially when designing controllers with poles and zeros close to the stability boundary. This is relevant for various applications such as the compensation of mechanical couplings, or the design of notch filters. Other interesting extensions are the design of gain-scheduled controllers, and the design of state-space controllers.

Power Systems Modeling

The proposed frequency-domain modeling approach offers a powerful and flexible framework, but the generator and load models considered in this thesis are still relatively simplistic. Implementing more complex models would be an obvious next step to achieve even more realistic simulations. Another very important aspect that is often not true in real distribution grids is the assumption of balanced voltages and currents. Extending the model to represent unbalanced conditions would enable the design of controllers specifically for these situations, which is still rarely treated in the literature.

Distributed Primary and Secondary Control

The formulation of distributed primary and secondary control design as a robust control problem as proposed in Chapter 5 presents a strong basis for many challenging and relevant research topics. A straightforward next step would be to consider more realistic generator and load models, and to develop appropriate performance specifications. A very crucial aspect that is often not considered is the primary source side of an inverter. Designing controllers that take into account things such as curtailing of photovoltaics, inertia of wind turbines or maximum power rates of batteries would be an important step towards realisability.

Another aspect concerns distributed architectures and related issues such as robustness towards communication loss and time delays. From an economic perspective, the control design method could also be used to assess different layouts of communication networks in order to make an informed decision about the tradeoff between the performance and number of communication lines.

Data-Driven Control in Power Systems

A very promising and interesting feature is the potential for data-driven control design. The frequency-domain model developed in this thesis forms a solid basis for the validation of data-driven models derived from measurement data. With the increasing availability of phasor measurement units and similar devices, data-driven design becomes an attractive approach that would make it possible to avoid many of the issues related to first-principle

models. The data-driven approach is also very promising in the light of plug-and-play design for distributed generation units, enabling a holistic approach where the measured frequency response is used to design a robust controller on-site, and without requiring any knowledge of the rest of the grid.

A Data-Driven Control Design for Atomic-Force Microscopy¹

In this chapter the control design method from Chapter 2 is used to design data-driven controllers for atomic-force microscopes (AFMs).

A.1 System Description

An AFM is a mechanical microscope with a resolution on the order of nanometers, and a wide range of applications in various fields such as solid-state physics [138], semiconductor science [139], molecular biology [140, 141] and cell biology [142–144]. The basic functionality of the AFM is shown in Fig. A.1 [140]. The main sensor is a cantilever with a sharp tip that is used to probe the surface of the sample to be studied. The deflection of the cantilever can be measured using a laser that is reflected off its back and

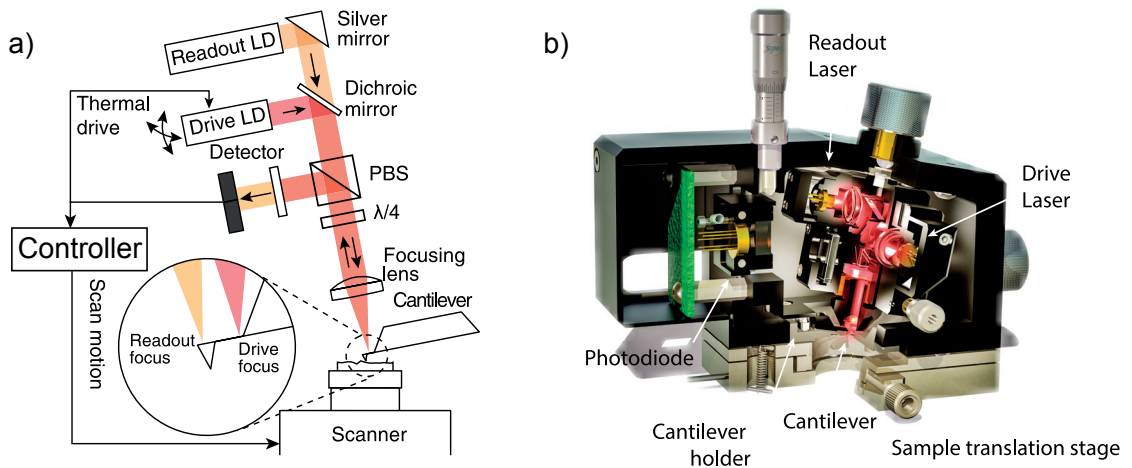


Figure A.1 – a) Block diagram of the functionality of an AFM. b) Exploded view of the head used for the experiments.

¹I would like to thank Adrian Nievergelt, Prof. Georg Fantner and the whole of the LBNI group at EPFL for their collaboration, and for making this work possible.

Appendix A. Data-Driven Control Design for Atomic-Force Microscopy

collected by a photodetector. From this measurement, the tip-sample interaction force can be extracted, which yields information about various mechanical material properties. Furthermore, the measured deflection is used to control a piezo actuator that moves the vertical position of the sample up and down in order to keep the deflection at a controlled value. Another piezo actuator is used to move the sample in the horizontal plane, and by scanning the sample in a raster an image is acquired point by point.

As the deflection of the piezo is proportional to the applied voltage, the image can be reconstructed from the input signal that is extracted from the feedback loop. This also means that the tracking performance of controller used to regulate the piezo actuator plays a crucial role in determining the quality of the image. Ringing in the closed-loop response leads to visible ripples and distortions in the AFM image, and good disturbance rejection is important. Furthermore, the image is acquired line by line as the scanner moves back and forth in the horizontal direction. The relevant metric for the speed is the line rate, which indicates the number of lines per second (L/s) that are recorded. As the scanning motion translates the spatial frequencies of the surface into temporal frequencies, the maximum line rate (and therefore the time required to record an image) directly depends on the closed-loop bandwidth. Simply put, the controller has to be able to track any features of the sample fast enough. A too slow controller leads to distortions in the image, blurs out the features and creates artifacts that obscure the true image.

Increasing the number of images that can be recorded in a given time enables the observation of processes on the nanoscale in real-time, which is of great interest to many fields. Fast scanning speeds make it possible to record time-lapse image series of processes that could not be observed before. Also, a high controller bandwidth reduces feedback-error-induced force interactions between the tip and the sample, which improves the image quality.

A.2 State of the Art

The standard control approach in AFM consists of a PI-controller in series with a low-pass filter, where the controller gains are manually tuned by the operator [145]. With this approach, a scanner's control bandwidth is mainly limited by the excitation of the first mechanical resonance. Too high controller gains degrade the reference tracking performance and introduce ringing, which introduces visible ripples in the AFM image. Nonetheless, being easy to implement and straightforward to tune, the PI remains the most prevalent controller in practice.

Several methods to improve the performance have been published in the literature. A common approach is to obtain a parametric plant model (from first principles or through system identification) and use its inverse in series with an integrator as a controller [146–151]. To achieve stability, additional filters are added and tuned manually, which can be a

lengthy process that requires solid knowledge of control systems. The final controllers are generally not robust towards modeling uncertainties, and performance is not guaranteed. In [152] a data-driven approach is proposed, where based on the frequency response of the plant an optimization problem is solved to calculate the frequency response of a stabilizing controller. Then, a continuous-time controller is fitted to the result using the Matlab system identification toolbox.

A common limitation of the approaches discussed so far is that they are generally not robust towards modeling uncertainties, and are therefore mostly applied to samples in air, where the dynamics of the system generally don't change in the timeframe of imaging. However, in order to study e.g. biological processes, the AFM has to be operated in liquid. This causes a problem for classical approaches, as in liquid the frequency response changes significantly every time an experiment is set up, which makes obtaining an accurate plant model challenging. First-principle models are nigh impossible to derive due to the complicated dynamics introduced by the interactions between the liquid and the scanner. Further complications when imaging in liquid are that air bubbles can form spontaneously, that the tip accumulates dirt more easily, and that the liquid dries up over time, all of which cause the response of the plant to change over time. Since experiments often involve taking images in fixed intervals over several hours, frequent re-identification of the plant and recalculation of the controller is necessary, which makes an automated and robust design process a necessity. While standard H_∞ control design techniques have been applied in the literature [153, 154], they have met with limited success. Drawbacks are that still a parametric model is required, and often some user interaction is necessary to choose the correct design parameters. Since AFM practitioners generally do not have an in-depth knowledge of control systems, up to now advanced techniques have proven to be too unwieldy for day-to-day operations.

Using a data-driven approach, the frequency response of any scanner can be calculated within a few seconds directly before capturing an image. Furthermore, as opposed to identifying a parametric model, the calculation of the frequency response is significantly simpler, and does not require an expert to adjust the identification parameters. Similarly, by using an optimization-based approach to tune the controller, no user interaction is required for the design, which again drastically reduces the preparation time. Directly computing a discrete-time controller also makes the discretization step unnecessary, which further simplifies the design process. Figure A.2 gives an overview of the differences in the design process between classical methods and our method, and illustrates the simplicity of the proposed approach.

In its final form, the control design algorithm has been embedded within the standard Labview interface that is used to run the system. With 3 button presses an operator can identify a response and design a controller within a few minutes, and without requiring any knowledge of control systems. This results in a useful and accessible tool that is now regularly used by practitioners.

Appendix A. Data-Driven Control Design for Atomic-Force Microscopy

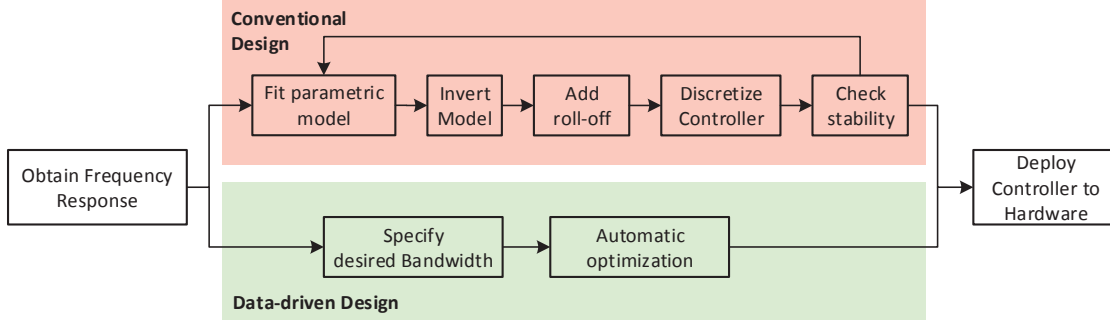


Figure A.2 – Comparison of control design steps in AFM for conventional approaches and using a data-driven approach.

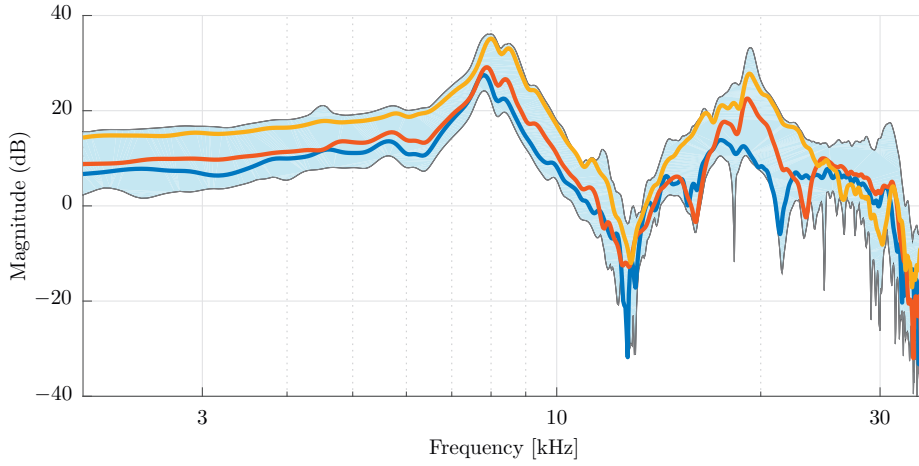


Figure A.3 – Evolution of the frequency response of a J-scanner in liquid over 3 hours. The envelope shows the range of the variations. Three example responses are shown, where blue is at the start, red is after 1 hour and yellow is after 2 hours.

A.3 Control Design

A.3.1 Plant Identification

This section considers the control design in the lateral axis. The input of the plant corresponds to the voltage applied to the piezo actuator, and the output corresponds to the deflection of the cantilever (see Fig. A.1). Both signals are within a range of ± 10 V. The system is excited by applying 100 periods of a pseudorandom binary sequence (PRBS) with a length of 8191 samples and a sampling frequency depending on the bandwidth of the system. The frequency response is calculated in Matlab using the *spa* command with a Hann window length of 700. Figure A.3 shows an example of the evolution of the frequency response over time. The change in the response can be significant, with magnitudes changing by 10 dB or more, and resonance peaks appearing and disappearing over time.

A.3.2 Control Performance

The objective is to achieve good tracking performance of the reference input. This is achieved through loop shaping, where a controller is designed such that the loop transfer function $L = GK$ is close to a desired transfer function L_d :

$$\min_K \|L - L_d\|_2, \quad L_d = \frac{\omega_c}{s} \quad (\text{A.1})$$

where ω_c is the desired bandwidth of the system.

To improve the robustness, H_∞ constraints on the closed-loop sensitivity $T = GK(I + GK)^{-1}$ and the input sensitivity $U = K(I + GK)^{-1}$ are introduced:

$$\|W_2 T\|_\infty < 1 \quad ; \quad \|W_3 U\|_\infty < 1 \quad (\text{A.2})$$

where W_2, W_3 are chosen as:

$$W_2^{-1} = 1.2B(1.1\omega_c), \quad W_3^{-1} = \begin{cases} 10G(0)B(1.1\omega_c) & \forall \omega \leq \omega_c \\ G(0)B(1.1\omega_c) & \forall \omega > \omega_c \end{cases} \quad (\text{A.3})$$

where $B(\omega_c)$ is a second-order discrete-time Butterworth lowpass filter with a cutoff frequency of ω_c . In order to have a generic formulation, the input filter W_3 is scaled by the dc-gain of the plant $G(0)$. This choice of filters enforces a roll-off in the closed-loop and input sensitivities, which improves the robustness of the controller towards plant uncertainties at frequencies above the desired bandwidth.

This leads to the following robust control design problem:

$$\min_K \|L - L_d\|_2 \quad (\text{A.4})$$

subject to:

$$\|W_2 T\|_\infty < 1$$

$$\|W_3 U\|_\infty < 1$$

A.3.3 Controller Structure

A 10th-order discrete-time transfer function controller K with fixed integrator is designed:

$$K = X(z)Y(z)^{-1} = \frac{x_{10}z^{10} + \dots + x_1z + x_0}{(z^{10} + \dots + y_1z + y_0)(z - 1)} \quad (\text{A.5})$$

where $x_i, y_i \in \mathbb{R}$ are the tunable parameters. This choice of order has been found to be sufficient for the systems the method was applied to.

A.3.4 Convex Formulation

To solve the robust design problem, a frequency grid with $N = 500$ logarithmically-spaced frequency points in the interval $\Omega_N = \left\{0.01 \frac{\pi}{T_s}, \frac{\pi}{T_s}\right\}$ rad/s is chosen, where the upper limit is the Nyquist frequency of the controller. Since the plants are always stable, an integral controller with low gain is chosen as initial controller:

$$K_c = X_c Y_c^{-1} = 10^{-3} \frac{z^{10}}{z^{10}(z-1)} \quad (\text{A.6})$$

where the order is augmented to satisfy the conditions of the design algorithm on the order of the initial controller.

Then, as described in Chapter 2, the control design problem is reformulated as a convex optimization problem:

$$\min_{X,Y} \sum_{k=1}^N \text{trace}[\Gamma_k] \quad (\text{A.7})$$

subject to:

$$\begin{aligned} & \begin{bmatrix} Y^* Y_c + Y_c^* Y - Y_c^* Y_c & (GX - L_d Y)^* \\ GX - L_d Y & \Gamma_k \end{bmatrix} (j\omega_k) > 0 \\ & \begin{bmatrix} P^* P_c + P_c^* P - P_c^* P_c & (W_2 GX)^* \\ W_2 GX & I \end{bmatrix} (j\omega_k) > 0 \\ & \begin{bmatrix} P^* P_c + P_c^* P - P_c^* P_c & (W_3 X)^* \\ W_3 X & I \end{bmatrix} (j\omega_k) > 0 \\ & k = 1, \dots, N \end{aligned}$$

The optimization problem is implemented in Matlab using Yalmip [58], and solved with Mosek [59]. The time to compute a controller is around 1 minute, and since the design is in discrete-time the controller parameters are directly written to the real-time software without requiring any user interaction.

A comparison of the obtained performance of the standard PI controller and the 10th-order controller is shown in Fig. A.4. It can be seen in subfigure A.4c) that the bandwidth of the 10th-order controller exceeds the PI by about one order of magnitude. At the same time, the resonance peak in the closed-loop sensitivity function is removed, which also leads to less ringing and better tracking performance.

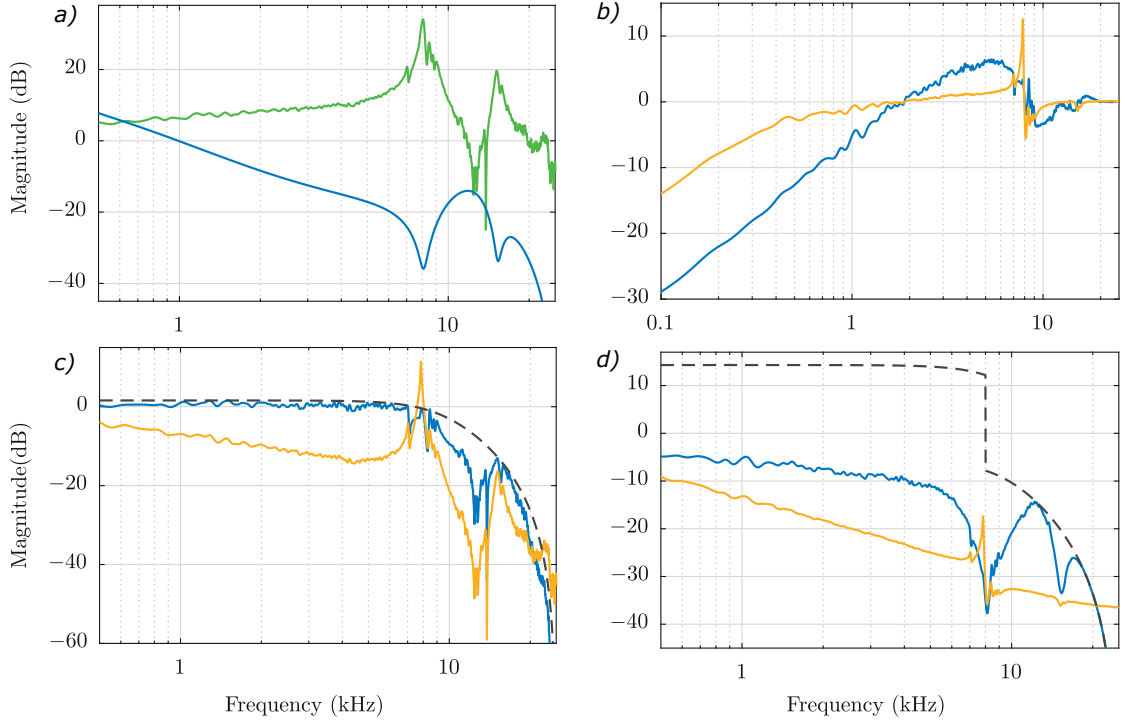


Figure A.4 – Comparison of the nominal closed-loop sensitivities. a) Measured plant frequency response in green, designed 10th-order controller in blue. b)-d) Sensitivity S , closed-loop sensitivity T and input sensitivity U for the 10th-order controller in blue and the PI-controller in yellow. Black dashed lines indicate the constraints W_2, W_3 .

A.4 Experimental Results

To validate the performance of the designed controllers, the approach is tested on several scanners and in different environments. The results for four setups are shown in Fig. A.5. It can be seen that the nominal and measured closed-loop responses match very well, and that the desired roll-off is achieved. The chosen performance specifications provide good results for all cases, which proves that the same algorithm can be applied to different systems without requiring any user interaction. It is also interesting to note that several of the designed controllers seem to defy expectations in that they do not at all resemble the inverse of the plant, which goes against the classical design approaches.

To show the superior imaging capabilities of the controller, an E-scanner is used to image DNA at different speeds. A comparison of the images for increasing line rates are shown in Fig. A.6, where it can be seen that the features are preserved up to a speed of 220 L/s. To compare, using the standard PI controller, the limit is reached at around 40 L/s, with significantly worse quality.

As an applied example, in Fig. A.7 the time-lapse of a self-assembling DNA lattice is shown. In the process, individual strands of DNA bond together to form a superstructure consisting of hexagonal rings. Thanks to the superior performance of the 10th-order

Appendix A. Data-Driven Control Design for Atomic-Force Microscopy

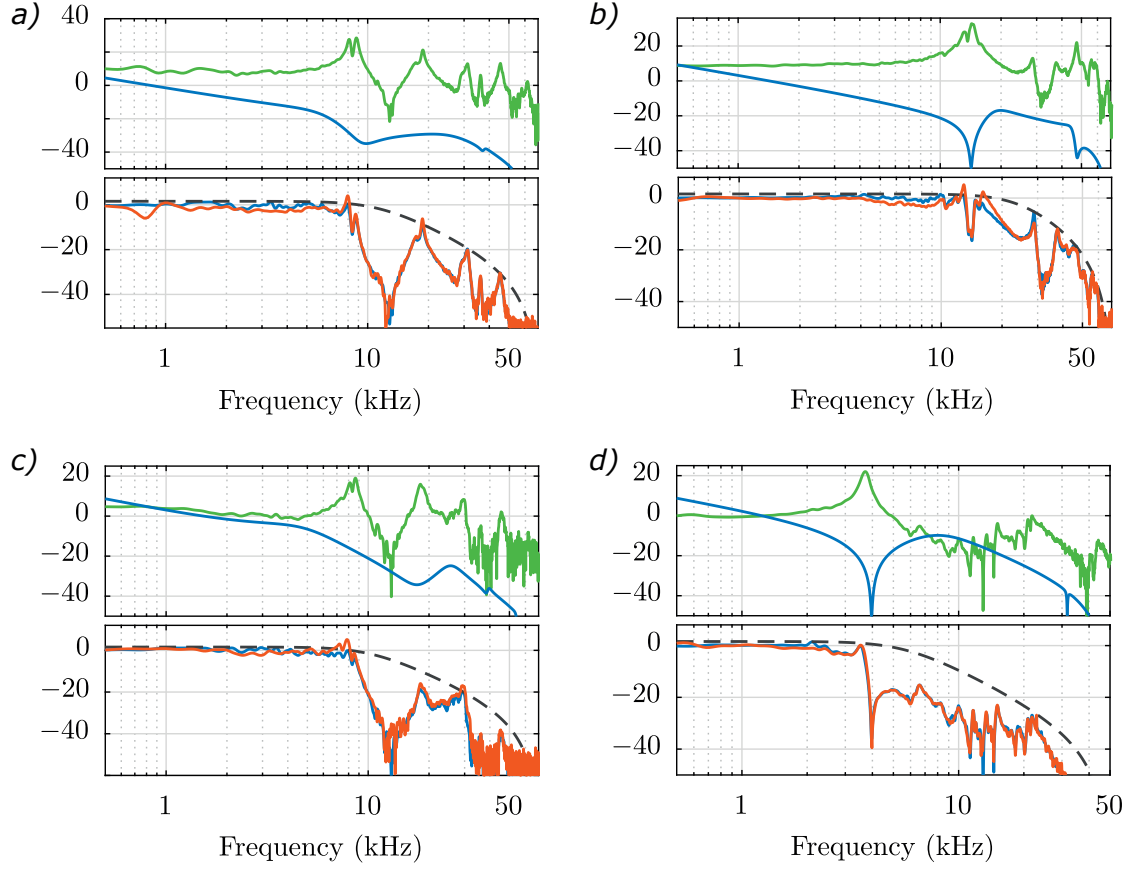


Figure A.5 – Frequency responses and designed controllers for different systems. The upper plots show the plant in green and the controller in blue. The lower plots show the nominal and measured closed-loop sensitivity in blue and red respectively, with the H_∞ constraint in dashed black. a) J-scanner in air, b) E-scanner in air, c) J-scanner in liquid, d) triple-S scanner in air.

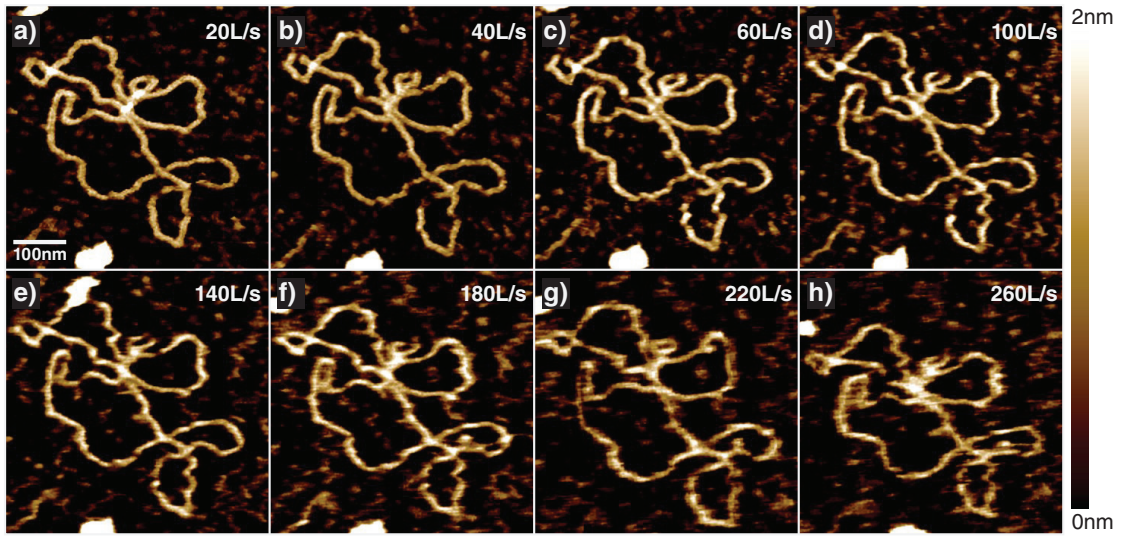


Figure A.6 – Imaging of DNA at increasing line rates.

controller it is possible to record more images in a given time, and at a higher quality than with the PI controller. This makes it possible to get a detailed look at the intermediary stages of the process. The creation and dissolution of defective rings can be observed, and the precise formation of the structure can be studied.

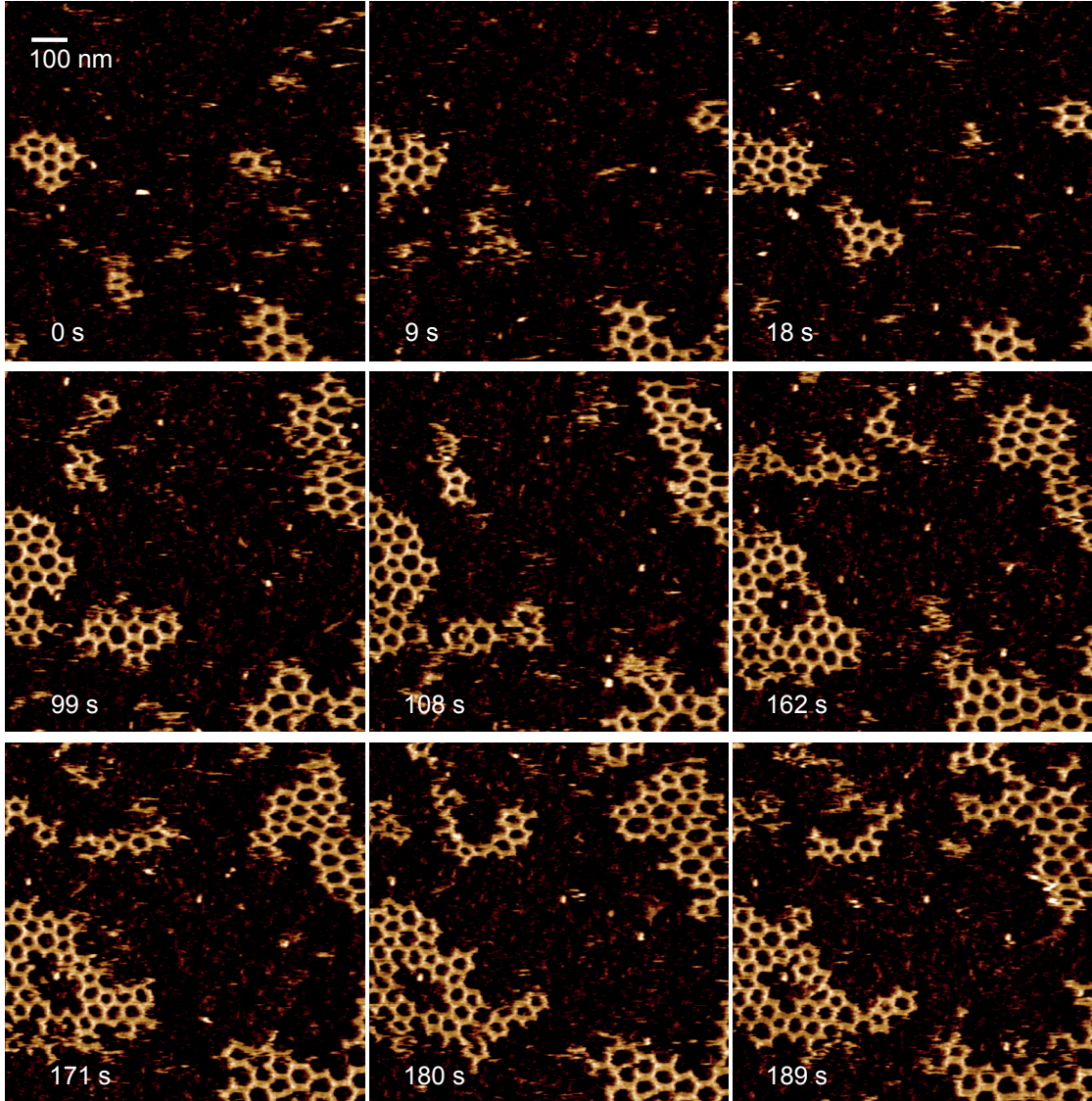


Figure A.7 – Time-lapse of the self-assembly of a DNA lattice.

A.5 Conclusion

The control design method developed in Chapter 2 has been successfully applied in two data-driven settings, and experimental results have verified the potential and versatility of the approach. The control of a 2-DOF gyroscope shows that the method is well suited for multivariable control design of strongly coupled systems under multimodel

Appendix A. Data-Driven Control Design for Atomic-Force Microscopy

uncertainty, which is a challenging and relevant problem in many practical applications.

Furthermore, the method forms the basis for a fully automated control design tool for atomic force microscopes that can be used regularly by practitioners with no background in control systems. The method has proven to be robust and reliable, and, based on generic design specifications, has been applied to a wide range of systems. The combination of data-driven design, convex optimization and being able to directly design discrete-time controllers results in a powerful algorithm that is able to overcome most limitations of classical approaches, and may well establish the future direction for control design for AFM.

B Data-driven Multivariable Control of a 2-DOF Gyroscope

This experimental example presents the design of a data-driven, robust multivariable controller with multimodel uncertainty to control the gimbal angles of a gyroscope. The controller is then applied on the experimental setup to validate the performance.

B.1 Experimental Setup

The experiment was conducted on a 3 DOF gyroscope setup built by Quanser (see Fig. B.1). The system consists of a disk mounted inside an inner blue gimbal, which is in turn mounted inside an outer red gimbal. The entire structure is supported by the rectangular silver frame. The disk, both gimbals and the frame can be actuated about their respective axis by electric motors, and their angular positions can be measured using high resolution optical encoders. For this experiment, the position of the silver frame is mechanically fixed in place. The control objective is to achieve a good tracking performance on the angular positions of the blue and red gimbal and to minimize the coupling between the axes. The dynamics of the system change depending on the angular velocity of the disk, which is included in the control design as a multimodel uncertainty.

B.2 Frequency Response

The gyroscope is a strongly nonlinear system, and linear control design methods only achieve good performance in a small range around the operation points. In order to improve this range, a cascaded control architecture was chosen, with a feedback linearization forming the inner loop. The block diagram in Fig. B.2 shows the structure of the system, where G_m is the real plant and K_{fl} is the feedback linearization controller. The closed-loop response of the inner loop is taken as the new plant G , which is used to design the outer controller K .

The variables $\theta = [\theta_b, \theta_r]^T$ and $\theta^* = [\theta_b^*, \theta_r^*]^T$ are vectors containing the measured and

Appendix B. Data-driven Multivariable Control of a 2-DOF Gyroscope



Figure B.1 – The gyroscope experimental setup by Quanser.

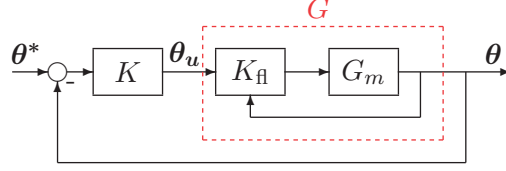


Figure B.2 – Block diagram of the cascaded controller structure of the gyroscope.

desired blue and red gimbal angles, and $\theta_u = [\theta_{ub}, \theta_{ur}]^T$ are the reference gimbal angles given to the feedback linearization.

The black box model G therefore has 2 inputs and 2 outputs, and a single-channel excitation is applied to calculate the frequency response of G . A PRBS signal with an amplitude of $\pm 10^\circ$, a length of 511 samples and a sampling time of 20 ms was applied for 4 periods to θ_{ub} and θ_{ur} respectively. The non-excited input was set to zero during the process. The frequency response was calculated in Matlab using the *spa* command with a Hann window length of 150. The frequency response was measured for the three different disk velocities $v = [300, 400, 500]$ rpm, resulting in three models $\mathcal{G} = [G_1, G_2, G_3]$. The frequency responses are shown in Fig. B.3. It can be seen that the coupling and resonance modes become stronger at higher disk speeds.

B.3 Control Design Formulation

Based on the three frequency responses, a multivariable controller is designed. The goal is to decouple the system while also achieving good tracking performance of the reference angles θ^* . Therefore, as objective function we choose to minimize the 2-norm $\|L - L_d\|_2$ between the actual open-loop transfer function L and desired open-loop transfer function $L_d = \frac{\omega_c}{s} I$, where a bandwidth of $\omega_c = 4$ rad/s is desired for the decoupled system.

To limit the overshoot and guarantee a good roll-off at higher frequencies, an additional H_∞ constraint is put on the complementary sensitivity function:

$$\|W_2 T\|_\infty < 1, \quad W_2(j\omega) = \frac{j\omega + 6.5}{1.05 \cdot 6.5} I \quad (\text{B.1})$$

where W_2^{-1} has the form of a low-pass filter to ensure a roll-off at high frequencies. The

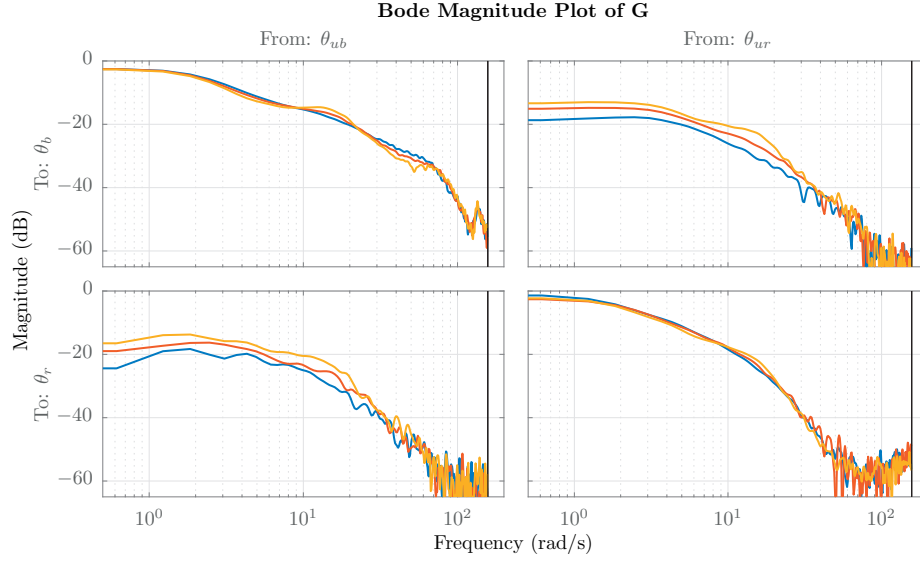


Figure B.3 – The measured frequency response of the blackbox model G at different disk speeds. The blue line is the response at a disk speed of 300 rpm, red at 400 rpm and yellow at 500 rpm.

fact that W_2 is not proper does not create any problem in practice because the constraints are evaluated only for finite values of ω . To prevent input saturation, a constraint on the input sensitivity is included:

$$\|W_3 U\|_\infty < 1, \quad W_3 = 0.05I \quad (\text{B.2})$$

where the magnitude of the weighting filter is chosen based on the expected worst-case disturbance.

A 5th-order discrete-time controller with a fixed integrator and a sampling time $T_s = 0.04$ s is chosen. This leads to the following structure:

$$\begin{aligned} X &= X_4 z^4 + X_3 z^3 + X_2 z^2 + X_1 z + X_0 \\ Y &= (I z^4 + Y_3 z^3 + Y_2 z^2 + Y_1 z + Y_0) \circ (z - 1)I \end{aligned} \quad (\text{B.3})$$

where $X_i \in \mathbb{R}^{2 \times 2}$ is a full matrix and $Y_i \in \mathbb{R}^{2 \times 2}$ is a diagonal matrix (i.e. the off-diagonal elements are fixed to zero). Fixing the structure of Y to be diagonal is useful in practice, as it greatly simplifies the calculation of the inverse and preserves the order of the controller. Note that the desired L_d and the weighting filters can be in continuous-time, while the designed controller is in discrete-time.

The optimization problem is sampled using $N = 500$ frequency points in the interval $\Omega_N = [10^{-1}, 25\pi]$ (the upper limit being the Nyquist frequency of the controller). The lower limit is chosen greater than zero in order to guarantee the boundedness of $L - L_d$.

Appendix B. Data-driven Multivariable Control of a 2-DOF Gyroscope

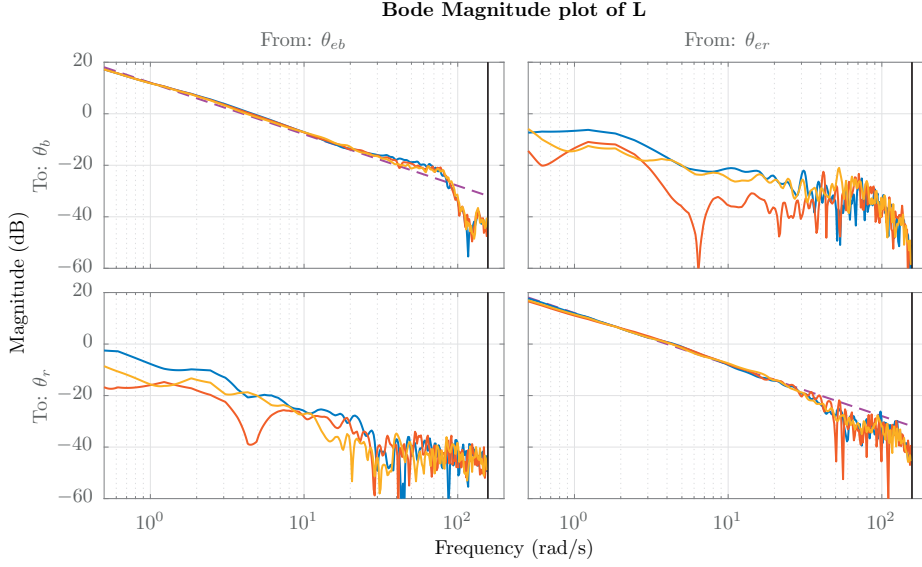


Figure B.4 – Bode magnitude plots of the desired open-loop transfer function L_d and the achieved $L_{1,2,3}$ for the three different plant models. The blue line is the achieved response at a disk speed of 300 rpm, red at 400 rpm and yellow at 500 rpm. The desired L_d is shown in dashed purple.

In fact a weighted two-norm of $L - L_d$ which is bounded is minimized.

The constraint sets are formulated for each of the three models $[G_1, G_2, G_3]$, resulting in the following optimization problem :

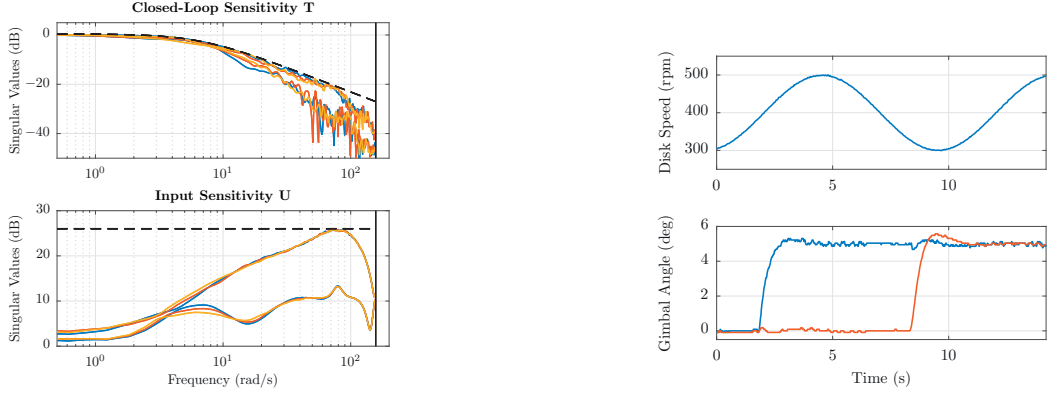
$$\min_{X,Y} \sum_{i=1}^3 \sum_{k=1}^N \text{trace}[\Gamma_{k_i}]$$

subject to:

$$\begin{aligned} & \begin{bmatrix} Y^* Y_c + Y_c^* Y - Y_c^* Y_c & (G_i X - L_d Y)^* \\ G_i X - L_d Y & \Gamma_{k_i} \end{bmatrix} (j\omega_k) > 0 \\ & \begin{bmatrix} P_i^* P_{c_i} + P_{c_i}^* P_i - P_{c_i}^* P_{c_i} & (W_2 G_i X)^* \\ W_2 G_i X & I \end{bmatrix} (j\omega_k) > 0 \\ & \begin{bmatrix} P_i^* P_{c_i} + P_{c_i}^* P_i - P_{c_i}^* P_{c_i} & (W_3 X)^* \\ W_3 X & I \end{bmatrix} (j\omega_k) > 0 \\ & k = 1, \dots, N \quad ; \quad i = 1, 2, 3 \end{aligned}$$

As the gyroscope is a stable system, the initial controller was chosen as an integral controller with low gain. Furthermore, the condition on the order of the initial controller is satisfied by augmenting it with the right number of poles and zeros at 0:

$$X_c = 0.01z^4 I \quad ; \quad Y_c = z^4(z - 1)I \quad (\text{B.4})$$



(a) Singular value plots of the nominal closed-loop and input sensitivity for the three different plants. The dashed lines indicate the constraints.

(b) Step response of the blue and red gimbal angles during a varying disk velocity.

Figure B.5 – Closed-loop sensitivities and measured step response.

It is important to note that Y_c has to contain an integrator to satisfy the first condition in Theorem 2 on the initial controller.

The optimization problem is implemented in Matlab using Yalmip [58], and solved with Mosek [59]. The iteration converges to a final controller in 10 steps. The bode magnitude plots of L_d and the obtained $L_{1,2,3}$ for the three different plant models are shown in Fig. B.4. It can be seen that the designed controller approximates the desired loop shape well at low frequencies, and that the system is well decoupled. The singular value plots of the obtained closed-loop and input sensitivity are displayed in Fig. B.5a. It can be seen that the constraints are satisfied for all three plant models.

B.4 Experimental Results

To validate the results, the controller was implemented in Labview and applied on the experimental setup. The step responses of the blue and red gimbal angle were measured for varying disk speeds, and the results are shown in Fig. B.5b. It can be seen that the decoupling is good, and that the multimodel uncertainty introduced by the varying disk speed is handled well. The rise time is 0.625 s for the blue and 0.486 s for the red gimbal angle, which matches well the desired bandwidth specified for L_d . Furthermore, the overshoot is limited to less than 10 %.

B.5 Conclusion

The control of a 2-DOF gyroscope shows that the method is well suited for multivariable control design of strongly coupled systems under multimodel uncertainty, which is a chal-

Appendix B. Data-driven Multivariable Control of a 2-DOF Gyroscope

lenging and relevant problem in many practical applications. The achieved performance is validated on an experimental setup and proves the viability of the approach.

Bibliography

- [1] Andreas Ulbig, Theodor S. Borsche, and Göran Andersson. Impact of low rotational inertia on power system stability and operation. *IFAC Proceedings Volumes*, 47(3): 7290–7297, 2014.
- [2] Alireza Karimi and Christoph Kammer. A data-driven approach to robust control of multivariable systems by convex optimization. *Automatica*, <http://dx.doi.org/10.1016/j.automatica.2017.07.063>, 85:227–233, 2017.
- [3] Christoph Kammer and Alireza Karimi. New distributed architecture for frequency and voltage control in islanded grids. *IEEE Transactions on Smart Grid (submitted)*, 2018.
- [4] Christoph Kammer, Salvatore D’Arco, Atsede Guali Endegnanew, and Alireza Karimi. Convex optimization-based control design for parallel grid-connected inverters. *IEEE Transactions on Power Electronics (submitted)*, 2018.
- [5] Christoph Kammer and Alireza Karimi. Decentralized and distributed transient control for microgrids. *IEEE Transactions on Control Systems Technology*, 2017. ISSN 1063-6536. doi: 10.1109/TCST.2017.2768421.
- [6] Christoph Kammer and Alireza Karimi. Advanced droop control in islanded microgrids using dynamic phasor models. *IFAC-PapersOnLine*, 50(1):6642–6647, 2017.
- [7] Christoph Kammer and Alireza Karimi. Robust distributed averaging frequency control of inverter-based microgrids. In *55th IEEE Conference on Decision and Control (CDC)*, pages 4973–4978. IEEE, 2016.
- [8] Christoph Kammer, Adrian P. Nievergelt, Georg E. Fantner, and Alireza Karimi. Data-driven controller design for atomic-force microscopy. *IFAC-PapersOnLine*, 50(1):10437–10442, 2017.
- [9] Christoph Kammer and Alireza Karimi. A data-driven fixed-structure control design method with application to a 2-DOF gyroscope. *IEEE Conference on Control Technology and Applications*, 2018 (accepted).

Bibliography

- [10] George Zames. Feedback and optimal sensitivity: Model reference transformations, multiplicative seminorms, and approximate inverses. *IEEE Transactions on Automatic Control*, 26(2):301–320, 1981.
- [11] J. W. Helton. Orbit structure of the mobius transformation semigroup acting on H_∞ broadband matching. *Topics in Functional Analysis: Advances in Mathematics Supplementary Studies*, 3:129–157, 1978.
- [12] Allen Tannenbaum. Feedback stabilization of linear dynamical plants with uncertainty in the gain factor. *International Journal of Control*, 32(1):1–16, 1980.
- [13] Carsten W. Scherer. Multiobjective H_2/H_∞ control. *IEEE Transactions on Automatic Control*, 40(6):1054–1062, 1995.
- [14] Kemin Zhou, John Comstock Doyle, Keith Glover, et al. *Robust and optimal control*, volume 40. Prentice hall New Jersey, 1996.
- [15] Zhong-Sheng Hou and Zhuo Wang. From model-based control to data-driven control: Survey, classification and perspective. *Information Sciences*, 235:3–35, 2013.
- [16] Mahdiah S. Sadabadi and Dimitri Peaucelle. From static output feedback to structured robust static output feedback: A survey. *Annual Reviews in Control*, 42:11–26, 2016.
- [17] Tetsuya Iwasaki. The dual iteration for fixed-order control. *IEEE Transactions on Automatic Control*, 44(4):783–788, 1999.
- [18] Pierre Apkarian, Dominikus Noll, Jean-Baptiste Thevenet, and Hoang Duong Tuan. A spectral quadratic-SDP method with applications to fixed-order H_2 and H_∞ synthesis. *European Journal of Control*, 10(6):527–538, 2004.
- [19] Pierre Apkarian and Dominikus Noll. Nonsmooth H_∞ synthesis. *IEEE Trans. on Automatic Control*, 51(1):71–86, 2006.
- [20] Pascal Gahinet and Pierre Apkarian. Decentralized and fixed-structure H_∞ control in matlab. In *Decision and Control and European Control Conference (CDC-ECC), 2011 50th IEEE Conference on*, pages 8205–8210. IEEE, 2011.
- [21] Pascal Gahinet and Pierre Apkarian. Structured H_∞ synthesis in matlab. *IFAC Proceedings Volumes*, 44(1):1435–1440, 2011.
- [22] James V. Burke, Didier Henrion, Adrian S. Lewis, and Michael L. Overton. HIFOO : A MATLAB package for fixed-order controller design and H_∞ optimization. In *Fifth IFAC Symposium on Robust Control Design, Toulouse*, 2006.

-
- [23] Cesar A.R. Crusius and Alexandre Trofino. Sufficient LMI conditions for output feedback control problems. *IEEE Transactions on Automatic Control*, 44(5):1053–1057, 1999.
- [24] Pierre Apkarian, Hoang Duong Tuan, and Jacques Bernussou. Continuous-time analysis, eigenstructure assignment, and H_2 synthesis with enhanced linear matrix inequalities (LMI) characterizations. *IEEE Transactions on Automatic Control*, 46(12):1941–1946, 2001.
- [25] Didier Henrion, Michael Sebek, and Vladimir Kucera. Positive polynomials and robust stabilization with fixed-order controllers. *IEEE Transactions on Automatic Control*, 48(7):1178–1186, 2003.
- [26] Kwan Ho Lee, Joon Hwa Lee, and Wook Hyun Kwon. Sufficient LMI conditions for H_∞ output feedback stabilization of linear discrete-time systems. *IEEE Transactions on Automatic Control*, 51(4):675–680, 2006.
- [27] Alireza Karimi, Hamid Khatibi, and Roland Longchamp. Robust control of polytopic systems by convex optimization. *Automatica*, 43(8):1395–1402, 2007.
- [28] Cristiano M. Agulhari, Ricardo Oliveira, and Pedro L. D. Peres. LMI relaxations for reduced-order robust H_∞ control of continuous-time uncertain linear systems. *IEEE Transactions on Automatic Control*, 57(6):1532–1537, 2012.
- [29] Mahdieh S. Sadabadi. *Fixed-structure Control of LTI Systems with Polytopic-type Uncertainty: Application to Inverter-interfaced Microgrids*. PhD thesis, Ecole Polytechnique Fédérale de Lausanne, 2016.
- [30] A. J. Den Hamer, Siep Weiland, and Maarten Steinbuch. Model-free norm-based fixed structure controller synthesis. In *Decision and Control, 2009 held jointly with the 2009 28th Chinese Control Conference. CDC/CCC 2009. Proceedings of the 48th IEEE Conference on*, pages 4030–4035. IEEE, 2009.
- [31] A. J. Den Hamer. Data-driven optimal controller synthesis: a frequency domain approach. *Eindhoven University of Technology, Eindhoven, the Netherlands*, 2010.
- [32] Masami Saeki. Data-driven loop-shaping design of PID controllers for stable plants. *International Journal of Adaptive Control and Signal Processing*, 28(12):1325–1340, 2014.
- [33] Alireza Karimi, Marc Kunze, and Roland Longchamp. Robust controller design by linear programming with application to a double-axis positioning system. *Control Engineering Practice*, 15(2):197–208, 2007.
- [34] Alireza Karimi and Gorka Galdos. Fixed-order H_∞ controller design for nonparametric models by convex optimization. *Automatica*, 46(8):1388–1394, 2010.

- [35] Alireza Karimi, Achille Nicoletti, and Yuanming Zhu. Robust H_∞ controller design using frequency-domain data via convex optimization. *International Journal of Robust and Nonlinear Control*, 2016.
- [36] Etienne Thalmann, Yves-Julien Regamey, and Alireza Karimi. High performance control of a corner cube reflector by a frequency-domain data-driven robust control method. In *American Control Conference*, pages 455–460, Boston, MA USA, 2016.
- [37] Gorka Galdos, Alireza Karimi, and Roland Longchamp. H_∞ controller design for spectral MIMO models by convex optimization. *Journal of Process Control*, 20(10): 1175–1182, 2010.
- [38] Alireza Karimi and Zlatko Emedi. H_∞ gain-scheduled controller design for rejection of time-varying narrow-band disturbances applied to a benchmark problem. *European Journal of Control*, 19(4):279–288, 2013. ISSN 0947-3580. doi: 10.1016/j.ejcon.2013.05.010.
- [39] Behrooz Bahrani, Alireza Karimi, Benoit Rey, and Alfred Rufer. Decoupled dq-current control of grid-tied voltage source converters using nonparametric models. *IEEE Trans. on Industrial Electronics*, 60(4):1356 – 1366, 2013. ISSN 0278-0046. doi: 10.1109/TIE.2012.2185017.
- [40] J. D. Dasika, B. Bahrani, M. Saeedifard, A. Karimi, and A. Rufer. Multivariable control of single-inductor dual-output buck converters. *IEEE Trans. on Power Electronics*, 29(4):2061–2070, 2014.
- [41] Alireza Karimi. Frequency-domain robust control toolbox. In *52nd IEEE Conference in Decision and Control*, pages 3744 – 3749, 2013.
- [42] E. Solingen, J. W. Wingerden, and T. Oomen. Frequency-domain optimization of fixed-structure controllers. *International Journal of Robust and Nonlinear Control*, 2016.
- [43] Masami Saeki, Masashi Ogawa, and Nobutaka Wada. Low-order H_∞ controller design on the frequency domain by partial optimization. *International Journal of Robust and Nonlinear Control*, 20(3):323–333, 2010.
- [44] Martin Hast, Karl J. Åström, Bo Bernhardsson, and Stephen Boyd. PID design by convex-concave optimization. In *Control Conference (ECC), 2013 European*, pages 4460–4465. IEEE, 2013.
- [45] Stephen Boyd, Martin Hast, and Karl Johan Åström. MIMO PID tuning via iterated LMI restriction. *International Journal of Robust and Nonlinear Control*, 26(8):1718–1731, 2016.
- [46] Pedro Mercader, Karl Johan Åström, Alfonso Banos, and Tore Hägglund. Robust PID design based on QFT and convex-concave optimization. *IEEE Transactions on Control Systems Technology*, 25(2):441–452, 2017.

-
- [47] Shogo Shinoda, Kazuhiro Yubai, Daisuke Yashiro, and Junji Hirai. Multivariable controller design evaluating closed-loop interaction by iterative LMI optimization using frequency response data. In *Advanced Mechatronic Systems (ICAMechS), 2015 International Conference on*, pages 429–434. IEEE, 2015.
- [48] Pierre Apkarian and Dominikus Noll. Structured H_∞ -control of infinite dimensional systems. *arXiv:1707.02052 [math.OC]*, 2017.
- [49] R. Pintelon and J. Schoukens. *System Identification: A Frequency Domain Approach*. IEEE Press, New York, USA, 2001.
- [50] Quoc Tran Dinh, Suat Gumussoy, Wim Michiels, and Moritz Diehl. Combining convex–concave decompositions and linearization approaches for solving BMIs, with application to static output feedback. *IEEE Transactions on Automatic Control*, 57(6):1377–1390, 2012.
- [51] Alistair G. J. MacFarlane and Ian Postlethwaite. The generalized nyquist stability criterion and multivariable root loci. *International Journal of Control*, 25(1):81–127, 1977.
- [52] C. Y. Zhang, S. Luo, A. Huang, and J. Lu. The eigenvalue distribution of block diagonally dominant matrices and block H-matrices. *Electronic Journal of Linear Algebra*, 20(1):621–639, 2010.
- [53] Haitham Hindi, Chang-Yun Seong, and Stephen Boyd. Computing optimal uncertainty models from frequency domain data. In *41st IEEE Conference on Decision and Control*, volume 3, pages 2898–2905, Las Vegas, Nevada USA, 2002.
- [54] Kemin Zhou. *Essentials of Robust Control*. Prentice Hall, New Jersey, 1998.
- [55] T. Alamo, R. Tempo, and A. Luque. On the sample complexity of probabilistic analysis and design methods. In *Perspectives in Mathematical System Theory, Control, and Signal Processing*, pages 39–55. Springer, 2010.
- [56] Alan L. Yuille and Anand Rangarajan. The concave-convex procedure. *Neural Computation*, 15(4):915–936, 2003.
- [57] F. Leibfritz. COMPluib: constrained matrix optimization problem library, 2006.
- [58] Johan Löfberg. YALMIP: A toolbox for modeling and optimization in MATLAB. In *CACSD Conference*, <http://control.ee.ethz.ch/joloef/yalmip.php>, 2004.
- [59] MOSEK ApS. *The MOSEK optimization toolbox for MATLAB manual. Version 7.1*, 2015. URL <http://docs.mosek.com/7.1/toolbox/index.html>.
- [60] Prabha Kundur, Neal J. Balu, and Mark G. Lauby. *Power system stability and control*, volume 7. McGraw-hill New York, 1994.

- [61] F. Katiraei, M. R. Iravani, and P. W. Lehn. Small-signal dynamic model of a micro-grid including conventional and electronically interfaced distributed resources. *IET generation, transmission & distribution*, 1(3):369–378, 2007.
- [62] Nagaraju Pogaku, Milan Prodanovic, and Timothy C. Green. Modeling, analysis and testing of autonomous operation of an inverter-based microgrid. *IEEE Transactions on Power Electronics*, 22(2):613–625, 2007.
- [63] Masoud Honarvar Nazari, Marija Ilic, and João PeCcas Lopes. Small-signal stability and decentralized control design for electric energy systems with a large penetration of distributed generators. *Control Engineering Practice*, 20(9):823–831, 2012.
- [64] Kai Yu, Qian Ai, Shiyi Wang, Jianmo Ni, and Tianguang Lv. Analysis and optimization of droop controller for microgrid system based on small-signal dynamic model. *IEEE Transactions on Smart Grid*, 7(2):695–705, 2016.
- [65] Shivkumar V. Iyer, Madhu N. Belur, and Mukul C. Chandorkar. A generalized computational method to determine stability of a multi-inverter microgrid. *IEEE Transactions on Power Electronics*, 25(9):2420–2432, 2010.
- [66] M. Rasheduzzaman, Jacob A. Mueller, and Jonathan W. Kimball. Reduced-order small-signal model of microgrid systems. *IEEE Transactions on Sustainable Energy*, 6(4):1292–1305, 2015.
- [67] Valerio Mariani, Francesco Vasca, Juan C. Vásquez, and Josep M. Guerrero. Model order reductions for stability analysis of islanded microgrids with droop control. *IEEE Transactions on Industrial Electronics*, 62(7):4344–4354, 2015.
- [68] Xiaotian Zhang, Joseph W. Spencer, and Josep M. Guerrero. Small-signal modeling of digitally controlled grid-connected inverters with LCL filters. *IEEE Transactions on Industrial Electronics*, 60(9):3752–3765, 2013.
- [69] Jinwei He, Yun Wei Li, Dubravko Bosnjak, and Brent Harris. Investigation and active damping of multiple resonances in a parallel-inverter-based microgrid. *IEEE Transactions on Power Electronics*, 28(1):234–246, 2013.
- [70] Xiongfei Wang, Frede Blaabjerg, Marco Liserre, Zhe Chen, Jinwei He, and Yunwei Li. An active damper for stabilizing power-electronics-based ac systems. *IEEE Transactions on Power Electronics*, 29(7):3318–3329, 2014.
- [71] Vaithianathan Venkatasubramanian, Heinz Schattler, and John Zaborszky. Fast time-varying phasor analysis in the balanced three-phase large electric power system. *IEEE Transactions on Automatic Control*, 40(11):1975–1982, 1995.
- [72] Eric H. Allen and Marija D. Ilic. Interaction of transmission network and load phasor dynamics in electric power systems. *IEEE Transactions on Circuits and Systems I: Fundamental Theory and Applications*, 47(11):1613–1620, 2000.

-
- [73] M. H. Nazari and M. Ilic. Dynamic modelling and control of distribution energy systems: comparison with transmission power systems. *IET Generation, Transmission & Distribution*, 8(1):26–34, 2014.
- [74] X. Guo, Z. Lu, B. Wang, X. Sun, L. Wang, and J. M. Guerrero. Dynamic phasors-based modeling and stability analysis of droop-controlled inverters for microgrid applications. *IEEE Transactions on Smart Grid*, 5(6):2980–2987, 2014.
- [75] Clayton R. Paul. *Analysis of multiconductor transmission lines*. John Wiley & Sons, 2008.
- [76] Andreas M. Kettner and Mario Paolone. On the properties of the power systems nodal admittance matrix. *IEEE Transactions on Power Systems*, 33(1):1130–1131, 2018.
- [77] Joan Rocabert, Alvaro Luna, Frede Blaabjerg, and Pedro Rodriguez. Control of power converters in ac microgrids. *IEEE Transactions on Power Electronics*, 27(11):4734–4749, 2012.
- [78] Dominik Amrein. Dynamisches Verhalten von Verteilnetzen mit dezentralen Kraftwerken. Master’s thesis, University of Applied Sciences Bern, 2016.
- [79] Łukasz H. Kocewiak, Jesper Hjerrild, and Claus Leth Bak. Wind turbine converter control interaction with complex wind farm systems. *IET Renewable Power Generation*, 7(4):380–389, 2013.
- [80] Xiongfei Wang, Frede Blaabjerg, Zhe Chen, and Weimin Wu. Resonance analysis in parallel voltage-controlled distributed generation inverters. In *Applied Power Electronics Conference and Exposition (APEC), 2013 Twenty-Eighth Annual IEEE*, pages 2977–2983. IEEE, 2013.
- [81] Fei Wang, Jorge L. Duarte, Marcel A. M. Hendrix, and Paulo F. Ribeiro. Modeling and analysis of grid harmonic distortion impact of aggregated DG inverters. *IEEE Transactions on Power Electronics*, 26(3):786–797, 2011.
- [82] Robert Turner, Simon Walton, and Richard Duke. Stability and bandwidth implications of digitally controlled grid-connected parallel inverters. *IEEE Transactions on Industrial Electronics*, 57(11):3685–3694, 2010.
- [83] Camilo C. Gomes, Allan F. Cupertino, and Heverton A. Pereira. Damping techniques for grid-connected voltage source converters based on LCL filter: An overview. *Renewable and Sustainable Energy Reviews*, 81:116–135, 2018.
- [84] Salvatore D’Arco, Jon Are Suul, and Olav B. Fosso. Control system tuning and stability analysis of virtual synchronous machines. In *Energy Conversion Congress and Exposition (ECCE), 2013 IEEE*, pages 2664–2671. IEEE, 2013.

Bibliography

- [85] Nathaniel Bottrell, Milan Prodanovic, and Timothy C. Green. Dynamic stability of a microgrid with an active load. *IEEE Transactions on Power Electronics*, 28(11):5107–5119, 2013.
- [86] Bo Wen, Dong Dong, Dushan Boroyevich, Rolando Burgos, Paolo Mattavelli, and Zhiyu Shen. Impedance-based analysis of grid-synchronization stability for three-phase paralleled converters. *IEEE Transactions on Power Electronics*, 31(1):26–38, 2016.
- [87] Rafael Peña-Alzola, Marco Liserre, Frede Blaabjerg, Martin Ordonez, and Yongheng Yang. LCL-filter design for robust active damping in grid-connected converters. *IEEE Transactions on Industrial Informatics*, 10(4):2192–2203, 2014.
- [88] Juan Luis Agorreta, Mikel Borrega, Jesús López, and Luis Marroyo. Modeling and control of N -paralleled grid-connected inverters with LCL filter coupled due to grid impedance in PV plants. *IEEE Transactions on Power Electronics*, 26(3):770–785, 2011.
- [89] Mikel Borrega, Luis Marroyo, Roberto Gonzalez, Julián Balda, and Juan Luis Agorreta. Modeling and control of a master–slave PV inverter with N -paralleled inverters and three-phase three-limb inductors. *IEEE Transactions on Power Electronics*, 28(6):2842–2855, 2013.
- [90] Xiongfei Wang, Frede Blaabjerg, and Weimin Wu. Modeling and analysis of harmonic stability in an AC power-electronics-based power system. *IEEE Transactions on Power Electronics*, 29(12):6421–6432, 2014.
- [91] Minghui Lu, Xiongfei Wang, Frede Blaabjerg, and Poh Chiang Loh. An analysis method for harmonic resonance and stability of multi-paralleled LCL-filtered inverters. In *Power Electronics for Distributed Generation Systems (PEDG), 2015 IEEE 6th International Symposium on*, pages 1–6. IEEE, 2015.
- [92] Minghui Lu, Xiongfei Wang, Poh Chiang Loh, and Frede Blaabjerg. Resonance interaction of multiparallel grid-connected inverters with LCL filter. *IEEE Transactions on Power Electronics*, 32(2):894–899, 2017.
- [93] Luiz Antonio Maccari, Jorge Rodrigo Massing, Luciano Schuch, Cassiano Rech, Humberto Pinheiro, Ricardo Oliveira, and Vinicius Foletto Montagner. LMI-based control for grid-connected converters with LCL filters under uncertain parameters. *IEEE Transactions on Power Electronics*, 29(7):3776–3785, 2014.
- [94] L. A. Maccari, J. R. Massing, L. Schuch, C. Rech, H. Pinheiro, V. F. Montagner, and R. Oliveira. Robust \mathcal{H}_∞ control for grid connected PWM inverters with LCL filters. In *Industry Applications (INDUSCON), 2012 10th IEEE/IAS International Conference on*, pages 1–6. IEEE, 2012.

-
- [95] J. R. Massing, G. G. Koch, A. T. Pereira, H. Pinheiro, V. F. Montagner, and R. Oliveira. Modeling and stability analysis of current controllers for multi-paralleled grid-connected converters with LCL-filter. In *Control and Modeling for Power Electronics (COMPEL), 2017 IEEE 18th Workshop on*, pages 1–7. IEEE, 2017.
- [96] Mahdiah S. Sadabadi, Aboutaleb Haddadi, Houshang Karimi, and Alireza Karimi. A robust active damping control strategy for an LCL-based grid-connected DG unit. *IEEE Transactions on Industrial Electronics*, 2017.
- [97] Mahdiah S. Sadabadi, Qobad Shafiee, and Alireza Karimi. Plug-and-play voltage stabilization in inverter-interfaced microgrids via a robust control strategy. *IEEE Transactions on Control Systems Technology*, 25(3):781–791, 2017.
- [98] Behrooz Bahrani and Alfred Rufer. Optimization-based voltage support in traction networks using active line-side converters. *IEEE Transactions on Power Electronics*, 28(2):673–685, 2013.
- [99] Behrooz Bahrani, Michail Vasiladiotis, and Alfred Rufer. High-order vector control of grid-connected voltage-source converters with LCL-filters. *IEEE Transactions on Industrial Electronics*, 61(6):2767–2775, 2014.
- [100] Chi Zhang, Josep M. Guerrero, Juan C. Vasquez, and Carsten Michaelson Seniger. Modular Plug-n-Play control architectures for three-phase inverters in UPS applications. *IEEE Transactions on Industry Applications*, 52(3):2405–2414, 2016.
- [101] Souvik Dasgupta, Shankar Narayan Mohan, Sanjib K. Sahoo, and Sanjib Kumar Panda. A plug and play operational approach for implementation of an autonomous-micro-grid system. *IEEE Transactions on Industrial Informatics*, 8(3):615–629, 2012.
- [102] Vahidreza Nasirian, Qobad Shafiee, Josep M. Guerrero, Frank L. Lewis, and Ali Davoudi. Droop-free distributed control for AC microgrids. *IEEE Transactions on Power Electronics*, 31(2):1600–1617, 2016.
- [103] Stefano Riverso, Fabio Sarzo, and Giancarlo Ferrari-Trecate. Plug-and-play voltage and frequency control of islanded microgrids with meshed topology. *IEEE Transactions on Smart Grid*, 6(3):1176–1184, 2015.
- [104] Sigurd Skogestad and Ian Postlethwaite. *Multivariable feedback control: analysis and design*, volume 2. Wiley New York, 2007.
- [105] Paolo Mattavelli. A closed-loop selective harmonic compensation for active filters. *IEEE Transactions on Industry Applications*, 37(1):81–89, 2001.
- [106] Daniel E. Olivares, Ali Mehrizi-Sani, Amir H. Etemadi, Claudio A. Cañizares, Reza Iravani, Mehrdad Kazerani, Amir H. Hajimiragha, Oriol Gomis-Bellmunt, Maryam Saeedifard, Rodrigo Palma-Behnke, et al. Trends in microgrid control. *IEEE Transactions on Smart Grid*, 5(4):1905–1919, 2014.

Bibliography

- [107] Qing-Chang Zhong and George Weiss. Synchronverters: Inverters that mimic synchronous generators. *IEEE Transactions on Industrial Electronics*, 58(4):1259–1267, 2011.
- [108] Yan Du, Josep M. Guerrero, Liuchen Chang, Jianhui Su, and Meiqin Mao. Modeling, analysis, and design of a frequency-droop-based virtual synchronous generator for microgrid applications. In *ECCE Asia Downunder (ECCE Asia), 2013 IEEE*, pages 643–649. IEEE, 2013.
- [109] Hassan Bevrani, Toshifumi Ise, and Yushi Miura. Virtual synchronous generators: A survey and new perspectives. *International Journal of Electrical Power & Energy Systems*, 54:244–254, 2014.
- [110] Nimish Soni, Suryanarayana Doolla, and Mukul C. Chandorkar. Improvement of transient response in microgrids using virtual inertia. *IEEE Transactions on Power Delivery*, 28(3):1830–1838, 2013.
- [111] Enrique Mallada. idroop: A dynamic droop controller to decouple power grid’s steady-state and dynamic performance. In *Decision and Control (CDC), 2016 IEEE 55th Conference on*, pages 4957–4964. IEEE, 2016.
- [112] Richard Pates and Enrique Mallada. Decentralised robust inverter-based control in power systems. *IFAC-PapersOnLine*, 50(1):5548–5553, 2017.
- [113] J. W. Simpson-Porco, F. Dörfler, and F. Bullo. Synchronization and power sharing for droop-controlled inverters in islanded microgrids. *Automatica*, 49(9):2603–2611, 2013.
- [114] Johannes Schiffer, Romeo Ortega, Alessandro Astolfi, Jörg Raisch, and Tevfik Sezi. Conditions for stability of droop-controlled inverter-based microgrids. *Automatica*, 50(10):2457–2469, 2014.
- [115] Karel De Brabandere, Bruno Bolsens, Jeroen Van den Keybus, Achim Woyte, Johan Driesen, and Ronnie Belmans. A voltage and frequency droop control method for parallel inverters. *IEEE Transactions on Power Electronics*, 22(4):1107–1115, 2007.
- [116] Jinwei He, Yun Wei Li, Josep M. Guerrero, Frede Blaabjerg, and Juan C. Vasquez. An islanding microgrid power sharing approach using enhanced virtual impedance control scheme. *IEEE Transactions on Power Electronics*, 28(11):5272–5282, 2013.
- [117] Josep M. Guerrero, Juan C. Vasquez, José Matas, Luis García De Vicuña, and Miguel Castilla. Hierarchical control of droop-controlled AC and DC microgrids - a general approach toward standardization. *IEEE Transactions on Industrial Electronics*, 58(1):158–172, 2011.
- [118] José Matas, Miguel Castilla, Luis Garcia de Vicuna, Jaume Miret, and Juan Carlos Vasquez. Virtual impedance loop for droop-controlled single-phase parallel inverters

- using a second-order general-integrator scheme. *IEEE Transactions on Power Electronics*, 25(12):2993–3002, 2010.
- [119] Ali Bidram, Ali Davoudi, Frank L. Lewis, and Josep M. Guerrero. Distributed cooperative secondary control of microgrids using feedback linearization. *IEEE Transactions on Power Systems*, 28(3):3462–3470, 2013.
- [120] Ali Bidram, Ali Davoudi, Frank L. Lewis, and Zhihua Qu. Secondary control of microgrids based on distributed cooperative control of multi-agent systems. *IET Generation, Transmission & Distribution*, 7(8):822–831, 2013.
- [121] Fanghong Guo, Changyun Wen, Jianfeng Mao, and Yong-Duan Song. Distributed secondary voltage and frequency restoration control of droop-controlled inverter-based microgrids. *IEEE Transactions on Industrial Electronics*, 62(7):4355–4364, 2015.
- [122] Florian Dörfler, John W Simpson-Porco, and Francesco Bullo. Breaking the hierarchy: Distributed control and economic optimality in microgrids. *IEEE Transactions on Control of Network Systems*, 3(3):241–253, 2016.
- [123] Daniel K. Molzahn, Florian Dörfler, Henrik Sandberg, Steven H. Low, Sambuddha Chakrabarti, Ross Baldick, and Javad Lavaei. A survey of distributed optimization and control algorithms for electric power systems. *IEEE Transactions on Smart Grid*, 8(6):2941–2962, 2017.
- [124] Qobad Shafiee, Čedomir Stefanović, Tomislav Dragičević, Petar Popovski, Juan C. Vasquez, and Josep M. Guerrero. Robust networked control scheme for distributed secondary control of islanded microgrids. *IEEE Transactions on Industrial Electronics*, 61(10):5363–5374, 2014.
- [125] Stefano Rivero, Michele Tucci, Juan C. Vasquez, Josep M. Guerrero, and Giancarlo Ferrari-Trecate. Stabilizing plug-and-play regulators and secondary coordinated control for ac islanded microgrids with bus-connected topology. *Applied Energy*, 210:914–924, 2018.
- [126] Amir H Etemadi, Edward J. Davison, and Reza Iravani. A decentralized robust control strategy for multi-DER microgrids - part I: Fundamental concepts. *IEEE Transactions on Power Delivery*, 27(4):1843–1853, 2012.
- [127] Amir H. Etemadi, Edward J. Davison, and Reza Iravani. A decentralized robust control strategy for multi-DER microgrids - part II: Performance evaluation. *IEEE Transactions on Power Delivery*, 27(4):1854–1861, 2012.
- [128] Jahangir Hossain, Apel Mahmud, Federico Milano, Seddik Bacha, and Ahmad Hably. Design of robust distributed control for interconnected microgrids. *IEEE Transactions on Smart Grid*, 7(6):2724–2735, 2016.

- [129] Alfredo Vaccaro, Giovanni Velotto, and Ahmed F. Zobaa. A decentralized and cooperative architecture for optimal voltage regulation in smart grids. *IEEE Transactions on Industrial Electronics*, 58(10):4593–4602, 2011.
- [130] M. J. Hossain, Hemanshu Roy Pota, M. Apel Mahmud, and Mohammad Aldeen. Robust control for power sharing in microgrids with low-inertia wind and PV generators. *IEEE Transactions on Sustainable Energy*, 6(3):1067–1077, 2015.
- [131] Quang L. Lam, Antoneta I. Bratcu, Delphine Riu, and Jiravan Mongkoltanatas. Multi-variable H-infinity robust control applied to primary frequency regulation in microgrids with large integration of photovoltaic energy source. In *Industrial Technology (ICIT), 2015 IEEE International Conference on*, pages 2921–2928. IEEE, 2015.
- [132] Hassan Bevrani, Mohammad Ramin Feizi, and Sirwan Ataei. Robust frequency control in an islanded microgrid: H_∞ and μ -synthesis approaches. *IEEE Transactions on Smart Grid*, 7(2):706–717, 2016.
- [133] Mahdiah S. Sadabadi, Alireza Karimi, and Houshang Karimi. Fixed-order decentralized/distributed control of islanded inverter-interfaced microgrids. *Control Engineering Practice*, 45:174–193, 2015.
- [134] Michele Tucci and Giancarlo Ferrari-Trecate. Voltage and frequency control in AC islanded microgrids: a scalable, line-independent design algorithm. *IFAC-PapersOnLine*, 50(1):13922–13927, 2017.
- [135] Karel De Brabandere, Bruno Bolsens, Jeroen Van Den Keybus, Johan Driesen, Milan Prodanovic, and Ronnie Belmans. Small-signal stability of grids with distributed low-inertia generators taking into account line phasor dynamics. In *Electricity Distribution, 2005. CIRED 2005. 18th International Conference and Exhibition on*, pages 1–5. IET, 2005.
- [136] Karel De Brabandere. *Voltage and Frequency Droop Control in Low Voltage Grids By Distributed Generators with Inverter Front-End*. PhD thesis, Katholieke Universiteit Leuven, FACULTEIT INGENIEURSWETENSCHAPPEN, 3001 Leuven, Belgium, 2006.
- [137] K. Rudion, A. Orths, Z.A. Styczynski, and K. Strunz. Design of benchmark of medium voltage distribution network for investigation of DG integration. *2006 IEEE Power Engineering Society General Meeting*, page 6, 2006. doi: 10.1109/PES.2006.1709447.
- [138] Sergei N. Magonov and Darrell H. Reneker. Characterization of polymer surfaces with atomic force microscopy. *Annual Review of Materials Science*, 27(1):175–222, 1997.

-
- [139] Rachel A. Oliver. Advances in AFM for the electrical characterization of semiconductors. *Reports on Progress in Physics*, 71(7):076501, 2008.
- [140] Adrian P. Nievergelt, Niccolò Banterle, Santiago H. Andany, Pierre Gönczy, and Georg E. Fantner. High-speed photothermal off-resonance atomic force microscopy reveals assembly routes of centriolar scaffold protein SAS-6. *Nature Nanotechnology*, 2018.
- [141] Leo Gross, Fabian Mohn, Nikolaj Moll, Peter Liljeroth, and Gerhard Meyer. The chemical structure of a molecule resolved by atomic force microscopy. *Science*, 325(5944):1110–1114, 2009.
- [142] Pierre Parot, Yves F. Dufrêne, Peter Hinterdorfer, Christian Le Grimmelc, Daniel Navajas, Jean-Luc Pellequer, and Simon Scheuring. Past, present and future of atomic force microscopy in life sciences and medicine. *Journal of Molecular Recognition*, 20(6):418–431, 2007.
- [143] Yves F. Dufrêne, Toshio Ando, Ricardo Garcia, David Alsteens, David Martinez-Martin, Andreas Engel, Christoph Gerber, and Daniel J. Müller. Imaging modes of atomic force microscopy for application in molecular and cell biology. *Nature nanotechnology*, 12(4):295, 2017.
- [144] Hermann Schillers, Izhar Medalsy, Shuiqing Hu, Andrea L. Slade, and James E. Shaw. Peakforce tapping resolves individual microvilli on living cells. *Journal of Molecular Recognition*, 29(2):95–101, 2016.
- [145] Daniel Y. Abramovitch, Sean B. Andersson, Lucy Y. Pao, and Georg Schitter. A tutorial on the mechanisms, dynamics, and control of atomic force microscopes. In *American Control Conference, 2007. ACC'07*, pages 3488–3502. IEEE, 2007.
- [146] G. Schitter, F. Allgöwer, and A. Stemmer. A new control strategy for high-speed atomic force microscopy. *Nanotechnology*, 15(1):108, 2003.
- [147] Noriyuki Kodera, Hayato Yamashita, and Toshio Ando. Active damping of the scanner for high-speed atomic force microscopy. *Review of Scientific Instruments*, 76(5):053708, 2005.
- [148] Daniel J. Burns, Kamal Youcef-Toumi, and Georg E. Fantner. Indirect identification and compensation of lateral scanner resonances in atomic force microscopes. *Nanotechnology*, 22(31):315701, 2011.
- [149] Yuen Kuan Yong, Bharath Bhikkaji, and Reza S. O. Moheimani. Design, modeling, and FPAA-based control of a high-speed atomic force microscope nanopositioner. *IEEE/ASME Transactions on Mechatronics*, 18(3):1060–1071, 2013.
- [150] Adrian P. Nievergelt, Blake W. Erickson, Nahid Hosseini, Jonathan D. Adams, and Georg E. Fantner. Studying biological membranes with extended range high-speed atomic force microscopy. *Scientific reports*, 5:11987, 2015.

Bibliography

- [151] Shingo Ito, Daniel Neyer, Juergen Steininger, and Georg Schitter. Dual actuation of fast scanning axis for high-speed atomic force microscopy. *IFAC-PapersOnLine*, 50(1):7633–7638, 2017.
- [152] T. D. Gupta, H. Habibullah, H. R. Pota, and I. R. Petersen. Data driven controller design for positioning control of an AFM scanner. *IFAC-PapersOnLine*, 50(1):10889–10894, 2017.
- [153] Stefan Kuiper, Paul M. J. Van den Hof, and Georg Schitter. Towards integrated design of a robust feedback controller and topography estimator for atomic force microscopy. *IFAC Proceedings Volumes*, 44(1):12709–12714, 2011.
- [154] Ning Chuang, Ian R. Petersen, and Hemanshu R. Pota. Robust H_∞ control in fast atomic force microscopy. *Asian Journal of Control*, 15(3):872–887, 2013.

Christoph Kammer

Liebeggweg 8

3006 Bern

Switzerland

+41 76 358 16 00

ckammer87@gmail.com

Date of Birth: 31.10.1987

Nationality: Swiss



Highlights

Competences	Strong background in optimization and control, power electronics and power systems dynamics. Experience in designing and implementing advanced control techniques for a broad range of architectures and applications. Extensive knowledge of power system modeling and simulation.
Soft Skills	Independent and diligent worker, very quick grasp of new matters, ability to enable communication between different fields, good collaborator, adaptable

Professional Experience

05/2014 – 06/2018	Doctoral Assistant , <i>École Polytechnique Fédérale de Lausanne (EPFL)</i> , Switzerland <ul style="list-style-type: none">• Development of a data-driven, robust control design method based on convex optimization. Standard performance specifications are formulated straightforwardly as frequency-domain constraints. The method is used to design multivariable fixed-structure controllers that are very common in industry (e.g. PID)• Development of a novel frequency-domain dynamic phasor model for electromagnetic and electromechanic transient analysis of power grids and generation units. The model allows the combination of white-, grey- and black-box models, and exhibits desirable properties for control design• Application of the method and dynamic phasor model to design distributed controllers for primary and secondary control design in islanded grids• Development of a current control design method for multiple inverters in weak distribution grids. A non-iterative approach is developed that guarantees stability and optimal performance• Extensive modeling and simulation of low- and medium-voltage grids, inverters and synchronous generators in Simulink using the Simpower toolbox• Experimental validation of simulation results on a power-hardware-in-the-loop setup in collaboration with SINTEF SA at NTNU Trondheim• Teaching assistant for engineering courses in system identification and advanced control systems• Supervisor of 11 student projects in control systems on the masters level• Electrical design and programming of electromechanical laboratory setups
01/2015 – 05/2016	Research Scientist , <i>Richemont Research and Development</i> , Buttes, Switzerland <ul style="list-style-type: none">• Mechanical and electronic design and development of a test bench• Implementation of advanced control methods on embedded systems (DSP, FPGA), selection of electrical hardware and motor setup• Embedded software and data storage design to guarantee continuous, fault-free operation over several months

- Development of robust communication protocol between embedded system and host computer, design of graphical user interface
- Project planning, reporting and documentation

11/2011 – 06/2012 **Research Assistant**, *Institute for Chemical and Bioengineering, ETHZ, Switzerland*

- Electrical and embedded software design for an autonomous pipetting robot

08/2010 – 01/2011 **Industry Internship**, *Supercomputing Systems, Zürich, Switzerland*

- Development and implementation of estimation algorithms and optimal control design techniques for a demonstrator of a Maglev train
- Embedded programming on fixed-point DSP in C
- Mechanical design

Education

05/2014 – 04/2018 (expected) **PhD in Control and Electrical Engineering**
École Polytechnique Fédérale de Lausanne (EPFL), Switzerland
 Title: Transient Control in Power Systems with Inverter-Interfaced Generation
 Supervisor: Dr. Alireza Karimi

02/2011 – 07/2013 **MSc in Mechanical Engineering**
Eidgenössische Technische Hochschule Zürich (ETH), Switzerland

- Emphasis on control, optimization and estimation. Additional intensive courses in power electronics, mechanics and computer vision
- Teaching assistant for courses in mechanics
- Master's Thesis written in exchange at KTH Stockholm

Final Grade: 5.7 out of 6

09/2007 – 07/2010 **BSc in Mechanical Engineering**
Eidgenössische Technische Hochschule Zürich (ETH), Switzerland

07/2006 **Eidgenössische Matura**, *Gymnasium Kirchenfeld Bern, Switzerland*

Language Skills

German	Native speaker
English	Fluent – Cambridge Certificate of Proficiency in English (CPE)
French	Intermediate

Computer Skills

Programming	Matlab/Simulink, C/C++, Python, Java, Labview/Labview FPGA
Engineering	Simulink/Simpower Systems, EMTP, Optimization (YALMIP, Mosek), Machine Learning Methods
Office Software	Microsoft Office, Microsoft Visio, Latex

References

Dr. Alireza Karimi
 Automatic Control Laboratory
 École Polytechnique Fédérale de Lausanne, 1015 Lausanne, Switzerland
 +41 21 693 59 25, alireza.karimi@epfl.ch

Peer-Reviewed Publications

- [1] Christoph Kammer, Salvatore D'Arco, Atsede Guali Endegnanew, Alireza Karimi. Convex Optimization-based Control Design for Parallel Grid-Connected Inverters. *IEEE Transactions on Power Electronics (submitted)*, 2018.
- [2] Christoph Kammer, Alireza Karimi. New Distributed Architecture for Frequency and Voltage Control in Islanded Grids. *IEEE Transactions on Smart Grid (submitted)*, 2018.
- [3] Christoph Kammer, Alireza Karimi. Data-driven Multivariable Control Design for a Gyroscope. *Conference on Control Technology and Applications (accepted)*, 2018.
- [4] Christoph Kammer, Alireza Karimi. Decentralized and Distributed Transient Control for Microgrids. *IEEE Transactions on Control Systems Technology*, 2017.
- [5] Christoph Kammer, Alireza Karimi. Advanced Droop Control in Islanded Microgrids using Dynamic Phasor Models. *20th World Congress of IFAC, France*, 2017.
- [6] Christoph Kammer, Adrian Nievergelt, Georg Fantner, Alireza Karimi. Data-driven Controller Design for Atomic Force Microscopy. *20th World Congress of IFAC, France*, 2017.
- [7] Alireza Karimi, Christoph Kammer. A data-driven Approach to Robust Control of Multivariable Systems by Convex Optimization. *Automatica*, 2017.
- [8] Christoph Kammer, Alireza Karimi. Robust Distributed Averaging Frequency Control of Inverter-based Microgrids. *IEEE 55th Conference on Decision and Control (CDC), Las Vegas, USA*, 2016.
- [9] Jeffrey Larson, Christoph Kammer, Kuo-Yun Liang, Karl Henrik Johanson. Coordinated Route Optimization for Heavy-Duty Vehicle Platoons. *16th International Conference on Intelligent Transportation Systems (ITSC)*, 2013.